ALGORITHM THEORETICAL BASIS DOCUMENT

AIRS-TEAM RETRIEVAL FOR CORE PRODUCTS AND GEOPHYSICAL PARAMETERS

Level 2

M. T. Chahine

AIRS Team Leader

H. Aumann, M. Goldberg, L. McMillin,
P. Rosenkranz, D. Staelin, L. Strow, J. Susskind

AIRS Team Member Contributors

M. Gunson
Editor, AIRS Deputy Team Leader

Version 2.1

20-Dec-1999
JPL D-17006

Relevant Documents

AIRS Science and Measurement Requirements Document, JPL D-6665 Rev 1 September 1991 AIRS Brochure

AIRS Instrument Calibration Plan, JPL D-16821, Preliminary, October 14, 1997

AIRS Team Science Data Validation Plan, Core Products, JPL D-16822, Version 1.2, August 15, 1997

AIRS Algorithm Theoretical Basis Documents, Level 1B, Part 1: Infrared Spectrometer, JPL D-17003, Version 2.0, January 4, 1999

AIRS Algorithm Theoretical Basis Document, Level 1B, Part 2: Visible/Near-Infrared Channels, JPL D-17004, Version 2, January 4, 1999

AIRS Project Algorithm Theoretical Basis Document, Level 1b, Part 2: Microwave Instruments, JPL D-17005, Version 1.2, November 15, 1996

AIRS Algorithm Theoretical Basis Document, AIRS-Team Unified Retrieval For Core Products, Level 2, JPL D-17006, Version 1.7, September 18, 1997

AIRS Algorithm Theoretical Basis Document, AIRS-Team Retrieval For Core Products and Geophysical Parameters, Level 2, JPL D-17006, Version 2.0, December 15, 1999

ALGORITHM THEORETICAL BASIS DOCUMENT

AIRS-TEAM RETRIEVAL FOR CORE PRODUCTS AND GEOPHYSICAL PARAMETERS

Level 2

M. T. Chahine

AIRS Team Leader

H. Aumann, M. Goldberg, L. McMillin,
P. Rosenkranz, D. Staelin, L. Strow, J. Susskind

AIRS Team Member Contributors

M. Gunson
Editor, AIRS Deputy Team Leader

Version 2.1

20-Dec-1999
JPL D-17006

Relevant Documents

AIRS Science and Measurement Requirements Document, JPL D-6665 Rev 1 September 1991 AIRS Brochure

AIRS Instrument Calibration Plan, JPL D-16821, Preliminary, October 14, 1997

AIRS Team Science Data Validation Plan, Core Products, JPL D-16822, Version 1.2, August 15, 1997

AIRS Algorithm Theoretical Basis Documents, Level 1B, Part 1: Infrared Spectrometer, JPL D-17003, Version 2.0, January 4, 1999

AIRS Algorithm Theoretical Basis Document, Level 1B, Part 2: Visible/Near-Infrared Channels, JPL D-17004, Version 2, January 4, 1999

AIRS Project Algorithm Theoretical Basis Document, Level 1b, Part 2: Microwave Instruments, JPL D-17005, Version 1.2, November 15, 1996

AIRS Algorithm Theoretical Basis Document, AIRS-Team Unified Retrieval For Core Products, Level 2, JPL D-17006, Version 1.7, September 18, 1997

AIRS Algorithm Theoretical Basis Document, AIRS-Team Retrieval For Core Products and Geophysical Parameters, Level 2, JPL D-17006, Version 2.0, December 15, 1999

Version History

Version 2.0 of the AIRS Level 2 Algorithm Theoretical Basis Document 'AIRS-TEAM RETRIEVAL FOR CORE PRODUCTS AND GEOPHYSICAL PARAMETERS' directly replaces and follows the Version 1.7 (11/96) document ', AIRS-TEAM UNIFIED RETRIEVAL FOR CORE PRODUCTS'. The essential algorithms at the heart of the AIRS level 2 data product generation executive have not changed.

Version 2.1 is revised with a new Section 5.4 and Chapter 6. The changes are consistent with the equations of V1.7, and provide a more detailed explanation of the Final Product algorithm.

Table Of Contents

Table of Figures

1. INTRODUCTION

The Atmospheric Infrared Sounder (AIRS) is a facility instrument selected by NASA to fly on the second Earth Observing System polar orbiting platform, EOS-Aqua. The same platform will also carry the NOAA operational Advanced Microwave Sounding Unit, AMSU, and the Microwave Humidity Sounder of Brazil (HSB). AIRS is designed to meet the requirements of the NASA Earth Science Enterprise climate research programs and the NOAA operational weather forecasting plans.

The AIRS/AMSU/HSB system will provide both new and improved measurements of clouds, atmosphere, and land and oceans, with the accuracy, resolution and coverage required by future weather and climate models. Such data will be used to validate climate models, study geophysical processes, and monitor trends. The purpose of this document is to give an overview of the important climate data sets that AIRS/AMSU/HSB will produce:

- atmospheric temperature profiles with an average layer accuracy of 1K in 1 km thick layers in the troposphere and 1K in 4 km layers in the stratosphere sea surface temperature
- land surface temperature and infrared spectral surface emissivity
- humidity profiles and total precipitable water vapor
- fractional cloud cover, cloud spectral infrared emissivity, and cloud-top pressure and temperature
- total ozone column density and column density in three layers of the atmosphere
- trace gas column densities (e.g., CH_4 and CO) and where possible in various layers within the atmosphere

In this document we present the theoretical basis of the AIRS Level 2 Products Algorithm. Many products are presented in one document because of the basic structure and approach of the Level 2 Products Algorithm. In order to achieve the basic requirement of temperature profile accuracy of 1K in 1 km thick tropospheric layers, a multi-spectral simultaneous retrieval of both the atmospheric thermodynamic state and atmospheric composition is attempted. Hence the Level 2 Products refer to the basic thermodynamic variables and trace gas abundance that control the outgoing infrared radiance.

The algorithm described in this document will be implemented as the AIRS Level 2 Product Generation Executive (PGE) at the Goddard Space Flight Center Distributed Active Archive Center. It does not describe how the implementation will be made to meet the operational weather forecasting needs of NOAA where timing is of a paramount importance. However, the choice of algorithms and the structure of the Level 2 PGE chosen by the AIRS Science Team, contains the flexibility and options to eliminate steps as necessary to satisfy NOAA operational needs.

We consider this document to define the at-launch algorithm and refers to the corresponding AIRS Level 2 PGE. We expect that refinements will be made to the algorithms after launch when validation and testing begins with on-orbit data from the AIRS suite of instruments.

2. OVERVIEW AND BACKGROUND INFORMATION

2.1 Experimental objectives

The Earth's climate is a complex system with many components and feedback processes that operate on different time scales. The slow components involve the deep oceans, and permanent and semi-permanent ice and snow covers. Their response sets the pace for long-term climate trends and may introduce a delay of 50 years or more in the response of the climate system to external forcing. The fast components, whose scales range from hours to multiple seasons, encompass the atmosphere, upper ocean, the biosphere, as well as air-land and air-sea interactions. The fast components are coupled with and controlled by the atmosphere, which drives the whole Earth environment and determines the amplitude and geographical patterns of climate change. The atmosphere controls many feedback processes that involve the interaction of radiation with clouds, water vapor, precipitation and temperature. Thus, a knowledge of the properties of the atmosphere is important not only for understanding processes that occur within the atmosphere itself; but also for understanding the feedback mechanisms among the various components of the entire climate system. Atmospheric and surface measurements from AIRS will provide data about these interactions with unprecedented accuracy.

The ability of AIRS/AMSU/HSB to provide simultaneous observations of the Earth's atmospheric temperature, ocean surface temperature, and land surface temperature, as well as humidity, clouds, albedo, and the distribution of greenhouse gases, makes AIRS the primary EOS instrument for investigating several interdisciplinary issues to be addressed in Earth science. Among these issues are:

- Improving numerical weather prediction.
- Demonstrating seasonal to interannual predictions of the effects of El Nino and other transient climate anomalies.
- Characterizing the optical properties of atmospheric constituents, cloud and aerosols, in order to compute radiation fluxes.
- Monitoring variations and trends in the global energy and water cycles.

2.2 Historical perspective

The basic physics of a temperature sounding from earth orbit was published in the late 1950's (Kaplan 1959). Ten years later, and shortly after Chahine (1968) published the relaxation algorithm to invert spectral radiances for atmospheric temperature profiles, the first experimental temperature soundings from space were achieved using the Satellite Infrared Radiation Spectrometer (SIRS) on NIMBUS-4. This was a seven channel grating spectrometer with a spectral resolution ($\lambda/\Delta\lambda$) of 100 in the 15 μm CO_2 band (Wark and Hilleary 1969). The presence of clouds in the field-of-view posed a major challenge. Smith (1968) published a monograph on this topic and proposed a numerical technique, the N* parameter, for "cloud-clearing". Clouds become optically thick much quicker in the infrared (15 μm = 0.0015 cm) than at 57 GHz (0.5 cm) used in microwave sounding. Staelin *et al.* (1975a) demonstrated the capability to sense atmospheric temperature within and below clouds in the microwave with the Nimbus-E Microwave Sounder (NEMS). Unfortunately, the mid- to lower-tropospheric vertical resolution achievable in the microwave is inferior to that achievable in the 4.3 μm CO_2 band (see Table 2.1). A physical basis for "cloud-clearing" infrared radiances was proposed by Chahine (1974). Smith et *al.* (1978) demonstrated the use of the N* technique with the VTPR on the NIMBUS-5 satellite. Aumann and Chahine (1976) and Chahine *et al.* (1977) demonstrated temperature sounding of partly cloudy atmospheres using 4.3 μm CO_2 and 11 μm window channels. A cloud-clearing technique combining infrared and microwave data is now applied routinely in the NOAA operational sounding system as well as at NASA Goddard Space Flight Center (Susskind *et al.* 1984). This method takes advantage of the fact that, to first order, the microwave data are not affected by most types of clouds. It makes the assumption that the horizontal inhomogeneity in the scene due to clouds is much larger than the inhomogeneity due to temperature profile changes compared to the scale of the microwave field-of-view. By 1978, the HIRS-2 sounder (Smith, *et al.*, 1979), a radiometer with 19 channels between 3.7 μm and 15 μm and a spatial resolution of about 17 kilometers, combined with the Microwave Sounding Unit, MSU (a follow-up to NEMS), with 4 channels near the 57 GHz oxygen band, became the first of the TIROS Operational Vertical Sounders (TOVS). The NOAA Polar Orbiting

Sounding System was recently upgraded with the HIRS-3, AMSU-A and AMSU-B, launched on NOAA-15 in 1997.

2.3 Instrument characteristics

AIRS is a continuously operating cross-track scanning sounder, consisting of a telescope that feeds an echelle spectrometer. The spectrometer analyzes thermal infrared radiation between the wavenumbers of 650 cm^{-1} - 2700 cm^{-1}, with an average resolving power of 1200. This spectral region includes the important temperature sounding regions in the 4.2 and 15 μm CO_2 bands, water vapor sounding in the 6.3 μm water band and ozone sounding in the 9.6 μm region. AIRS has 2378 detector elements at the focal plane, arranged in several linear arrays. Each detector has a noise-equivalent difference temperature on the order of 0.2K (at 250K) seen in each 1.1° Instantaneous Field Of View (IFOV) as shown Figure 2.1.

During each scan, the rotating external mirror scans the underlying Earth between 49° either side of the nadir. In each scan line, there are 90 integration periods (Earth scenes or footprints), two views of dark space, one view of an internal radiometric calibration target, and one view of an internal spectral calibration target, for a total of 94 sets of measurements. The scan is repeated every 8/3 seconds. The downlink data rate from the AIRS instrument is 1.2 Mbit/sec.

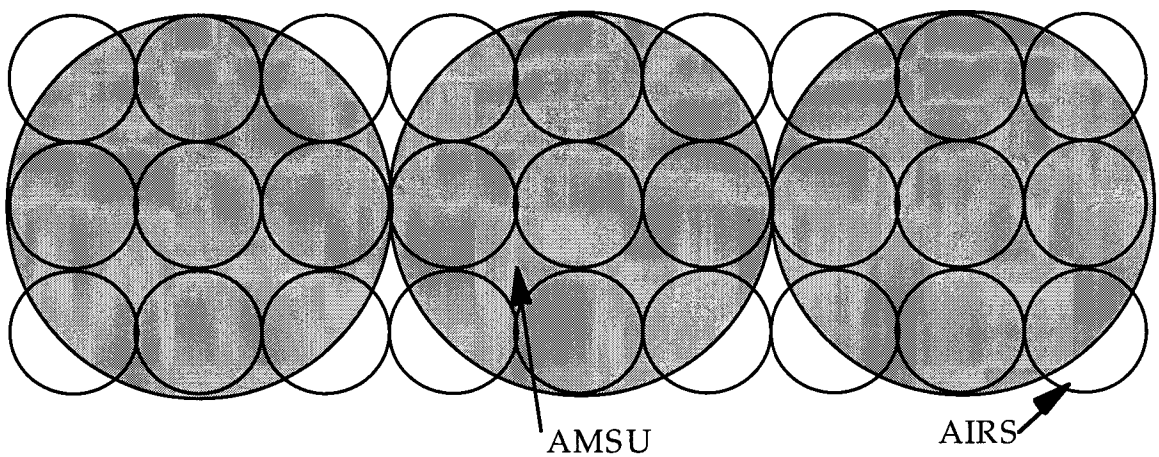

FIGURE 2.1 AIRS/AMSU SCHEMATIC FOOTPRINT PATTERN

Proper interpretation of AIRS data requires the use of co-located temperature and humidity data from a passive microwave sounder. Therefore, the Advanced Microwave Sounding Unit (AMSU) instrument will fly as part of the AIRS instrument complement on EOS. This instrument (which is flying on NOAA-15 and will also fly on the NOAA-L, -M, and -N weather satellites) is composed of two subsystems, AMSU and the Humidity Sounder of Brazil (HSB) (formerly the Microwave Humidity Sounder, MHS).

AMSU is a cross-track scanning multi-spectral microwave radiometer, with a 3.3° IFOV and 15 spectral channels (23 GHz - 90 GHz). Each cross-track scan produces 32 sets of measurements (30 Earth looks, 1 dark space calibration, and 1 internal blackbody radiometric calibration). The scan repeats every 8 seconds, being synchronized with every 3 AIRS scans (via the spacecraft master clock).

HSB is a cross-track scanning multi-spectral microwave radiometer, with a 1.1° IFOV and 4 spectral channels (150 GHz - 183 GHz). One channel of those of AMSU-B was eliminated by our Brazilian partners as a cost saving measure. Each cross-track scan produces 92 sets of measurements (90 Earth looks, 1 dark space calibration, and 1 blackbody calibration). The scan repeats every 8/3 seconds, being synchronized every third scan line.

The overlap between AIRS and AMSU footprints in the cross-track direction is illustrated in Figure 2.1. Note that HSB and AIRS will share approximately the same footprints. The current retrieval system produces one set of core products per AMSU footprint.

The AIRS instrument also contains four visible/near-IR channels working in the 0.4 to 0.95 micron range. With a nadir pixel size of 2.3 km, their primary function is to indicate when an infrared field-of-view (~15 km at nadir) is highly variable or contains low-clouds. See the Level 1b ATBD, Part 2, for a complete description of the visible/near-IR channels.

2.4 Measurement Strategy

During the past 20 years, considerable progress has been made in passive infrared remote sensing of temperature profiles. Currently, the combination of the High Resolution Infrared Sounder (HIRS) and the Microwave Sounding Unit (MSU) provides atmospheric temperature profiles with an average RMS error of approximately 2.0 K, with a vertical resolution of 3 to 5 km in the troposphere. This accuracy, however, falls short of the requirements for numerical weather prediction models. At present the need for improved sounding is accentuated by the fact that, during the past decade, models have evolved more rapidly than the capabilities of satellite-borne temperature sounders to supply accurate data. The inability of current sounders to match the vertical and horizontal resolution of general circulation models and difficulties in correcting for the

	Band	$\lambda/\Delta\lambda$	Half-width in scale heights	Remarks
Stratosphere	14.5 μm	100	2.4	VTPR/HIRS
	15.0 μm	1200	1.6	AIRS
	15.0 μm	10000	1.4	Wings of lines
	60 GHz	1000	1.3	AMSU
Troposphere	15.0 μm	100	1.6	VTPR
	60 GHz	1000	1.5	AMSU
	4.46 μm	100	1.3	HIRS
	4.18 μm	1200	0.69	AIRS
	4.18 μm	10000	0.60	Wings of lines

TABLE 2.1 CONTRIBUTION FUNCTION HALF WIDTH AS A FUNCTION OF SPECTRAL RESOLUTION

effects of clouds are the major deficiencies to be improved upon.

The limitation in vertical resolution is caused mainly by the broadness of the contribution functions (i.e., the weighting function multiplied by the Planck function - see Figure 2.2) of current instruments. When the contribution functions are broad, emitted

energy reaching the satellite in each channel will have components originating from a thick layer of the atmosphere, thereby making the discrimination of fine-scale vertical details practically impossible. This problem is exacerbated by the limited number of HIRS channels. Furthermore, because of the broad width of the contribution functions (see Table 2.1) and the difficulties in eliminating cloud contamination effects, as well as surface emissivity, O_3, H_2O, and other minor constituents, the RMS errors in the retrieved temperature profiles remain high. AIRS takes advantage of the ability to sound between lines and the temperature dependence in the high-J lines in the 4.18 μm CO_2 band to sharpen the weighting functions.

Experience with the current generation of sounders has shown that amalgamation of microwave and infrared data is a very useful combination for accurate elimination of most effects of clouds. Microwave observations in the 50 GHz region are not affected by

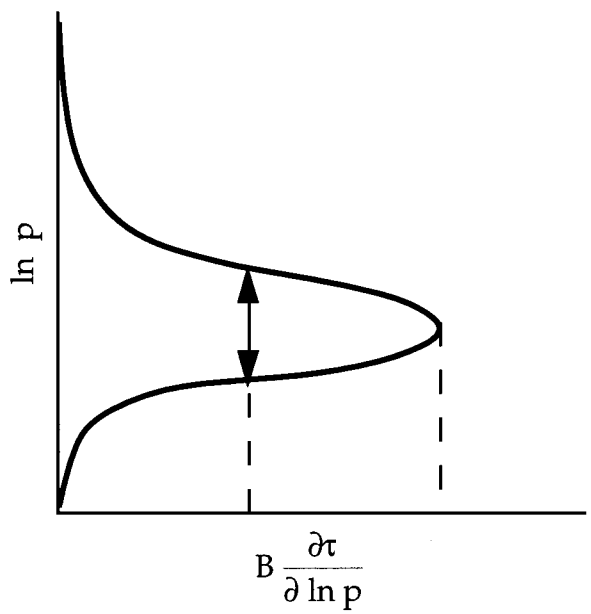

FIGURE 2.2 SCHEMATIC ILLUSTRATION OF A CONTRIBUTION FUNCTION AS A FUNCTION OF ATMOSPHERIC PRESSURE WHERE B IS THE PLANCK FUNCTION, τ IS THE TRANSMISSION TO SPACE, AND P IS THE PRESSURE

most types of clouds, which allows them to be used as an accurate filter to retrieve a variety of clear-column parameters. Some microwave channels are affected slightly by

the surface, especially over land, and are less effective for filtering out low clouds. Visible channels are needed here as a diagnostic to discriminate between low-level clouds and different types of terrain.

All AIRS/AMSU/HSB sounding channels, including the visible channels, must observe the same field-of-view at approximately the same time. This simultaneity requirement will insure that all the channels observe the same clouds and, consequently,

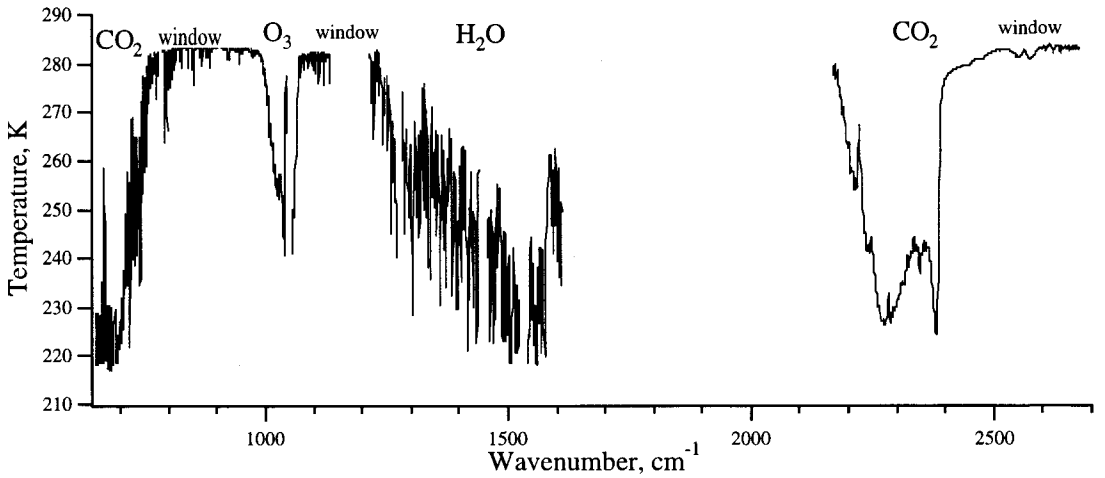

FIGURE 2.3 SIMULATED AIRS BRIGHTNESS TEMPERATURE SPECTRA FOR CLEAR CONDITIONS

Beginning wavelength $\lambda 1$	Ending wavelength $\lambda 2$	Beginning wavenumber μ_1	Beginning wavenumber μ_2
3.736	3.917	2676.37	2553.04
3.915	4.110	2554.34	2433.09
4.110	4.329	2433.09	2309.95
4.327	4.609	2311.02	2169.90
6.200	6.493	1612.83	1540.03
6.550	6.850	1526.62	1459.85
6.936	7.477	1441.84	1337.45
7.475	7.792	1337.88	1283.35
7.861	8.220	1272.18	1216.55
8.807	9.480	1135.42	1054.90
9.565	10.275	1045.48	973.24
10.275	10.985	973.24	910.33
11.070	11.751	903.31	850.98
11.743	12.685	851.56	788.33
12.799	13.746	781.32	727.50
13.738	14.553	727.92	687.13
14.667	15.400	681.79	649.35

TABLE 2.2 AIRS 17 DETECTOR ARRAY CUTOFF WAVELENGTHS (AS MEASURED IN A VACUUM)

the same cloud correction applies to all the frequencies.

Infrared Measurements

High spectral resolution in the infrared is key to achieving high vertical resolution. In the troposphere, the ability of microwave channels to provide high vertical discrimination is inherently weak. High J-lines in the R-branch of the 4.18 μm region, in which the CO_2 absorption coefficient increases rapidly with increasing temperature, provide the highest possible lower tropospheric vertical resolution of any part of the infrared spectrum and this resolution enhancement can be captured only through high spectral resolution measurements. In addition, a sufficiently large number of 15 μm infrared channels are required in the upper troposphere and adjacent lower stratosphere; and this requirement can also be satisfied as a consequence of high spectral resolution. High spectral resolution also permits selection of sounding channels not contaminated by water vapor lines or by emission from other active gases, and provides spectrally clean window-channels for surface measurements. The effect of the surface emission must be separated from the emission of the lower troposphere to provide accurate temperature profiles near the surface.

Channel No.	Center Frequency	Bandwidth (MHz)	Function
1	23.800 GHz	270	Water Vapor Burden
2	31.400 GHz	180	Surface Temperature
3	50.30 GHz	180	Surface Temperature
4	52.800 GHz	400	Surface Temperature
5	53.596 ±0.115 GHz	2x170	Tropospheric Temp
6	54.400 GHz	400	Tropospheric Temp
7	54.940 GHz	400	Tropospheric Temp
8	55.500 GHz	330	Tropospheric Temp
9	57,290.344 MHz (= f9)	330	Stratospheric Temp
10	f9 ±217 MHz	2x78	Stratospheric Temp
11	f9 ±322.2±48 MHz	4x36	Stratospheric Temp
12	f9 ±322.2±22 MHz	4x16	Stratospheric Temp
13	f9 ±322.2±10 MHz	4x8	Stratospheric Temp
14	f9 ±322.2±4.5 MHz	4x3	Stratospheric Temp
15	89.0 GHz	6000	Cloud Top/Snow

TABLE 2.3 AMSU CHANNEL SET (3.3-DEGREE BEAM DIAMETER)

The infrared channels to be used for retrieving such parameters as temperature and humidity profiles, ocean and land surface temperature, clouds and O_3, must be selected carefully. This is aided by the availability of narrow band-pass channels that are located away from unwanted absorption lines. It also takes advantage of the unique spectral properties of several regions, such as the high J-lines in the R-branch of the 4.3 μm CO_2 band and very clear window channels near 3.7 μm. A typical AIRS spectrum is presented in Figure 2.3 and Table 2.2 presents the precise AIRS array specifications.

Microwave Measurements

AMSU consists of 12 channels within the 50-60 GHz portion of the oxygen band to provide temperature and precipitation information. In addition, AMSU contains three window-channels at 24, 31 and 89 GHz to provide total precipitable water, cloud liquid water content and precipitation measurements. These channels will also be used to provide information on sea-ice concentration and snow cover. The 3-dB beam diameter

of AMSU is 3.3°, corresponding to about 50x50 km at nadir. The set of 15 microwave

Channel No.	Center Frequency (GHz)	Bandwidth (GHz)	Function
1*			
2	150.0	4000	Water vapor
3	183.31 ± 1.0	2x500	Water vapor
4	183.31 ± 3.0	2x1000	Water vapor
5	183.31 ± 7.0	2x2000	Water vapor

*Channel 1 (89 GHz) has been deleted for the HSB

TABLE 2.4. HSB (AMSU-B) CHANNEL SET (1.1-DEGREE BEAM DIAMETER)

channels is given in Table 2.3.

A second microwave instrument package will also be provided. The Microwave Humidity Sounder of Brazil (HSB), a copy of AMSU-B, contains one window-channel at 150 GHz to obtain high-resolution measurements of precipitation, snow cover and sea-ice with the same spatial footprint as AIRS. Three additional channels in the 183 GHz water vapor line will be used to improve the accuracy of atmospheric humidity profiles and total precipitable water vapor. The 3-dB beam diameter of HSB is 1.1°, corresponding to about 16 km at nadir. The full set of HSB (AMSU-B) channels and their specifications is given in Table 2.4.

Visible and Near-infrared Measurements

AIRS will also carry a small set of visible channels as a diagnostic aid in accounting for low-level clouds. In addition, the visible channels are needed to diagnose land surface inhomogeneities for the determination of surface temperature and emissivities and enhance the synergy with the Moderate Resolution Imaging Spectroradiometer (MODIS) on EOS. A set of visible and near-infrared channels between 0.4 and 0.95 μm is presented in Table 2.5. There are 36 spots within one AIRS infrared footprint.

Channel No.	Frequency Range (μm)	IFOV
1	0.40 - 0.44	1.1°/6
2	0.58 - 0.68	1.1°/6
3	0.71 - 0.98	1.1°/6
4	0.40 - 1.06*	1.1°/6

* warm silicon diode cutoff

TABLE 2.5. VISIBLE CHANNEL SET

Treatment of Clouds and Aerosols

Clouds are an important modulator of the infrared radiation emitted by the Earth surface and atmosphere. For this reason, the retrieval of basic cloud properties (cloud fraction, cloud-top height, and cloud-top temperature) is an integral part of the Level 2 algorithm. Our approach to dealing with clouds is an extension of those discussed by Smith (1968), Chahine (1974), and Chahine (1977). It involves a multi-step, iterative process to retrieve surface, atmospheric, and cloud properties, and is described fully in Section 5.2. Conceptually, the approach relies on the fact that cloud amount tends to vary appreciably among nearby 15 km AIRS footprints, but that other atmospheric and cloud properties (averaged within the footprints) are more uniform. This means that radiance differences between adjacent AIRS footprints are primarily caused by changes in cloud amount. Adjacent, multi-spectral observations can then be solved in a least squares sense for the infrared radiance that is common to the clear portions of all fields of view. This is called the "cloud-cleared radiance". Since the effect of clouds has been removed, atmospheric and surface properties can be retrieved from these radiances as if no clouds were present. Differences between the observed and cloud-cleared radiances can also be used to determine cloud properties. Note that AIRS does not need to have a cloud-free footprint in order to perform this analysis (but some point within one of the footprints must be clear), and that each footprint may contain multiple cloud layers. It should also be noted that existing systems (TOVS) have proven this approach to be effective. The

higher spectral resolution offered by AIRS, however, allows this technique to be exploited to a higher degree than ever before.

The power of the cloud-clearing approach is that minimal assumptions are made about the cloud's radiative properties while retrieving the state of the atmosphere (see Section 5.2). This flexibility means that any aerosols that interact with IR radiation can be treated as an unusual cloud layer. As with water clouds, there still must be a clear region somewhere within each AMSU footprint. Thus, narrow smoke plumes are not a problem, but a uniform dust layer extending more than 45 km across would get folded into the "clear-column" radiances and could degrade the atmospheric retrieval. To assess the impact of such horizontally widespread aerosols, we first note that stratospheric sulfuric acid aerosols are optically thin in the IR, except after large volcanic eruptions such as Mt. Pinatubo. Tropospheric anthropogenic aerosols are also optically thin to AIRS because of their small size. Examination of POLDER and AVHRR observations (Druze *et al.* 1999, Higurashi and Nakajima 1999) covering visible to IR wavelengths, indicates that at certain times of the year large dust storms in some deserts can create areas with appreciable optical depth. The Arabian Sea, off the coast of West Africa is one such region. Ackerman (1997) has previously found thermal-IR brightness temperature changes of 2 K may result from dust storms. We therefore conclude that aerosols may impact AIRS retrieval accuracy only in limited spatial and temporal regions. This will be further investigated after launch as part of the AIRS validation activities.

3 AIRS/AMSU/HSB DATA PRODUCTS

3.1 Standard Products

The AIRS Level 2 PGE produces (or has options to produce) four different files in EOS HDF Swath format available at launch:

- Standard Product
- Cloud-Cleared Radiance
- Support Product
- Quality Assessment Support Product

Successive files provide increasingly detailed information about the AIRS level 2 retrievals. It is worth noting that each file encompasses one 'granule' of AIRS data. Granules are formally defined as the smallest aggregation of data that is independently managed (i.e., described, inventoried, retrievable). An AIRS granule has been set as 6 minutes of data. This will normally correspond to approximately 1/15 of an orbit but exactly 45 scanlines of AMSU data or 135 scanlines of AIRS and HSB data.

The **Standard Product** consists of retrieved estimates of cloud and surface properties, plus profiles of retrieved temperature, water vapor, ozone and a flag indicating the presence of cloud ice or water. Estimates of the errors associated with these quantities will also be part of the Standard Product. The profile vertical resolution is 30 points total between 1000 mb and .02 mb; WMO pressure levels are used in the troposphere and lower stratosphere. The Standard Product contains quality assessment flags in addition to retrieved quantities. Its intended audience is climate and weather researchers with limited interest in the retrieval algorithm. The Standard Product will be generated at all locations atmospheric soundings are taken.

Cloud-Cleared Radiances are produced along with the AIRS Standard Product, as they are the radiances used to retrieve the Standard Product. Nevertheless, they are an order of magnitude larger in data volume than the remainder of the Standard Products and, many Standard Product users are expected to have little interest in the Cloud Cleared Radiance. For these reasons they are a separate output file, but like the Standard Product will be generated at all locations.

The **Support Product** includes higher vertical resolution profiles of the quantities found in the Standard Product, plus intermediate output (e. g., microwave-only retrieval), research products such as the abundance of trace gases, and detailed quality assessment information. The Support Product profiles contain 100 levels between 1100 and .016 mb; this higher resolution will simplify the generation of radiances using forward models, though the vertical information content is no greater than in the Standard Product profiles. The intended users of the Support Product are researchers interested in generating forward radiance, or in examining research products, and the AIRS algorithm development team. The Support Product will be generated at all locations as Standard Products.

The final AIRS Level 2 data product is the **Quality Assessment Support Product.** This output is intended to provide insight into the detailed workings of the AIRS retrieval algorithm, and will contain a large number of intermediate retrieved quantities, their estimated uncertainties, and associated quality assessment parameters. Because of its large size, the quality assessment Support Product will be generated only at those locations where the AIRS retrieval algorithm is known to be functioning poorly, based upon quality assessment information. The intended users of the Quality Assessment Support Product are the AIRS retrieval algorithm development team, and scientists validating the performance of these algorithms, primarily at the Team Leader Science Computing Facility (TLSCF) at JPL. It will not be generated at the GSFC DAAC.

3.2 Research Products

AIRS will produce a number of research products that will be developed and tested after launch. Primary among these are trace constituent profiles of CO and CH_4, Outgoing Longwave Radiation (OLR) and Clear Sky Outgoing Radiation (COLR), and possibly total CO_2 burden. These are described briefly below.

3.2.1 OLR and COLR

The ability to compute OLR and COLR from sounding data was demonstrated with the TOVS Pathfinder Path A Dataset (Susskind et al., 1997; Mehta and Susskind, 1999a;

Mehta and Susskind, 1999b). The approach used for TOVS data is to compute total OLR using a forward model and the retrieved quantities: surface skin temperature, temperature-, moisture-, O_3-profiles, cloud top pressure and radiatively effective cloud fraction (given by the product of the portion of the scene covered by clouds and the cloud emissivity at 11 μm). COLR is computed analogously, but setting the effective cloud fractions to zero. It represents the radiation that would have gone to space if no clouds were present. The TOVS Pathfinder OLR and COLR has been shown to be at least comparable to me ERBE products.

AIRS OLR will be computed in an analogous way, but will also take into account the surface spectral emissivity, the cloud spectral emissivity, and trace constituent profiles. Comparison of AIRS OLR and COLR with values determined from CERES will tend to validate in a radiative sense the AIRS products, and will also cross validate the CERES values. More importantly, AIRS will be able to explain the spatial and temporal variability of the CERES OLR and COLR in terms of the variability of the geophysical parameters on which they depend.

3.2.2 Trace Gases

Preliminary studies, presented at AIRS Science Team meetings, have shown that the AIRS instrument will be capable of measuring carbon dioxide (CO_2), methane (CH_4), and carbon monoxide (CO). The retrieval methodology is identical to the final product retrieval, discussed in section 5.4. We will attempt the trace gas retrievals after all other AIRS products have been determined and validated. CO_2 and CH_4 products must have an accuracy better than a fraction of a percent to be useful for seasonal and climate studies. Also, the CO retrieval will be difficult due the small number of AIRS channels sensitive to CO. We expect that only cloud-free AMSU footprints will be used to generate a trace-gas products and that thses may be spatially or temporally averaged over 100's of km's to achieve the desired accuracy.

4 THE FORWARD PROBLEM

In the following, atmospheric radiative transfer or the 'forward problem' will be discussed. Because the retrieval methodology utilized by the AIRS team depends on the ability to accurately determine the outgoing radiance, particular attention will be paid to errors in the spectroscopy and errors in modeling the outgoing radiation -- the rapid forward model. To overcome these error sources, a process known as tuning is used to remove systematic effects and is described in section 5.1.

4.1 Radiative Transfer of the Atmosphere in the Microwave

At the frequencies measured by AMSU and HSB, the most important absorbing gases in the atmosphere are oxygen and water vapor. The oxygen molecule has only a magnetic dipole moment, and its lines are intrinsically much weaker than those which result from the electric dipole of water vapor; however, the much greater abundance of oxygen in the atmosphere more than compensates for this difference. When clouds are present, liquid water also plays a role in radiative transfer. However, fair-weather cirrus composed of ice particles small compared to the wavelength are effectively transparent to microwave radiation.

4.1.1 Oxygen

The dipole moment of O_2 is due to two unpaired electron spins and thus it can be expressed in terms of fundamental constants. Hence, the intensities of the O_2 spin-rotation transitions are among the most precisely calculable of any molecule. The values used are from the JPL Submillimeter, Millimeter, and Microwave Spectral Line Catalog (Poynter and Pickett, 1985). These transitions comprise approximately 30 lines between 50 and 70 GHz and an isolated line at 118.75 GHz (which is not observed by AMSU or HSB). Several groups have measured the pressure-broadened widths of the lines in the 50-70 GHz band. The most accurate measurements are probably those of Liebe *et al.*, (1977) and Liebe and Gimmestad (1978), where the errors were estimated to be $\leq 1\%$ for most of the stronger lines.

The characteristic of oxygen's microwave spectrum that introduces difficulty for construction of models is the significant degree of line mixing. In the Millimeter-wave Propagation Model (MPM92) (Liebe, *et al.,* 1992), line mixing was treated by a first-order expansion in pressure. The coefficients for this expansion were determined by a constrained linear fit to laboratory measurements made on an O_2 - N_2 mixture over the frequency range of 49-67 GHz and the temperature range 279-327 K, with a noise level of approximately 0.06 dB/km. Within that range, the model represents the measurements to $\leq$ 0.2 dB/km (see for example, Figure 4.1.1). It is possible that extrapolation to colder temperatures introduces larger errors. Recent measurements from the NASA ER-2 at 52-56 GHz seem to be in agreement with the model, however. There is also some indication from aircraft and ground-based atmospheric measurements that model errors in oxygen zenith opacity may reach 10-20% near 30 and 90 GHz. However, the main absorber at those frequencies is water.

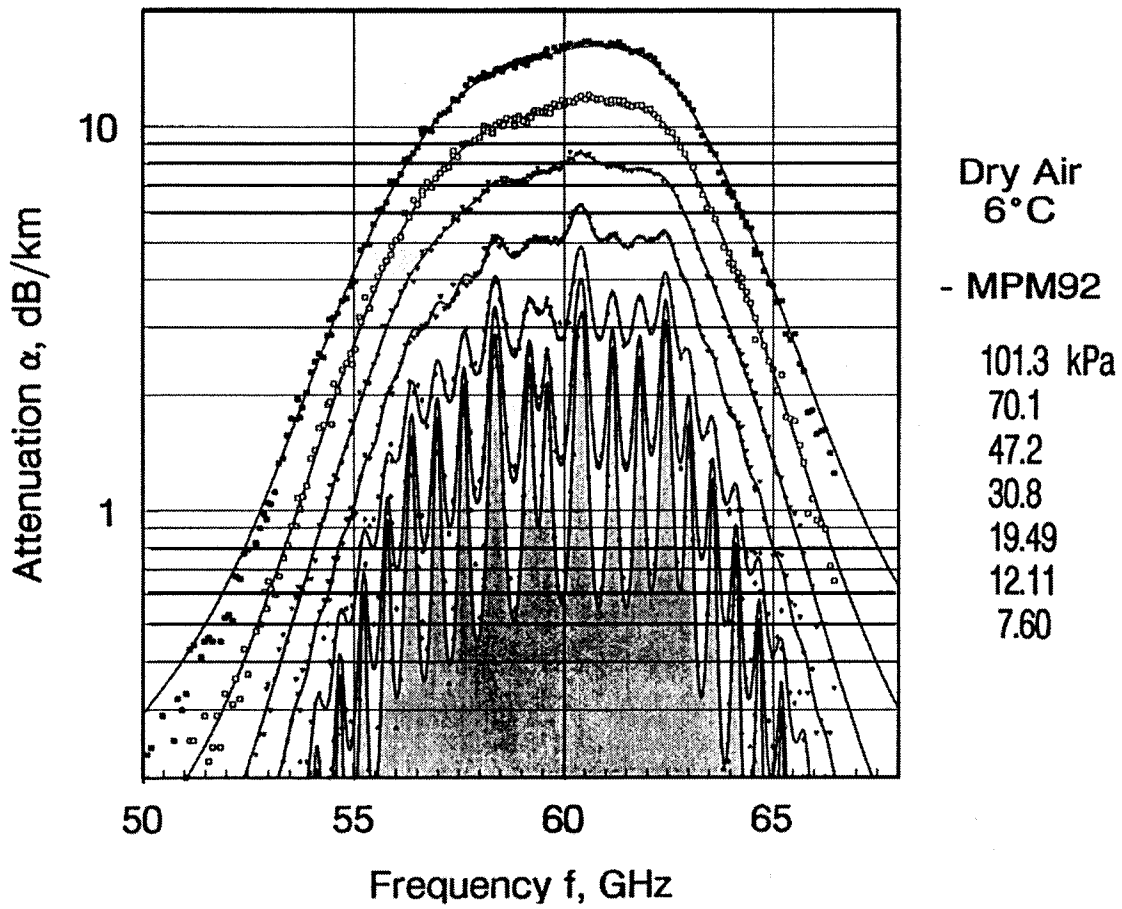

FIGURE 4.1.1. ATTENUATION MEASUREMENTS OF TEST AIR AT 279K AND 7 PRESSURES, COMPARED WITH THE MPM 92 MODEL (FROM LIEBE *ET AL*, 1992).

4.1.2 Water Vapor

Water has a weak rotational line at 22.23 GHz that is semi-transparent at normal atmospheric humidity, and a much stronger, opaque line at 183.31 GHz. Intensities of these lines have been calculated and tabulated by Poynter and Pickett (1996 version of JPL line catalog) and Rothman *et al.*, (1992) (HITRAN), among others. The HITRAN intensities are used here. For the 22-GHz line, the JPL intensity is higher than the HITRAN value by 0.3%. There is a measurement by Liebe *et al.*, (1969) (estimated error 0.3%) which is 3.5% lower than the HITRAN value. At 183 GHz, the JPL line intensity is 0.1% higher than HITRAN. Widths have been measured by Liebe *et al.*, (1969) and Liebe and Dillon (1969) at 22 GHz with estimated uncertainty of 1% for both self and

foreign-gas broadening; and by Bauer *et al.*, (1989) at 183 GHz, with uncertainties of 0.5% for self-broadening and 1.6% for foreign-gas broadening. However, Gamache *et al.* (1994) concluded from a survey of measurements of many H_2O lines that, in general, measured line widths should be considered to have uncertainties of 10-15%.

At frequencies away from these two lines, microwave absorption by water vapor is predominantly from the continuum, which is attributed to the low-frequency wing of the intense infrared and submillimeter rotational band lines. In the microwave part of the spectrum, the foreign-broadened component of the continuum is stronger than the self-broadened component, for atmospheric mixing ratios. Measurements of continuum absorption as a function of temperature have been made at various frequencies by Liebe and Layton (1987) and by Bauer's group (Godon, *et al.*, 1992; Bauer *et al.*, 1993, 1995). There are also numerous measurements at single temperatures and frequencies in the laboratory, and in the atmosphere where temperature and mixing ratio are variable. The measurements do not present an entirely consistent picture. It has been argued by Rosenkranz (1998b) that the most satisfactory overall agreement with laboratory and atmospheric measurements of the water continuum is obtained with a combination of the foreign-broadened component from MPM87 (Liebe and Layton, 1987) with the self-broadened component from MPM93 (Liebe et al., 1993). The combined model is used here.

4.1.3 Liquid Water

It is useful to distinguish between precipitating and non-precipitating clouds with respect to their interactions with microwaves. Over the range of wavelengths measured by AMSU and HSB, non-precipitating droplets (with diameters of 50 μm or less) can be treated using the Rayleigh small-droplet approximation. In this regime, absorption is proportional to the liquid water content of the air, and scattering can be neglected. The model for the dielectric constant limits the accuracy of these calculations. The double-Debye model of Liebe *et al.*, (1991) is used here; it has an estimated maximum prediction error of 3% between 5 and 100 GHz, and 10% up to 1 THz. Precipitation, on the other hand, requires Mie theory to calculate both absorption and scattering. The latter is

generally not negligible, and is the dominant term at some wavelengths. In the case of convective storms, scattering from ice at high altitudes is often the most important process. In simulations so far we have not considered scattering, and the rapid transmittance algorithm uses only the small-droplet approximation for cloud liquid water.

4.1.4 Rapid Transmittance Algorithm

The physical retrieval algorithms used for AIRS/AMSU/HSB do radiative transfer calculations for each profile and hence need a computationally efficient transmittance algorithm. The microwave algorithm computes an effective channel transmittance between two adjacent pressure levels as

$$\langle \tau(P_1, P_2) \rangle = \exp\left[-(\alpha + \beta\rho_V + \gamma\rho_L)\right], \tag{4.1.1}$$

where ρ_V is the water vapor column density of the (P_1, P_2) layer, ρ_L is its liquid water column density, and the coefficients α, β, γ, are calculated for each layer and channel. They implicitly depend on temperature, pressure, and the angle of observation; β also depends implicitly on ρ_V. For AMSU channel 14, α has a weak dependence on the local geomagnetic field. The magnetic field is currently calculated by a fifth-order spherical-harmonic representation that has an accuracy of a few microteslas. The coefficient α includes the opacity due to O_2 and a small contribution from pressure-induced absorption by N_2. Parameterization of the coefficients uses approximations described by Rosenkranz (1995) for oxygen-band or window-type channels. The oxygen-band-channel coefficients are computed on a set of fixed pressure levels and then linearly interpolated to the pressure levels of the present retrieval, which can be variable (as is the case for the surface pressure). Window-channel coefficients use analytic approximations for far-wing line and continuum absorption. Channels near the two water lines (AMSU channel 1 and HSB channels 3-5) use a Lorentzian-line calculation for the nearby line, with the contributions of other lines treated in the same way as for a window channel (see Rosenkranz, 1998a). The local water-line parameters, the water continuum, and the liquid-water absorption are interpolated from a table as functions of temperature.

The retrieval algorithm described in Section 5.2 also makes use of the derivatives $d\alpha/dt$ and $d\beta/d\rho_v$, which are computed in the rapid algorithm by appropriate analytic expressions corresponding to the local-line and continuum components.

The transmittance of multiple layers is calculated by taking the product of the transmittances for each layer. This transmittance is then used in the radiative transfer equation to compute brightness temperature:

$$\Theta = \int_0^{P_s} T(P) < d\tau(0,P) > + \varepsilon T_s < \tau(0,P_s) > + (1-\varepsilon) < \tau(0,P_s) > \int_0^{P_s} T(P) < d\tau(P_s,P) > + (1-\varepsilon)\Theta_c < \tau(0,P_s) >^2 \quad (4.1.2)$$

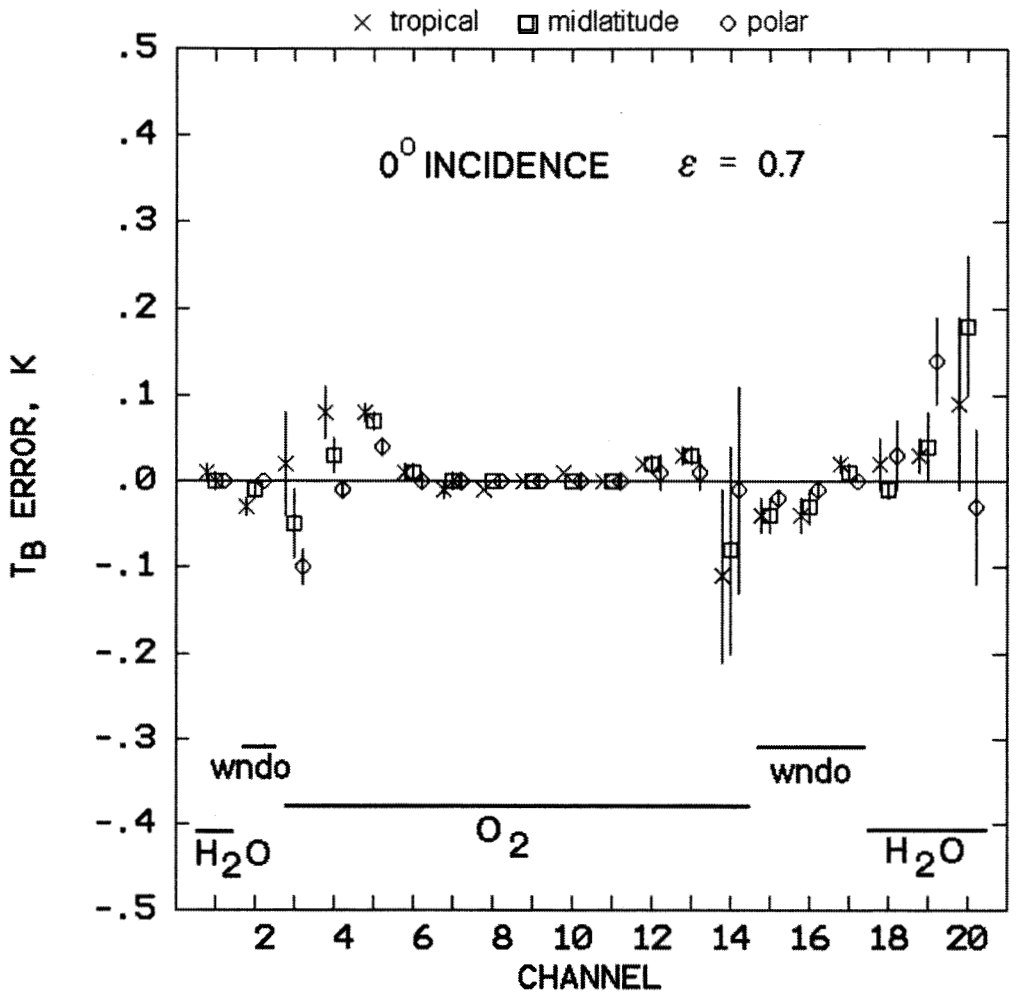

FIGURE 4.1.2. BRIGHTNESS TEMPERATURE ERRORS (RAPID ALGORITHM MINUS LINE-BY-LINE ALGORITHM) FOR AMSU CHANNELS (1-15) AND HSB CHANNELS (16-20). VERTICAL LINES INDICATE ± 1 STANDARD DEVIATION. HERE, ε IS THE SURFACE EMISSITIVITY.

where T(P) is atmospheric temperature at level P, T_s and P_s are the surface temperature and pressure, Θ_c is the cosmic background brightness temperature, and ε is the emissivity of the surface, assumed to be smooth here.

The ability of the rapid algorithm to approximate a line-by-line calculation was tested on a set of 300 profiles from the TOVS Initial Guess Retrieval (TIGR) (Chedin *et al.*, 1985) ensemble. The first 100 profiles from each of the tropical, mid-latitude, and polar groups were used. Figure (4.1.2) shows brightness temperature errors (mean ± 1 standard deviation) at nadir, with surface emissivity = 0.7. For the channels that are not opaque (1-5, 15-17, 19 and 20), these brightness temperature errors depend on surface

emissivity. The value $\varepsilon = 0.7$ is typical of ocean at the highest frequencies, and intermediate between ocean and land at the lowest frequencies. Errors for higher-emissivity land surfaces are smaller than in Figure 4.1.2. The errors for channel 14 include the consequences of the magnetic field approximation.

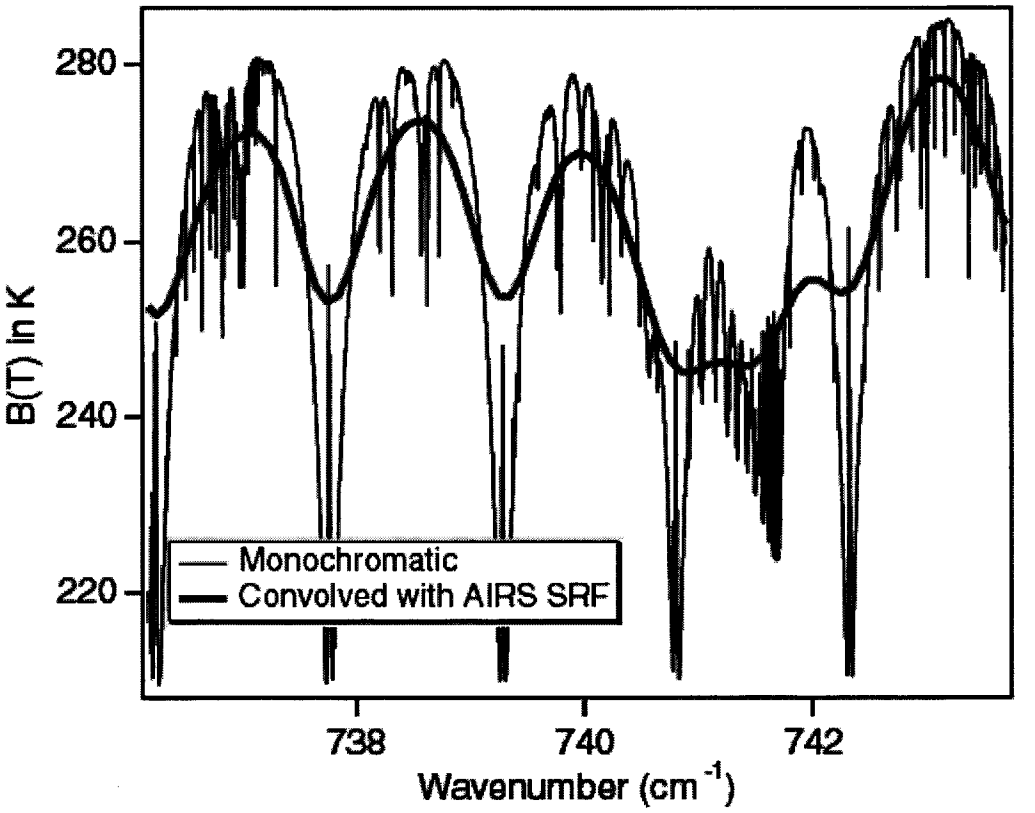

FIG. 4.2.1 COMPARISON OF MONOCHROMATIC BRIGHTNESS TEMPERATURES TO BRIGHTNESS TEMPERATURES CONVOLVED WITH THE AIRS SPECTRAL RESPONSE FUNCTION.

4.2 Radiative Transfer of the Atmosphere in the Infrared

Physical retrievals of atmospheric parameters attempt to minimize the difference between computed and observed channel radiances. The accuracy of the retrieval is therefore directly related to the accuracy of the computed radiances. AIRS measures the convolution of the up-welling monochromatic radiances with the instrument spectral response function (SRF). An exact calculation of the observed radiances therefore requires the convolution of simulated monochromatic radiances. These computed radiances are complicated functions of the atmospheric state (temperature, pressure, gas amount), the gas transmittances, and the AIRS SRFs. Since the atmospheric emission lines can have widths as small as ~0.001 cm^{-1}, the wavenumber grid scale for the radiance calculation must have a similar spacing. This small grid spacing, combined with the time-consuming SRF convolutions, makes a monochromatic calculation of radiances orders of magnitude too slow for practical use. Instead, we must use a fast radiative

transfer model that is based on appropriately convolved atmospheric transmittances for each spectral channel. Then the radiative transfer can be performed on a per-channel basis rather than on a finely spaced monochromatic wavenumber grid.

The starting point for understanding the AIRS radiative transfer algorithm (AIRS-RTA) is the monochromatic radiative transfer equation. The monochromatic radiance leaving the top of a non-scattering atmosphere is

$$R(\nu,\theta) = \varepsilon_S B(\nu,T_S)\tau(\nu,p_S,\theta) + \int_{\ln p_S}^{\ln p_\infty} B(\nu,T)\frac{\partial\tau(\nu,p,\theta)}{\partial \ln p} d\ln p + \rho_S H_{sun}\tau(\nu,p_S,\theta)\tau(\nu,p_S,\theta_{sun})\cos(\theta_{sun}) + R_d, \quad (4.2.1)$$

where $B(\nu,T)$ is the Planck function emission at frequency ν and temperature T, $\tau(\nu,p,\theta)$ is the transmittance between pressure p and the satellite at viewing angle θ, and T_s, ε_s, and ρ_s refer to the Earth's surface temperature, emissivity, and reflectivity respectively, and R_d is the reflected downwelling thermal radiance. The solar radiance entering at the top of the atmosphere is represented by H_{sun}. The dependence of temperature and angle on pressure (altitude) has been suppressed in the above equation, as well as the dependence of the transmittances on temperature and gas abundance. Due to lack of space, a detailed explanation of our implementation of the reflected solar and reflected thermal terms will not be given here.

The AIRS-RTA allows the integration of the radiative transfer equation over 100 atmospheric layers to be performed in a discrete form. Ignoring the last two terms in Equation (4.2.1), a discrete form of the radiative transfer equation can be written conveniently as

$$R_{meas} = \int R(\nu) f(\nu-\nu_o) d\nu = \int (\varepsilon_S B(T_S)\tau_{Z,N} + \sum_{i=1}^{N} B(T(i))(\tau_{Z,i-1} - \tau_{Z,i}) f(\nu-\nu_o)) d\nu \quad (4.2.2)$$

where the atmospheric layers are numbered from space to the surface, 1 to N respectively. $B(T(i))$ is the Planck emission for layer i at temperature T(i), $\tau_{z,i}$ is the transmittance from layer i to space, inclusive, and $f(\nu-\nu_o)$ is the AIRS SRF for the channel

centered at ν_o. The emissivity and Planck function are easily removed from inside the integral, leaving us with the channel-averaged form of the radiative transfer equation,

$$R_{meas} = \varepsilon B(T_s)\tau_{z,N} + \sum_{i=1}^{N} B(T(i))(\tau_{z,i-1} - \tau_{z,i}) \qquad (4.2.3)$$

where all terms now represent appropriate channel-averaged quantities.

The polychromatic approximation introduced in the above relation replaces the monochromatic layer-to-space transmittances with transmittances convolved with the SRFs. This in effect convolves the outgoing radiances, allowing us to do radiative transfer at just a single frequency per channel. In most cases, the AIRS channel radiances calculated from the above equation using convolved layer-to-space transmittances differ from the convolved monochromatic AIRS channel radiances by ≤ 0.05 K, assuming you had perfect layer-to-space convolved transmittances in hand.

Figure 4.2.1 illustrates the large difference in spectral resolution between the upwelling monochromatic radiation and an AIRS brightness temperature spectrum. Because of this large difference in spectral resolution you cannot derive the layer-to-space transmittances directly from the product of the convolved layer transmittances since you have lost Beer's law by doing the convolution. Overcoming this problem is one of the major issues in the development of a model for fast, parameterized, convolved layer transmittances.

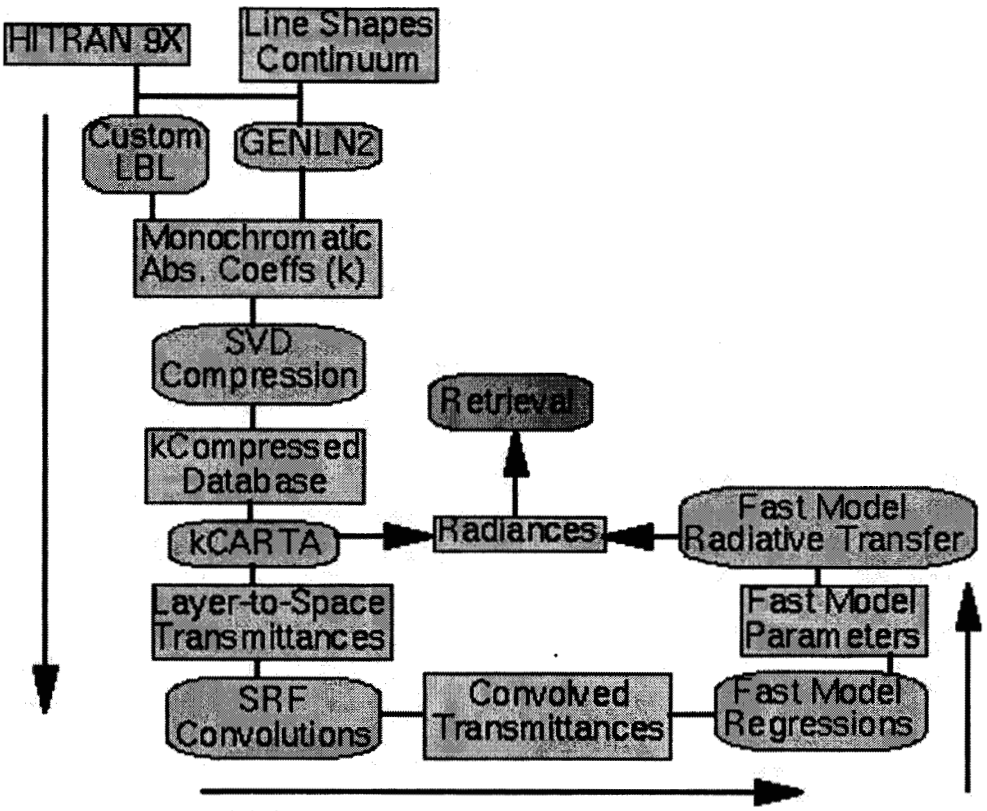

FIG. 4.2.2 FLOW DIAGRAM FOR DEVELOPMENT OF THE AIRS-RTA

In the following sections we discuss the major issues in developing the AIRS-RTA, which include:

(1) forming a discrete grid for integrating the radiative transfer equation,
(2) parameterizing the layer transmittances as a function of the atmospheric state,
(3) the spectroscopy needed to compute atmospheric transmittances,
(4) the line-by-line algorithm used to generate the monochromatic transmittances
(5) the AIRS spectral response functions

The flowchart shown in Figure 4.2.2 outlines the flow of activities needed to develop the AIRS-RTA, which is discussed in the following text.

4.2.1 AIRS Atmospheric Layering Grid

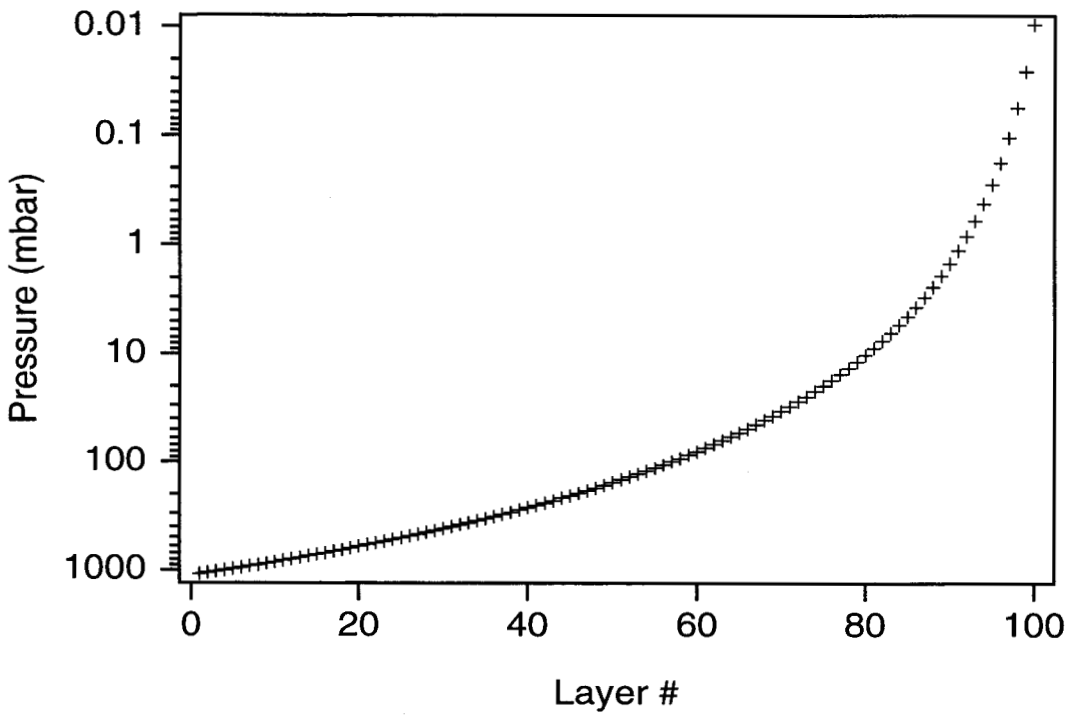

FIGURE 4.2.3: AIRS-RTA MODEL PRESSURE LAYER STRUCTURE. (NOTE: LAYER NUMBER IS INVERTED IN THIS FIGURE COMPARED TO THE TEXT.)

The atmospheric pressure layering grid for the AIRS-RTA model was selected to keep radiative transfer errors below the instrument noise. Grid characteristics are a function of the spectral region(s) of observation, the instrument resolution, and instrument noise. The speed of the final fast transmittance model will depend on the number of layers, so excessive layering should be avoided.

Line-by-line simulations indicate some channels need a top layer with pressures as small as 0.01 mb, an altitude of ~ 80 km. The region of primary importance to AIRS is the troposphere and lower stratosphere, where layers on the order of 1/3 of the nominal 1 km vertical resolution of AIRS retrievals are desired. Smoothly varying layers facilitate interpolation and avoid large changes in layer effective transmittances. The following relation defines the pressure layer boundaries selected for AIRS:

$$P_i = (ai^2 + bi + c) \qquad (4.2.4)$$

where P is the pressure in millibars; i is the layer boundary index and ranges from 1 to 101; and the parameters a, b, and c were determined by solving this equation with the following fixed values: P_1 = 1100 mb, P_{38} = 300 mb, and $P_{101} = 5x10^{-3}$ mb. The 101 pressure layer boundaries in turn define the 100 AIRS layers. These layers vary smoothly in thickness from several tenths of a kilometer near the surface to several kilometers at the highest altitudes. Figure 4.2.3 displays a plot of this atmospheric layer structure.

4.2.2 Fast Transmittance Modeling

Over the years, a number of fast transmittance models have been developed for various satellite instruments [McMillin and Fleming, 1976; Fleming and McMillin, 1977; McMillin et al., 1979, 1995; Scott and Chedin, 1981; Susskind et al., 1983; Erye and Woolf, 1988; Chéruy et al., 1995]. However, some of these models only have been applied to the microwave region where the measured radiances are essentially monochromatic and easier to model. AIRS required a major new effort in the development of its RTA, some of the details of our model in its early stages can be found in Hannon et al. [1996]. The AIRS-RTA model has already been adopted by the EUMETSAT IASI Science Team (private communication, Marco Matricardi , ECMWF), and for GOES applications (private communication, Paul Van Delst, University of Wisconsin).

The AIRS-RTA most closely follows Susskind et al. [1983] by parameterizing the optical depths rather than transmittances for channels where the influence of water vapor is small. Channels sensitive to water vapor are modeled using a variant of the Optical Path TRANsmittance (OPTRAN) algorithm developed by McMillin et al. [1979, 1995]. The AIRS infrared fast model is thus a hybrid of both Susskind's approach and OPTRAN.

The AIRS-RTA model actually produces equivalent channel averaged optical depths, k's, which are related to the layer transmittances, τ 's, by $\tau = \exp(-k)$. The optical depth is the product of the absorption coefficient and the optical path. For AIRS, a fast model for k is much more accurate than a model that directly returns layer τ 's. k's are computed for

each of the 100 atmospheric layers used for AIRS radiative transfer. The current AIRS-RTA model allows water, ozone, methane, carbon monoxide, carbon dioxide, the temperature, and local scan angle to vary. All other gases are treated as 'fixed' gases. These gases are "fixed" in the sense that we only need to parameterize their dependence on temperature, not amount. Although the observed radiances are primarily sensitive to temperature via the Planck function, the temperature dependence of the transmittances is also important.

The following discussion outlines the development of a parameterization of the convolved layer transmittances as a function of the atmospheric state. Most of the complications of this parameterization arise from the loss of Beer's law, which forces us to introduce terms in the transmittance parameterization for a given atmospheric layer that depend on layers above the particular layer under consideration. These parameterizations, which are functions of the atmospheric profile, are derived from least-squares fits to a statistical set of atmospheric profiles in order to ensure that we can faithfully produce the appropriate transmittances under all atmospheric conditions. We call this statistical set of profiles our "regression profiles".

4.2.2.1 Breakout of Gases

Once the atmospheric layering grid and regression profiles (see later discussion) are selected, the monochromatic layer-to-space transmittance can be calculated. The gases are distributed into sub-groups that are either fixed or variable. The details of how the transmittance model simultaneously handles several variable gases is somewhat complicated and beyond the scope of this document. For simplicity, this discussion is restricted to fixed gases (F), water vapor (W), and ozone (O). The breakout of the other variable gases is similar. The monochromatic layer-to-space transmittances for the 48 regression profiles are calculated for each pressure layer, grouped into the following three sets, and convolved with the AIRS SRF,

$$\begin{aligned} F_{\infty,l} &= \tau_{\infty,l}(\text{fixed}) \\ FO_{\infty,l} &= \tau_{\infty,l}(\text{fixed} + \text{ozone}) \\ FOW_{\infty,l} &= \tau_{\infty,l}(\text{fixed} + \text{ozone} + \text{water}) \end{aligned} \tag{4.2.5}$$

Water continuum absorption is excluded since it varies slowly with wavenumber and does not need to be convolved with the AIRS SRF. In addition, separating out the water continuum improves our fit of the local line water transmittance. Later, the water continuum is factored into the total transmittance as a separate term.

For each layer l, the convolved layer-to-space (∞,l) transmittances are ratioed with transmittances in the layer above, l - 1, to form effective layer transmittances for fixed (F), water (W), and ozone (O) as follows:

$$\begin{aligned} F_l^{eff} &= \frac{F_{\infty,l}}{F_{\infty,l-1}} \\ O_l^{eff} &= \frac{FO_{\infty,l}}{FO_{\infty,l-1}} \div \frac{F_{\infty,l}}{F_{\infty,l-1}} \\ W_l^{eff} &= \frac{FOW_{\infty,l}}{FOW_{\infty,l-1}} \div \frac{FO_{\infty,l}}{FO_{\infty,l-1}} \end{aligned} \tag{4.2.6}$$

Forming these ratios is the above manner reduce the errors inherent in separating the gas transmittances after the convolution with the instrument spectral response function. The total effective layer transmittance can be recovered as follows,

$$FOW_l^{eff} = F_l^{eff} * O_l^{eff} * W_l^{eff} = \frac{FOW_{\infty,l}}{FOW_{\infty,l-1}} \tag{4.2.7}$$

The convolution of a product of terms is in general not the same as the product of the terms convolved individually. However, the above formulation guarantees the product of all the layer transmittances from layer l to ∞ exactly returns $FOW_{\infty,l}$, if the layer transmittances are exact.

The zeroth layer transmittance (i.e. when l - 1 = 0) is taken to be exactly 1.0. The negative logarithm of these layer effective transmittances is taken to get effective layer optical depths,

$$\begin{aligned} k_{fixed} &= -\ln(F_{eff}) \\ k_{water} &= -\ln(W_{eff}) \\ k_{ozone} &= -\ln(O_{eff}) \end{aligned} \tag{4.2.8}$$

which become the dependent variables in the fast model regression.

4.2.2.2 Predictors

The independent variables in the fast model regression, called the predictors, are a set of variables relating to the atmospheric profile. The optimal set of predictors used to parameterize the effective layer optical depth depends upon the gas, the instrument SRFs, the range of viewing angles, the spectral region, and even the layer thicknesses. In short, no one set of predictors is likely to work well in every case. Finding the set of predictors which give the best results is, in part, a matter of trial and error. However, there are some general trends.

For an instrument such as AIRS with thousands of channels, it is difficult to develop individual optimal predictors for each channel. The AIRS-RTA uses seven sets of predictors, each corresponding with a subset of channels. These sets of predictors were determined by extensive trial and error testing, as well as consideration of the relative importance of the variable gases in each channel. Supplemental sets of predictors are used for OPTRAN water, the water continuum, and variable CO_2.

The regression is prone to numerical instabilities if the values of the predictors vary too greatly. Consequently, we follow the usual practice of defining the predictors with respect to the values of a reference profile, either by taking a ratio or an offset. There is also a danger of numerical instability in the results of the regression, due to the interaction of some of the predictors. Sensitivity of the output to small perturbations in the predictors is avoided by systematic testing, but there are practical difficulties in detecting small problems since we are performing on the order of 1 million regressions.

As an example, the predictors for the fixed gases for one of the seven sets are shown:

$$\begin{array}{lll} 1)a & 2)a^2 & 3)aT_r \\ 4)aT_r^2 & 5)T_r & 6)T_r^2 \\ 7)aT_z & 8)aT_z/T_r & \end{array} \qquad (4.2.9)$$

where a is the secant of the local path angle, T_r is the temperature ratio $T_{profile}/T_{reference}$, and T_z is the pressure weighted temperature ratio above the layer

$$T_Z(l) = \sum_{i=2}^{l} P(i)(P(i) - P(i-1))T_r(i-1) \qquad (4.2.10)$$

where P(i) is the average layer pressure for layer l. The predictors for the variable gases can involve more complicated dependencies on the gas and the pressure weighted gas ratios above the layer, similar to the temperature term defined above. Note that terms like T_z (or W_z, etc. for the variable gases) make the layer l transmittance dependent on the temperature (or gas amounts) in the layers above l.

4.2.2.3 Regressions for Fast Transmittance Parameters

The accuracy of radiative transfer calculations made with the AIRS-RTA model was improved significantly by weighting the variables prior to performing the regression. Radiative transfer is insensitive to layers for which the change in layer-to-space transmittance across the layer is approximately zero. This occurs when either the layer effective transmittance is approximately unity, or the layer-to-space transmittance is approximately zero. Therefore, the data going into the regression is not all of equal importance to the final accuracy of radiative transfer calculations made with the model. We found it useful to weight the data in terms of both its effective layer optical depth as well as the total optical depth of all the layers above the layer under consideration.

The spectral dependence of the fitting errors are shown in Figure 4.2.4 and a histogram of these errors in Figure 4.2.5. The errors are calculated with respect to the regression profile set, comparing the RMS errors between the brightness temperatures of input data and the AIRS-RTA model calculated values. These graphs including errors from all six angles used for regression profiles. They do not include errors associated with the parameterization of the reflected thermal and reflected solar radiation.

During the development of the AIRS-RTA, the RMS errors were computed for a large independent set of profiles. The resulting RMS errors were generally slightly larger between spectral lines, and slightly smaller on top of lines. Since that time, the transmittance regressions have been improved significantly, and the latest model needs to be re-tested against an independent set of profiles. The regression profiles represent a

wide range of possible conditions, with a number of extreme cases. The RMS errors with an independent set of profiles are not expected to be much larger than what is shown in graphs presented here. It is important to recognize, however, that the AIRS –RTA does have a statistical component that comes from the selection of the regression profiles.

4.2.2.4 Regression Profiles

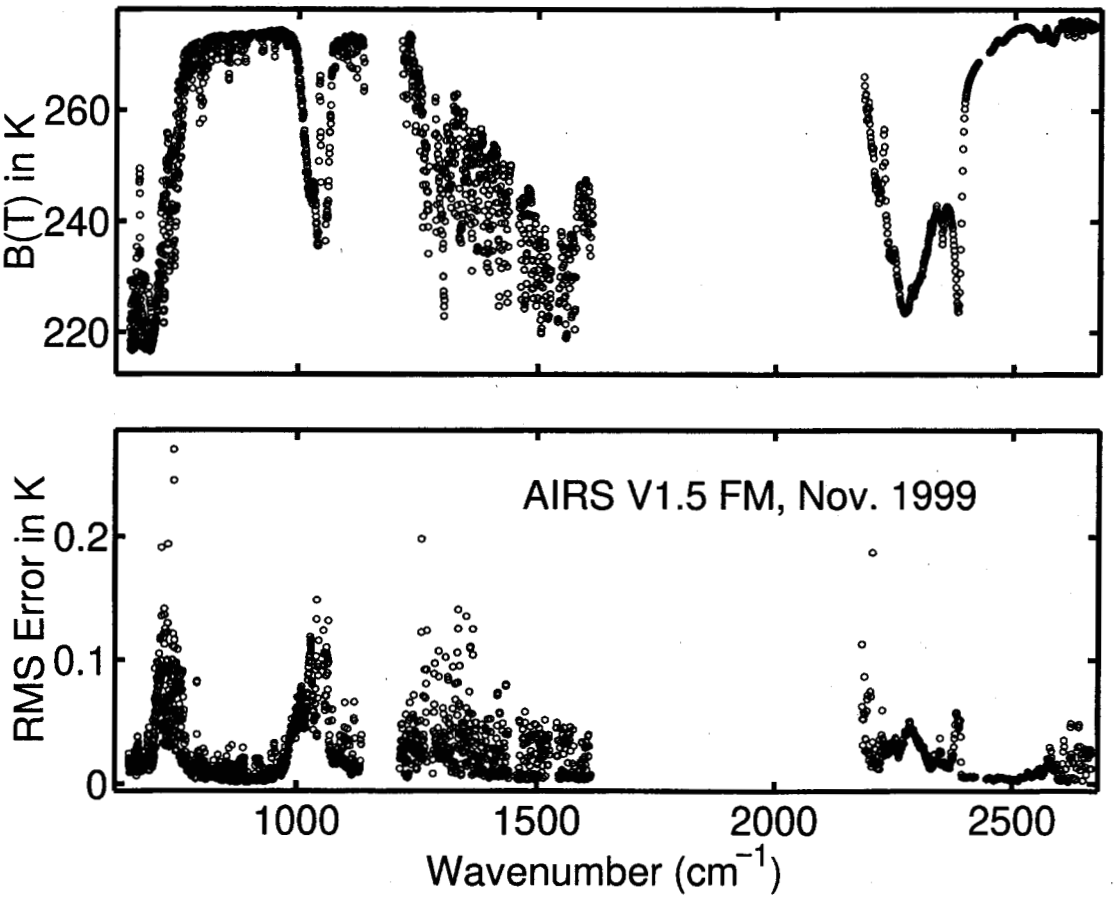

FIG 4.2.4: RMS FITTING ERRORS OF THE AIRS-RTA MODEL.

One other necessary pre-processing step is the selection of a set of profiles for calculation of the layer-to-space transmittances. The transmittances for these profiles become the regression data for the fast transmittance coefficients. These profiles should span the range of atmospheric variation, but, on the whole, should be weighted towards the more typical cases. The range of variation provides the regression with data points covering the range of possible atmospheric behavior, while the weighting of the mix of profiles towards more typical cases produces a transmittance model that works best on more statistically common profiles.

The process of calculating and convolving monochromatic layer-to-space transmittances is generally computationally intensive, thus imposing a practical limit on the number of profiles one can calculate for use in the regression. As discussed earlier, 48 regression profiles (at 6 viewing angles each) are sufficient to cover most of the profile behavior. This number is a compromise between the available time and computing resources and the need to cover a wide range of profile behavior in the regression. Choosing too few profiles leads to accuracy problems for profiles outside the range of behaviors considered. Choosing more profiles than necessary does not hurt the fast model, but does consume extra time and computer resources.

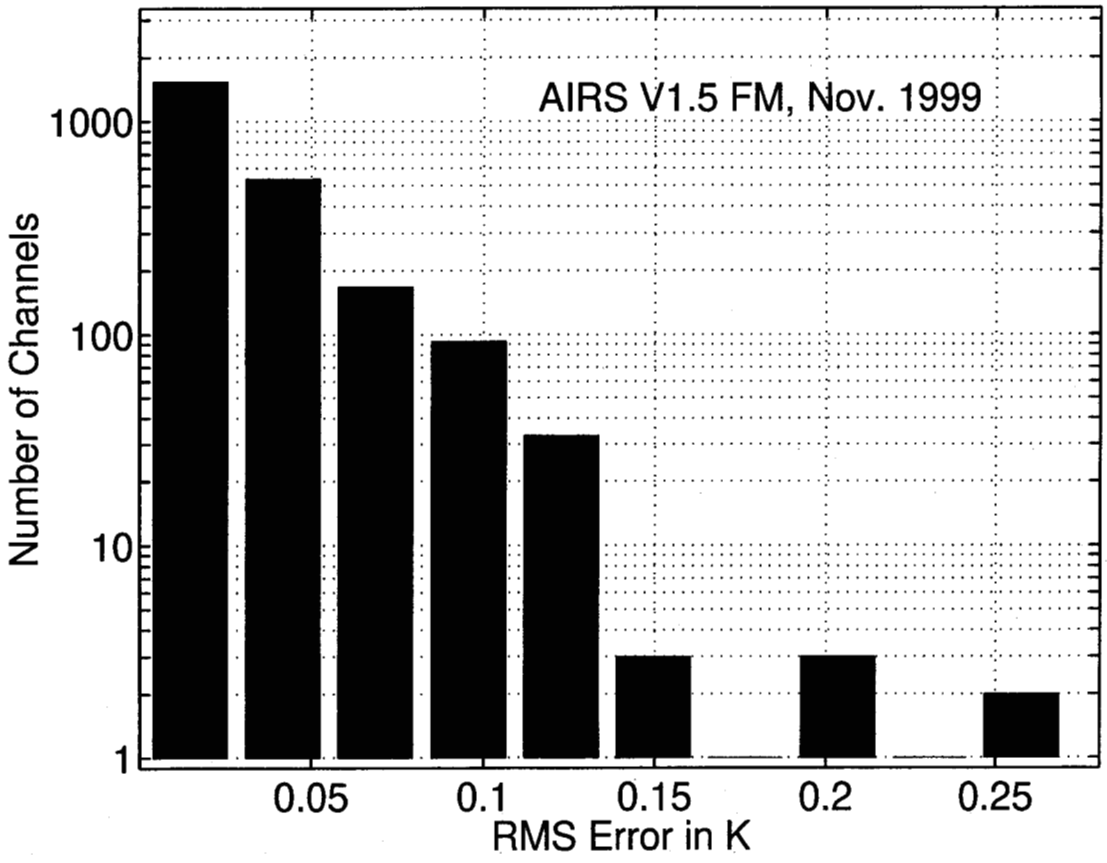

FIG 4.2.5: HISTOGRAM OF THE AIRS-RTA MODEL FITTING ERRORS FOR ALL CHANNELS.

Each profile should cover the necessary pressure (altitude) range with data for temperature as well as absorber amount for each of the gases allowed to vary. The fixed gases include all whose spatial and temporal concentration variations have a negligible impact on the observed radiances. As previously mentioned, the variable gases are H_2O, O_3, CO, CH_4, and CO_2. All other gases are included in the 'fixed gas' category. CO_2 is

handled differently than the other variable gases, and only two CO_2 absorber amount profiles are used: a standard amount profile and a perturbed amount profile. The standard amount CO_2 profile is treated as a fixed gas. A very simple and accurate parameterization is used to model the difference in transmittance between the standard CO_2 profile transmittances and the perturbed CO_2 profile transmittances.

For those satellite viewing angles relevant to the AIRS instrument (0 to 49 degrees), the effects of viewing angle can be approximated fairly well by multiplying the nadir optical depth by the secant of the local path angle. This approximation neglects the minor refractive effect at large angles. Due to the curvature of the Earth, the local path angle is in general not the same as the satellite viewing angle, but is related to it by a fairly simple equation. Local atmospheric path angles of 0, 32, 45, 53, 60, and 63 degrees are used in the regression profiles to cover the 0-49 degree satellite view angle range. An additional six angles between 69-84 degrees are used for the shortwave channels where transmittances at large angles are need to model the reflected solar radiance.

4.2.3 Spectroscopy

Our ultimate goal is to produce an AIRS-RTA that does not introduce significant errors in AIRS computed radiances. In the past, this has not been possible given the state-of-the-art in atmospheric spectroscopy. However, advances in laboratory measurements of line parameters and advances in phenomenological spectral lineshape models make an accurate AIRS-RTA a real possibility. This is especially important for water vapor. Radiosonde humidity errors, coupled with errors due to time and space co-location differences between radiosonde reports and AIRS observations, make tuning of the AIRS H_2O radiances quite suspect. Consequently, the forward model is of fundamental importance for AIRS data products.

During the development of the AIRS-RTA it has been clear that uncertainties in the CO_2 and water vapor lineshapes were easily large enough to impact AIRS retrievals. Consequently, we have been actively making (or analyzing) new laboratory measurements of these gases under conditions appropriate for AIRS. We have recently developed a new lineshape model for CO_2 that has significantly improved our ability to

compute AIRS radiances in the important CO_2 sounding channels (see later discussion). At present, we are analyzing new long-path (0.5 km) data of water vapor, taken at the Rutherford Appleton Laboratory (under AIRS sponsorship), in order to improve the water vapor continuum in the 1250 – 1350 cm-1 region important for sounding of tropospheric water vapor. We are also re-examining the water vapor continuum in the 10-12 um window with these data, where we suspect that the continuum is too strong. Work is also continuing on development of a near-wing water vapor lineshape that has been partially reported by Tobin et al. [1996a. 1996b].

In parallel with the laboratory spectroscopy, we have continued to compare the spectroscopy used in the AIRS-RTA with observed radiances, generally taken by a high resolution interferometer flying on NASA's ER-2 (HIS, NAST-I). Comparisons of this sort are highly dependent on good in-situ radiosonde data, which is often difficult to obtain. Nevertheless, comparisons between a growing number of these so-called validated radiance data sets indicates that our improved CO_2 spectroscopy is reducing the errors between observed and computed radiances. We have seen some marginal improvements in regions of strong water emission [Strow, 1998a], but these observations will always to difficult because of the relatively large systematic errors in the radiosonde humidity measurements in the mid- to upper-troposphere.

4.2.3.1 Spectroscopic Line Parameter Errors

Due to the dominance of either CO_2 or H_2O absorption in the majority of AIRS channels, the most important spectroscopy errors are associated with errors in the line parameters and line shapes of these two gases. The line parameters most likely to introduce spectroscopy errors into the fast forward model for AIRS are the line strengths, line widths, and the temperature dependence of the line widths. However, errors in spectral lineshapes and continuum absorption probably are generally more troublesome than line parameter errors.

Currently, the HITRAN98 [Rothman et al., 1998] database is used for most atmospheric line parameters, supplemented by more recent water linewidths measured by Toth [private communication]. The AIRS-RTA will be regularly updated with the latest

available line parameters using databases such as HITRAN2000 and GEISA [Husson et al., 1992]. Because there are so many bands and molecules that contribute to the observed radiances, the accuracy of the existing line parameters is difficult to judge in detail. Fortunately for AIRS, most of the important lines of both CO_2 and H_2O have been measured in the laboratory.

In general the CO_2 line parameters are better known than for H_2O. The line strengths for the stronger CO_2 lines have an estimated accuracy of ~2%, while the H_2O line strengths may only be good to 5%, or worse, for weak lines. The estimated uncertainties in the linewidths are 5% for CO_2 and 5-10% for H_2O. The combined effects of these errors on the AIRS computed radiances are difficult to ascertain, but we expect them to be on the order of 0.2 – 0.3K once recent laboratory results are incorporated into our radiative transfer models. These errors will also be highly wavenumber dependent. There may be isolated regions with larger errors, although these are slowly disappearing as the laboratory spectroscopy improves.

4.2.3.2 Molecular Line Shape Effects

Errors in the spectral lineshapes of CO_2 and H_2O are much more problematic than line parameter errors. Because of the large optical depths of CO_2 and H_2O in the atmosphere, their spectral line wings can be important, especially for remote sensing of temperature and humidity. For example, AIRS channels with the sharpest weighting functions are located in between lines or in the line wings where knowledge of the spectral line shape is most important. Moreover, accurate measurements of the line wing absorption are exceedingly difficult due to problems simulating atmospheric optical depths in a laboratory cell, especially for H_2O. It is also tedious and expensive to make these large optical depth measurements at the low temperatures found in the upper troposphere.

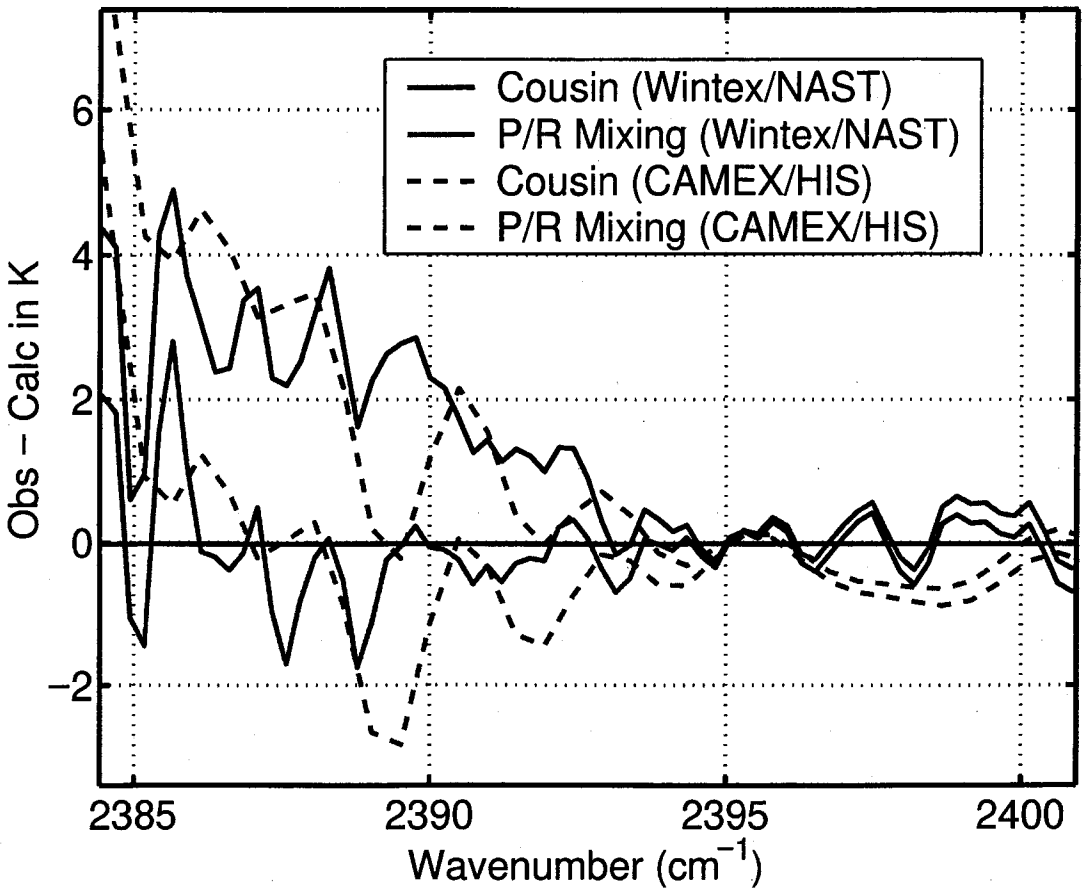

FIG. 4.2.6. COMPARISON OF NAST-I COMPUTED AND OBSERVED BRIGHTNESS TEMPERATURES DURING THE WINTEX CAMPAIGN IN THE 4.3 μM SPECTRAL REGION WHERE MANY TEMPERATURE SOUNDING CHANNELS ARE LOCATED

As discussed earlier, we are actively working to improve both the CO_2 and water vapor lineshapes for incorporation into the AIRS-RTA. The CO_2 work is essentially finished and is illustrated in Figures 4.2.6 and 4.2.7, showing the improvements between observed and computed NAST-I and HIS radiances taken during several campaigns. These improvements are based on a phenomenological model of P/R branch line mixing that is presently not available in any other line-by-line code. The difficulty of building this more advanced lineshape into an existing line-by-line code is one of the reasons why we had to develop our own line-by-line code (UMBC-LBL). Because line-by-line (and especially P/R branch line mixing) calculations are very slow, we developed a new pseudo line-by-line algorithm called the kCompressed Atmospheric Radiative Transfer

Algorithm (kCARTA) to allow the fast computation of almost monochromatic transmittances and (see below).

Recent laboratory work has improved our knowledge of the H_2O line shape within the strong part of the H_2O infrared band [Tobin et al. 1996a, 1996b], a region important for the determination of mid- to upper-tropospheric H_2O. In addition, recent measurements with the Atmospheric Emitted Radiance Interferometer (AERI) at the Department of Energy's Atmospheric Radiation Measurement program Cloud And Radiation Testbed site in Oklahoma should lead to an improved H_2O continuum in the AIRS window channels near 10 μm. This work is in progress.

4.2.4 Line-by-Line Calculations

The monochromatic layer-to-space transmittances used to determine the parameters of the AIRS-RTA model are indirectly generated using our custom line-by-line code (UMBC-LBL). We will continue to incorporate spectroscopic advances into UMBC-LBL and validate these using data acquired in the field campaigns discussed in the AIRS Validation Plan and outlined briefly in Section 8.6

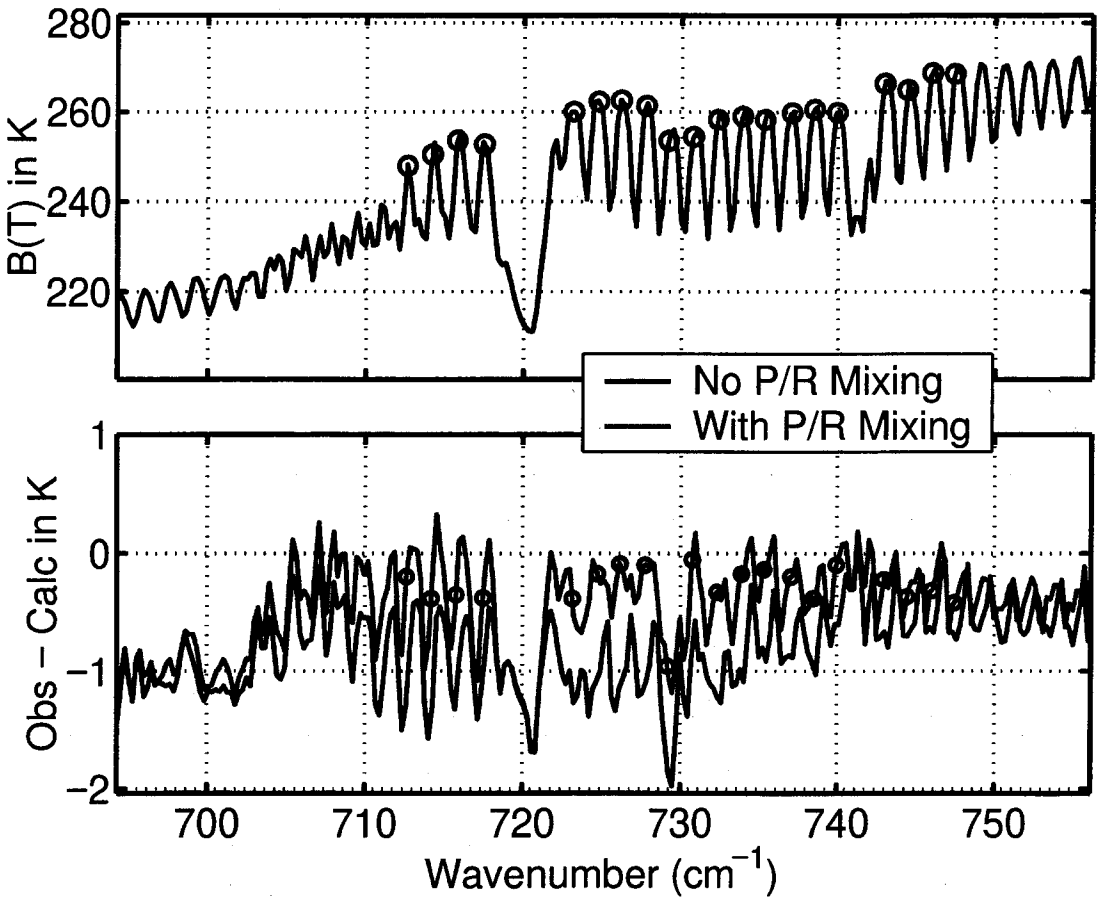

FIG. 4.2.7. COMPARISON OF NAST-I COMPUTED AND OBSERVED BRIGHTNESS TEMPERATURES DURING THE WINTEX CAMPAIGN IN THE 15 μM SPECTRAL REGION. THE CIRCLES DENOTE SPECTRAL REGIONS WHERE THE RADIOSONDE DATA CAN BE USED FOR COMPARISON TO OBSERVED RADIANCES, BASICALLY IN-BETWEEN SPECTRAL LINES THAT HAVE WEIGHTING FUNCTION PEAKING WELL BELOW THE ER-2 ALTITUDE.

Currently, 48 profiles are used in the regressions for the fast transmittance parameters. However, 48 line-by-line calculations for each of the 100 AIRS pressure layers are not performed directly with UMBC-LBL. Instead, UMBC-LBL is used to compute a very large look-up table of monochromatic layer optical depths for a set of 11 reference atmospheric profiles. Such a look-up table is similar to the approach of Scott and Chedin [1981]. Layer optical depths scale linearly with gas amount since the look-up table is monochromatic. In addition, the layer optical depths vary quite slowly and smoothly with temperature, allowing accurate interpolations in temperature. Note that any change in the physics of the line-by-line code or line parameter database requires a recalculation of the affected portion of the look-up table.

Each file in the look-up table covers a 25 cm^{-1} interval with 10,000 points (0.0025 cm^{-1} spacing) for 100 pressure layers (0.009492 to 1085 mb). The pressure layer structure, described in more detail in the following sub-section, was chosen to produce errors < 0.2 K in observed brightness temperatures for AIRS. For each infrared active gas and 25 cm^{-1} region from 605 cm^{-1} to 2830 cm^{-1}, 11 tables are computed differing only by the temperature profile. The 11 profiles are the U.S. Standard profile, and 10 profiles offset from it in ±10K increments. On average, 7 gases must be included per 25 cm^{-1} region. The continua due to gases such as N_2 and O_2 are also included in these tables. Optical depths are computed using a 0.0005 cm^{-1} grid and then averaged to the database grid spacing of 0.0025 cm^{-1}. Consequently, the highest altitude optical depths are not truly monochromatic, but exhibit good integrated optical depths. The relatively large width of the AIRS Spectral Response Function (SRF) results in negligible errors due to this averaging.

This large look-up table has been compressed and incorporated into our k-Compressed Radiative Transfer Algorithm (kCARTA) pseudo line-by-line code [Strow et al. 1998b]. The approximately 50 times compression achieved in kCARTA is lossy, but the accuracy of the transmittances remains very high. kCARTA bridges the gap between slow but accurate line-by-line codes, and fast but special purpose fast transmittance codes. kCARTA is used to calculate the 48 profile transmittances we use as regression data for the AIRS fast transmittance model. The computation time for these transmittances is not a significant fraction of the time involved in creation of a new fast model. However, the transmittance data files are very large, and the convolution of these monochromatic transmittances with the AIRS SRFs is a major time consuming process.

kCARTA will also serve as the AIRS Reference line-by-line algorithm for validation of the AIRS-RTA and general purpose analysis of AIRS accuracy. For example, kCARTA will be used for the initial analysis of AIRS observed radiances before the instrument is thermally stable.

4.2.5 Spectral Response Function Measurements and Modeling

Inaccuracies in the AIRS spectral response function directly impact the accuracy of the AIRS-RTA, and consequently the accuracy of the AIRS retrieved products. The AIRS SRFs are not Level 1 products, so it is appropriate to discuss the determination of the SRF functions in this document. Complete knowledge of the AIRS SRFs derived solely from ground calibration is not possible for two reasons; (1) small shifts in the alignment of the AIRS spectrometer/focal plane during launch could shift the centroids of the AIRS SRFs, and (2) the spectral location of fringes produced by the AIRS entrance aperture filters may be dependent on the thermal environment of AIRS in orbit. We expect both of these effects to be relatively small, but our requirements on SRF knowledge are quite stringent.

For example, we need to know the SRF centroids and widths to 1% or better. Following vibration testing of the AIRS instrument, the SRF centroids appeared to have shifted by more than 1%. AIRS may need to operate at two different temperatures during its design lifetime. Since the channel centroids and the fringe positions shift at different rates with temperature, new SRFs will be required for each operating temperature of AIRS. (AIRS is expected to operate at its initial in-orbit temperature for at least 3 years.)

It is likely that the effects of the channel spectra on the SRFs measured during ground calibration can be sufficiently characterized. This will allow us to determine the AIRS SRFs as if the channeling did not exist. We have convincing evidence that these "pure" SRFs vary in a very smooth fashion across each array and that the SRF shape can be adequately characterized using an empirical model function. In addition, using ground calibration data we can fully characterize the variation in the SRF centroids (and widths) with temperature.

Once in orbit, a sub-set of channel centroids can be accurately measured using upwelling radiances. This absolute frequency calibration will then be transferred to all other channels using the grating model derived from ground calibration data. The positions of the fringes relative to the actual channel centroids can also be determined in-orbit as follows. The fringes, which have a contrast of approximately 8%, affect the

radiometric gain of the AIRS detectors. However, the fringe positions are also dependent on temperature, so by varying the temperature of AIRS (during initial deployment) we can measure how the radiometric gain changes with temperature and wavenumber. From this information we reconstruct the fringe positions for each channel. This process also depends, to some extent, on the filter transmittance. Since the transmittances of the flight instrument filters were not measured at high spectral resolution, we must rely on transmittance measurements of filters manufactured at the same time as the flight filters.

Clearly, the determination of the AIRS SRFs involves a complicated series of events, some of which cannot be performed until after launch. A detailed analysis of the SRF uncertainties is premature since ground calibration only ceased in November 1999. The software to produce the AIRS-RTA has been developed to allow the relatively quick production of up-dated fast transmittance parameters once the SRFs are known in order to minimize delays in the start-up of operational retrievals.

4.2.6 AIRS-RTA Error Analysis

The following table contains preliminary estimates of the errors in the AIRS-RTA in units of brightness temperature. They are separated into radiative transfer/spectroscopy errors and SRF knowledge errors. In many cases these errors will be correlated, sometimes of opposite sign. Consequently it is very difficult to properly combine the errors in Table 4.2.1 into a single AIRS-RTA error budget. In addition, many of these errors are highly channel dependent.

The spectacular redundancy in the AIRS channels will provide many opportunities to separate the various contributions to the total RTA error budget. For example, many spectroscopy errors will be highly correlated. Moreover, these errors will correlate very poorly with errors due to inaccurate SRFs. Although some SRF errors will be difficult to completely characterize, we will know which channels are susceptible to these errors, which will help us isolate them from other errors. Fast model parameterization errors will be continuously checked using kCARTA and in-orbit data will most likely help highlight any problems with our choice of regression profiles.

Radiative Errors	Brightness Temperature Error (K)	Comments
Fast Transmittance Model	< 0.02K – 0.2K	Very channel dependent
Spectroscopy	0.2-0.4K	Larger errors where H2O continuum dominates
Reflected Thermal	0.15K	Needs improved parameterization
Solar	< 0.1K	Errors coupled with retrieval algorithm
Layering	Max 0.05K	Most channel have much lower errors
Polychromatic Approximation	0.05K	
Aerosols	?	Shortwave only
SRF Errors		
Centroids	0.2K	Somewhat channel dependent
Widths	0.2K	Analysis not complete
Channeling	0 – 0.3K	VERY channel dependent, assumes 0.1 cm-1 knowledge of fringe phase
Grating Model	0.1K?	Analysis incomplete on in-orbit absolute frequency calibration
Wings	0.1K	Analysis incomplete, channel dependent

TABLE 4.2.1 AIRS-RTA ERROR ESTIMATES

5 MATHEMATICAL DESCRIPTION OF THE CORE RETRIEVAL ALGORITHM

The AIRS Team Core Algorithm has two major product goals:

- a rapid determination of atmospheric state using regression methods
- a more accurate physically based retrieval of all geophysical parameters

These are maintained to provide the flexibility for operational data processing in a timely and computationally efficient manner in support of numerical weather prediction, as well as to provide high quality data products for Earth Science Enterprise research.

In this section both the underlying physics and the algorithms used to retrieve geophysical parameters will be described. Many different types of retrieval methodologies can be applied to this problem with advantages for each type. In general we can classify the approaches into two: 1) pre-computed Empirical Orthogonal Function (EOF) or regression methods and 2) physically-based techniques which match measured and calculated radiances and iterate until the match is within the expected signal-to-noise. Approach 1 is the fastest methodology because all the radiative transfer calculations are done off-line. The first approach is used to produce a rapid and accurate estimate of the geophysical parameters which can be refined by a rapid physical retrieval step. To produce the final product, a more sophisticated physical retrieval, which includes the use of a scene dependent noise covariance matrix, allows for further refinement of the products with error estimates on a case-by-case basis.

There are also two approaches to the infrared cloud-clearing problem: 1) account for the effects of clouds in the observed radiances and 2) eliminate the effects of clouds from the observed radiances. The method chosen for the AIRS Team algorithm is approach 2 which has had a long and successful application to current and previous generations of temperature sounder measurements. (Approach 1 will be examined as a research product and is not described in this document.)

The cloud-clearing methodology assumes very little about the radiative properties of the clouds. The only assumption is that for a given channel, a given cloud formation behaves the same in all fields of view. To the extent that a cloud formation behaves

differently in different fields of view, it is in reality more than a single cloud formation. The cloud clearing methodology can handle many cloud formations in principle, and has been tested for two cloud formations. Should the assumption of cloud homogeneity (between fields of view) for a given number of cloud formations break down, the scene will appear to contain multiple cloud formations and satisfactory solution will not be found and the profile will be rejected.

The final product algorithm does not attempt to solve for cloud properties simultaneously with the temperature and moisture profile because errors in the cloud properties (radiative properties of clouds can behave in a very complex way) will propagate into errors in the other retrieved quantities. We first obtain clear column radiances in a way that does not require knowledge of the detailed radiative properties of the clouds, then obtain solutions for other geophysical parameters, and then retrieve cloud properties.

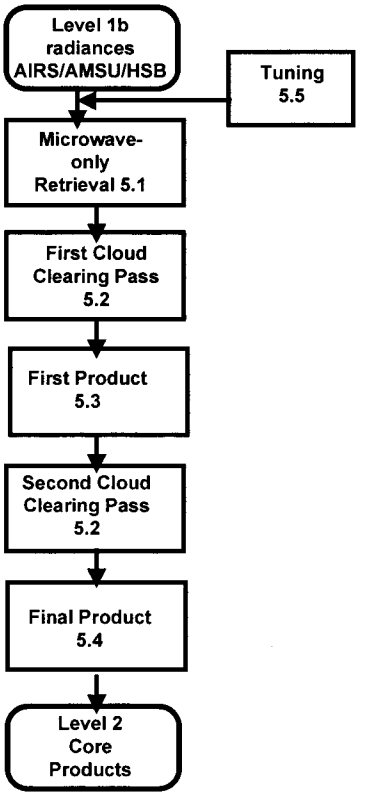

FIGURE 5.1.1 SIMPLIFIED ALGORITHM FLOW CHART

Overview

The approach the AIRS team has taken to meet the very stringent temperature accuracy constraint of 1K RMS Tropospheric error in 1 km increments is to provide multiple retrieval strategies, designated as products. A simplified chart is presented in figure 5.1 that describes the basic flow of the AIRS Team Algorithm design.

The main objective of the microwave initial guess algorithm (section 5.1) is to characterize the atmospheric column in terms of precipitation and cloud liquid water which are used in the cloud-clearing process throughout the core algorithm retrieval.

The clear sky or cloud-cleared radiance spectrum is derived from a composite cloud-clearing algorithm before retrievals in either the first or final product are attempted

The first product algorithm (section 5.3) has two objectives: (1) delivers the initial guess using in the final product algorithm and (2) is computationally expedient. Optionally, this result can be derived sufficiently quickly to be used in NOAA operational weather forecasting.

The final product algorithm (section 5.4) delivers all the AIRS/AMSU/HSB Core Products as defined in this document. The final product algorithm is a totally new state of the art algorithm developed for a high signal-to-noise instrument with many channels. The algorithm takes great care to describe all sources of channel noise (defined as the error in the difference between observed and computed brightness temperatures), especially errors due to cloud clearing. The algorithm then finds solutions which best match these radiances, given the noise covariance matrix, with no explicit consideration given to the estimated accuracy of the first guess, or the extent of deviation of the solution for the first guess. The algorithm has been shown to have only a very weak first guess dependence, and does not require considerations or coefficients which depend on location or season. In addition, the algorithm produces error estimates for all products, including clear column radiances, on a profile by profile basis. The final product algorithm is not dependent on the NOAA product, but can use either the microwave product, the NOAA product, or the NOAA regression guess, as its first guess. The final retrieval is only weakly dependent on the first guess used.

During the simulation testing (described in Section 8.4) and during the first phase of instrument checkout, the algorithm will be streamlined into its most robust and efficient form.

5.1 Microwave Initial Guess Algorithms

5.1.1 Precipitation Flags, Rate Retrieval, and AMSU Corrections

The precipitation algorithm produces (1) 2-bit flags for AMSU Channels 4, 5, 6, and 7, (2) estimates of corrections which should be applied to their brightness temperatures to compensate for precipitation, if present, (3) a precipitation-rate retrieval (mm/hr) which is currently valid primarily in mid-latitude regions where the algorithm was tuned with NEXRAD data, and (4) a flag indicating the quality of the precipitation retrieval. Inputs to the algorithm are fields of AMSU data for channels 1, 2, 4-12, and the data for all four HSB channels. Initially only the data at 183 ± 7 and 183 ± 1 GHz are actually being used. Figure 5.1.1 is a block diagram of the algorithm.

5.1.1.1 Precipitation Flags

The objective of the 2-bit flags for AMSU channels 4-7 is to alert users of this data to the possibility that retrievals based on these microwave channels might be impacted by precipitation. The four possible flag states are:

00 No precipitation perturbations detected
01 Small perturbations present (nominally less than 2K), which are approximately correctable
10 AMSU brightness perturbations for this channel may exceed 2K, so perturbation corrections are less reliable
11 It is unknown whether perturbations due to precipitation are present (e.g., altitude ≥ 2 km

Perturbation corrections are estimated for AMSU channels 4, 5, 6, and 7 for flag states 01, 10, and 11. In addition, for each AMSU beam position a precipitation-rate estimate (mm/hr) is provided when flag states 00, 01 or 10 exist for AMSU channel 4 (52.8 GHz). A quality flag for precipitation is also provided:

00 = no precipitation
01 = expected rms error relative to a NEXRAD equivalent observation ≤ 0.5 mm/hr
10 = rms error ≤ 1.5 dB
11 = else.

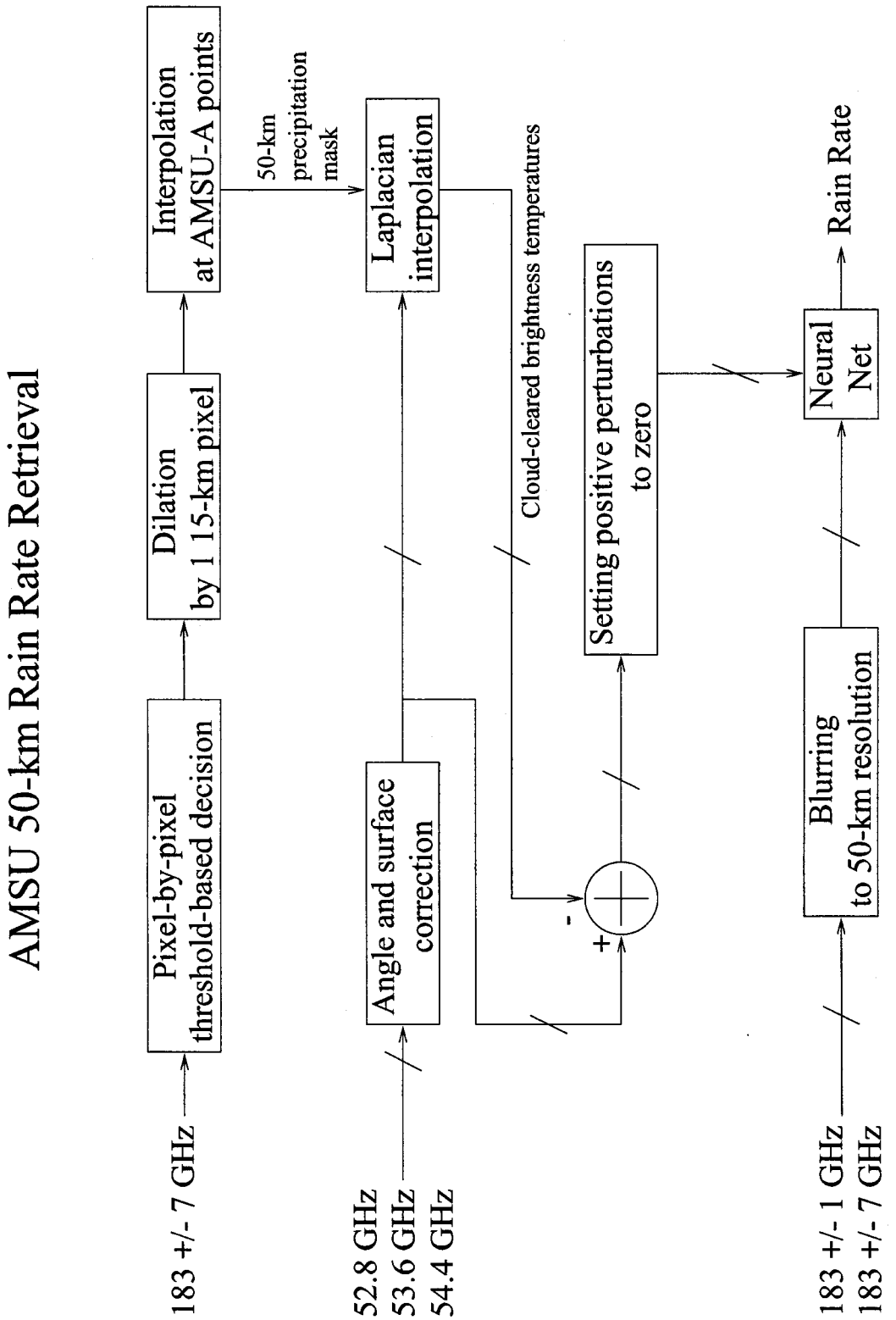

FIGURE 5.1.2 AMSU/HSB PRECIPITATION ALGORITHM

Users of AMSU data for temperature profile retrievals should use brightness temperatures flagged with 10 or 11 with caution, even if the suggested perturbation corrections are employed.

Generating precipitation flags from AMSU data involves nine major steps:

1) Flag HSB cells for which precipitation seems highly likely; i.e. flag cells for which 183 ± 7 GHz is colder than 260K. AMSU spots over ocean for which a simple liquid-water estimate exceeds a threshold are also flagged.
2) Dilate by one HSB cell width those regions flagged by 183 ± 7 GHz or 23/31 GHz. Each HSB flag is assigned to the nearest AMSU cell.
3) Effects of scan angle and surface variations are removed from AMSU channels 4-7 by a neural net estimating equivalent nadir brightness temperatures over land. For flagged regions touching the edge of the swath, linearly interpolate between the two non-flagged swath-edge AMSU corrected brightness temperatures bordering the flagged regions to estimate values for those 50-km pixels on the edge of the swath.
4) Perform Laplacian interpolation between corrected brightness temperatures bordering the dilated flagged regions in AMSU coordinates for AMSU channels 4, 5, 6, and 7.
5) For AMSU Channels 4-7 the interpolated brightness temperatures are subtracted from the corrected observed brightness temperatures to yield estimated perturbations due to precipitation. Positive perturbations are set to zero.
6) Precipitation flag 00 is assigned to all 50-km spots for those AMSU. Channels 4-7 for which neither the 183 ± 7 GHz flag nor the 23/31-GHz flag were set, or for which the deduced perturbations for the associated channel were less than 0.5K; the precipitation quality flag is also set to 00.
7) The flag 01 is assigned to all AMSU spots for those Channels 4-7 for which the perturbation on that channel lies between 0.5 and 2K.
8) The flag 10 is assigned to all AMSU spots for those Channels 4-7 for which the perturbation exceeds 2K.
9) The flag 11 is assigned to all AMSU spots for which a peak altitude in that area exceeds 2 km, or for which a precipitation determination could not be made.

Although the 183 ± 7 GHz channel is generally not sensitive to surface variations, mountain peaks and cold dry polar regions can produce false indications of precipitation. The 183 ± 7 GHz flag is also less reliable in humid tropical regions where it cannot penetrate to observe low-altitude precipitation. Over ocean these precipitating regions can be flagged instead by using liquid water retrievals based on AMSU Channels 1 and 2 at 23.8 and 31.4 GHz, respectively; a retrieval method for this is being derived and will be incorporated in the algorithm shortly. The 150-GHz channel peaks at still lower altitudes, so that in more humid mid-latitudes and tropical regions it could substitute or supplement the 183 ± 7 GHz channel.

It should be noted that 52.8-GHz radiances can suffer warm perturbations over ocean due to low altitude absorption by clouds or precipitation. Such warm perturbations can be flagged and corrected as are the cold perturbations, but warm perturbations have not yet been incorporated in the algorithm. Again, the 23.8/ 31.4 GHz combination will validate the locations of such excess absorption and perturbations.

5.1.1.2 AMSU Channel 4-7 Perturbations

These perturbations are the outputs computed in Step 5 of the flag generation procedure described above.

5.1.1.3 Precipitation Rate Retrievals

The precipitation rate is estimated using a neural network operating on cold perturbations in channels 4-7, and the blurred and aligned raw brightness temperatures of the four HSB channels (initially only the 183 ± 1 and 183 ± 7 GHz channels); the cosine of the scan angle is also incorporated. Staelin and Chen (1999) found excellent agreement between these precipitation rate retrievals and comparable retrievals using NEXRAD data. Agreement for four passes over two frontal systems and two hurricanes yielded agreement between 50-km AMSU and NEXRAD precipitation rates of 1.4 dB rms for those rates above 4 mm/hrr.

5.1.2 Profile Retrieval Algorithm

The microwave initial guess profile retrieval algorithm derives temperature, water vapor and non-precipitating cloud liquid water profiles from AMSU/HSB brightness temperatures. It is intended to provide the starting point for the AIRS cloud-clearing and retrieval. This is an iterative algorithm in which the profile increments are obtained by the minimum-variance method, using weighting functions computed for the current temperature and moisture profiles with the rapid transmittance algorithm described in Section 4.1. A block diagram is shown in Figure 5.1.2.

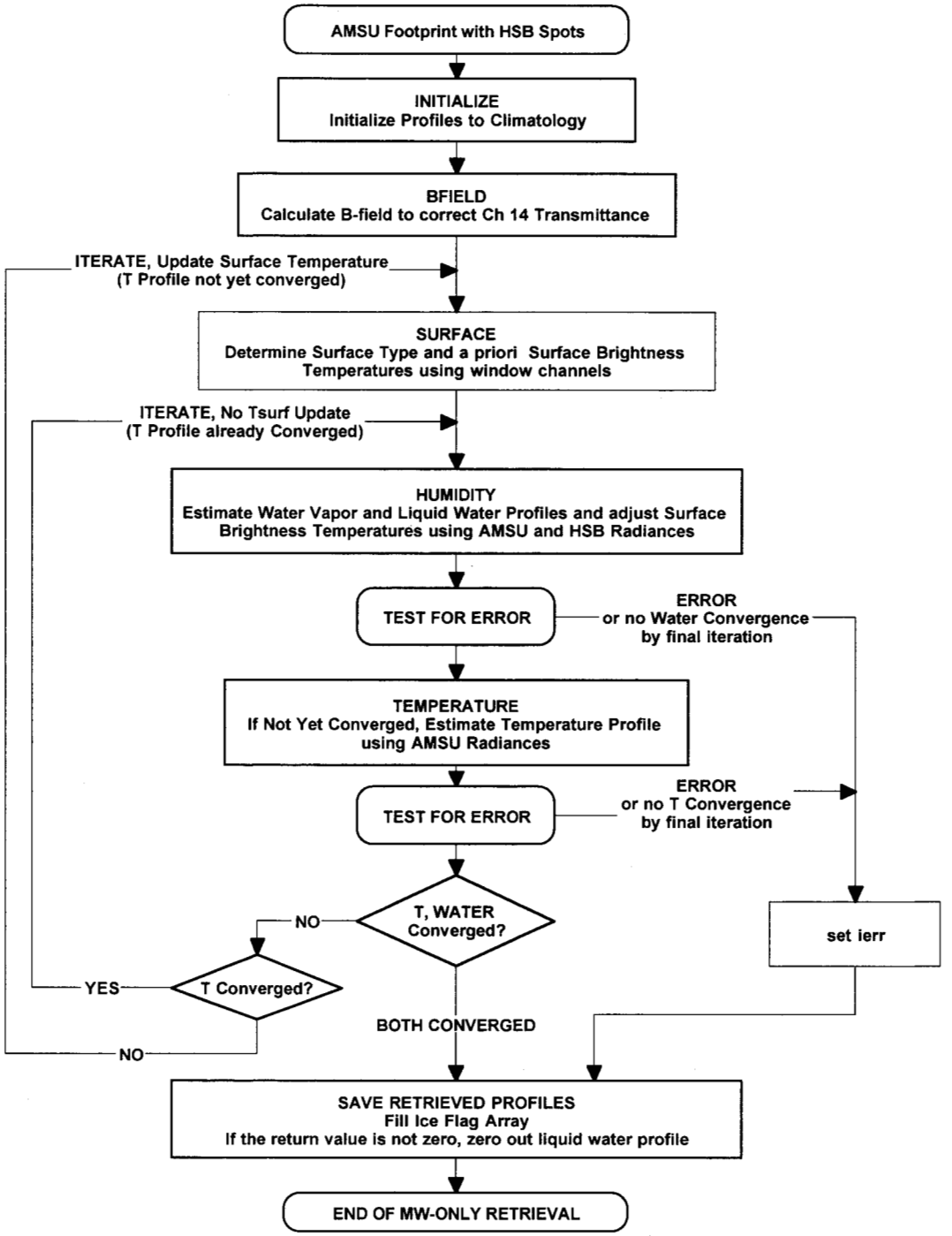

FIGURE 5.1.3 AMSU/HSB INITIAL-GUESS PROFILE RETRIEVAL

The retrieved profiles result from a process of iteration in which the minimum of a quadratic form

$$\left(\bar{X}-\bar{X}_o\right)^T \mathbf{S}_X^{-1}\left(\bar{X}-\bar{X}_o\right)+\left[\bar{\Theta}_{obs}-\bar{\Theta}\left(\bar{X}\right)\right]^T \mathbf{S}_{err}^{-1}\left[\bar{\Theta}_{obs}-\bar{\Theta}\left(\bar{X}\right)\right] \tag{5.1.1}$$

is approached asymptotically. In the above, $\bar{X}$ is the estimate of a vector of parameters defining the state of the atmosphere and the surface, $\bar{X}_o$ is its *a priori* value and $\mathbf{S}_X$ is its covariance matrix, $\bar{\Theta}_{obs}$ is a vector containing the measured brightness temperatures, $\mathbf{S}_{err}$ is their error covariance matrix, and $\bar{\Theta}\left(\bar{X}\right)$ is a brightness temperature vector computed from $\bar{X}$ by the radiative transfer model (see Section 4.1).

The input vector of measured brightness temperatures is accompanied by an input validity vector whose elements are either one or zero. This provides a way of handling missing or bad data when real measurements eventually are processed. Prior to the retrieval, the rain rate in the field of view will be estimated, and if the rain exceeds some threshold, the lower tropospheric channels will either be corrected for perturbation by rain, or excluded from use in the retrieval by setting their validity flags to zero.

Planck's equation for radiant intensity is a nonlinear function of temperature. For microwave frequencies, however, the physical temperatures encountered in the earth's atmosphere lie at the high-temperature asymptote of this function. Hence, as discussed by Janssen (1993), brightness temperature can be used as a surrogate for radiance in the equation of radiative transfer with an accuracy of a few hundredths of a kelvin. The only exception to this statement occurs with the cosmic background, which must be assigned an effective brightness temperature at frequency ν of

$$\Theta_{CB}=\frac{h\nu}{2k}\times\frac{e^{h\nu/kT_{CB}}+1}{e^{h\nu/kT_{CB}}-1} \tag{5.1.2}$$

instead of its actual temperature $T_{CB}=273$ K, in order to linearize Planck's function.

The equation of radiative transfer is written in the form

$$\Theta_{TOA} = \Theta_{direct} + \tau\left[\Theta_s + \Theta_{sky}\left(1 - \frac{\Theta_s}{T_s}\right)\right] \tag{5.1.3}$$

where Θ_{TOA} is the brightness temperature emitted from the top of the atmosphere, τ is the one-way transmittance of the atmosphere, Θ_{direct} is the component of brightness temperature emitted from the atmosphere on a direct path to space, Θ_s is the surface brightness temperature, Θ_{sky} is the sky brightness temperature (including the attenuated cosmic contribution) as it would be observed from the surface, and T_s is the physical surface temperature. Based on experience with NOAA-15 data, Θ_{sky} is currently computed for a path length (or opacity) equal to 1.15 times the direct path (1.10 for AMSU channels 4-14). This empirical adjustment accounts approximately for the effect of ocean surface non-specularity, and is consistent with the calculations of Guissard and Sobieski (1994). For higher-emissivity surfaces, the adjustment has a negligible effect.

5.1.2.1 Surface Brightness Model

The surface brightness temperature spectrum Θ_s is modeled by a four-parameter curve (Grody, 1988), added to an *a priori* surface brightness:

$$\Theta_s = \Theta_{so} + \frac{R_o T_o + R(\nu) T_\infty}{R_o + R(\nu)}, \tag{5.1.4}$$

where R_o and $R(\nu)$ are defined as

$$R_o = (\nu_o / 31.4\ \text{GHz})^s, \tag{5.1.5}$$

$$R(\nu) = (\nu / 31.4\ \text{GHz})^s. \tag{5.1.6}$$

T_o, T_∞, ν_o and s are parameters defining the curve, and Θ_{so} is a preliminary estimate of surface brightness temperature.

The surface classification rules are from Grody *et al.* (1999), and make use of discriminant functions which are linear combinations of AMSU channels 1, 2, 3, and 15. If sea ice is indicated by the classification algorithm, then its concentration fraction is

estimated from a linear operation on channels 1, 2, and 3. *A priori* emissivities for the ice and snow types have been estimated from NOAA-15 data; further work on these is planned. For land, $\Theta_{so} = 0.95\ T_s$ at all frequencies, and for seawater it is calculated by a second-order polynomial function of temperature with coefficients fitted to the emissivity of a flat surface viewed in the polarization of the AMSU and HSB radiometers. A separate set of these coefficients was pre-computed for each incidence angle and frequency. The model of Guillou *et al.* (1998) was used for seawater dielectric constant at 23.8 and 31.4 GHz, and the model of Lamkaouchi *et al.* (1997) at higher frequencies.

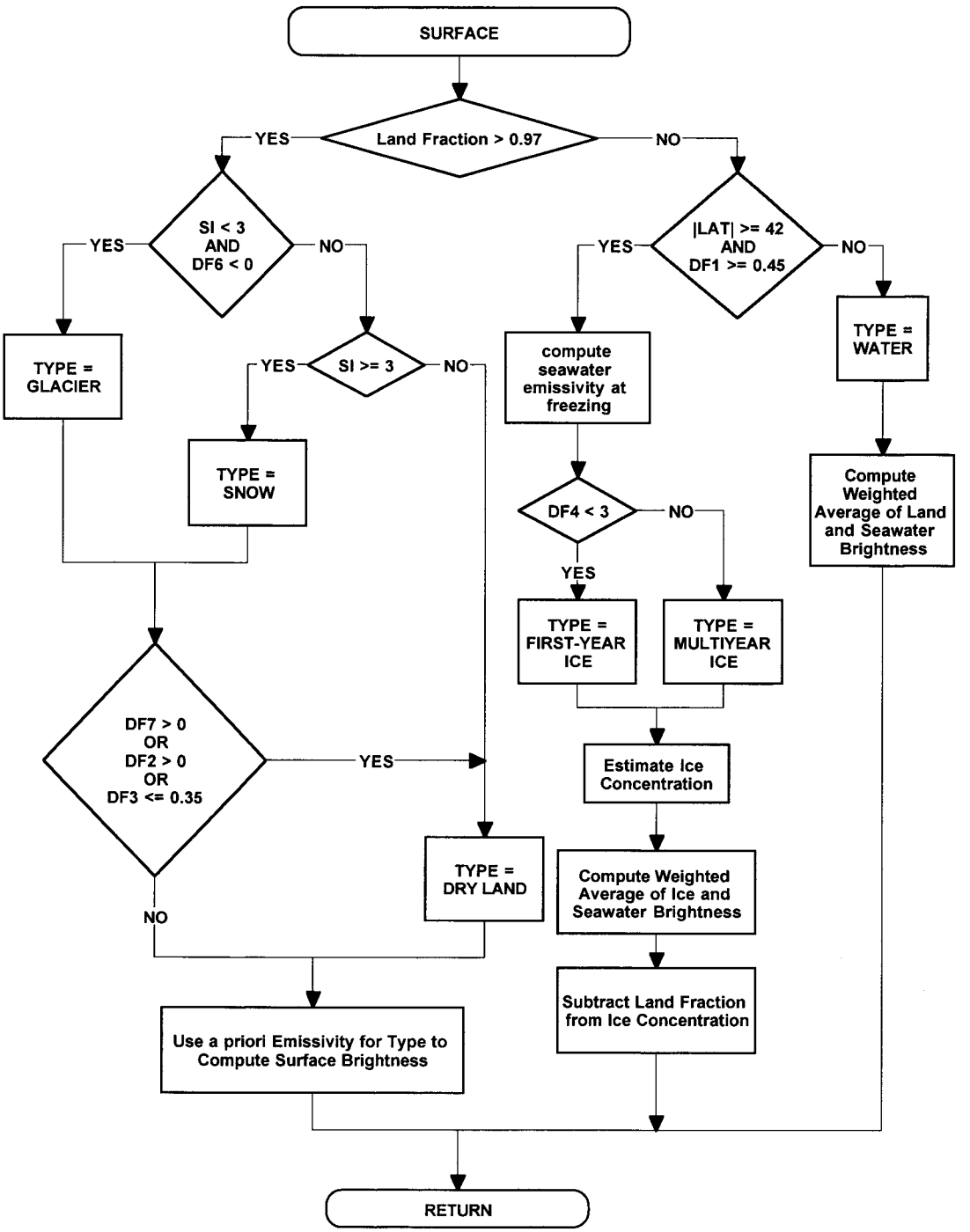

FIGURE 5.1.4 SURFACE CLASSIFICATION ALGORITHM

Thus the surface model takes a baseline Θ_{so} and adds or subtracts a smooth function of frequency, to correct for surface roughness, for errors in the dielectric constant model, for a mis-classification of the surface, etc. For example, it was found that (4) could

approximate a blackbody surface ($\Theta_s = T_s$) to within 0.5% at all AMSU and HSB frequencies, even when $\Theta_{so}(\nu)$ was computed for seawater, if s = 1.2 and R_0, T_0, and T_∞ were adjusted to appropriate values for a given temperature. The discussion in Grody (1988) suggests that a function such as (4) is capable of approximating the emissivity of a wide variety of surfaces.

The retrieval algorithm fixes s at the value 1.2 and treats R_0, T_0, and T_∞ as uncorrelated free parameters for which it solves, as described below. Mean values are set to

$$\begin{aligned} \overline{R}_0 &= 3.5 \\ \overline{T}_0 &= 0 \\ \overline{T}_\infty &= 0 \end{aligned} \qquad (5.1.7)$$

and variances are set to

$$\begin{aligned} S_{R_0} &= 2.25 \\ S_{T_0} &= 100 \quad (\text{Kelvin})^2 \\ S_{T_\infty} &= 100 \quad (\text{Kelvin})^2 \end{aligned} \qquad (5.1.8)$$

5.1.2.2 Atmospheric Moisture and Condensation Model

Measurements of brightness temperature at the HSB frequencies are a result of the vertical profile of atmospheric opacity relative to temperature and hence do not by themselves distinguish, at any given altitude, between opacity due to water vapor and opacity due to liquid water. However, the physics of water vapor condensation add some *a priori* information or constraints. Cloud coverage is parameterized as in the stratiform condensation model of Sundqvist *et al.* (1989), where a relative humidity threshold determines the onset of condensation. If the observing instrument had infinitesimal horizontal resolution, an appropriate threshold would be 100% relative humidity. Although the water vapor profile is saturated within the cloudy part of the field, it is assumed that the condensation process is not spatially resolved, hence the threshold is less than 100%. Currently, the threshold is $H_{cth} = 85\%$

The H profile stored by the algorithm serves to define both the vapor and cloud liquid water density profiles, as illustrated in Figure 5.1.4.

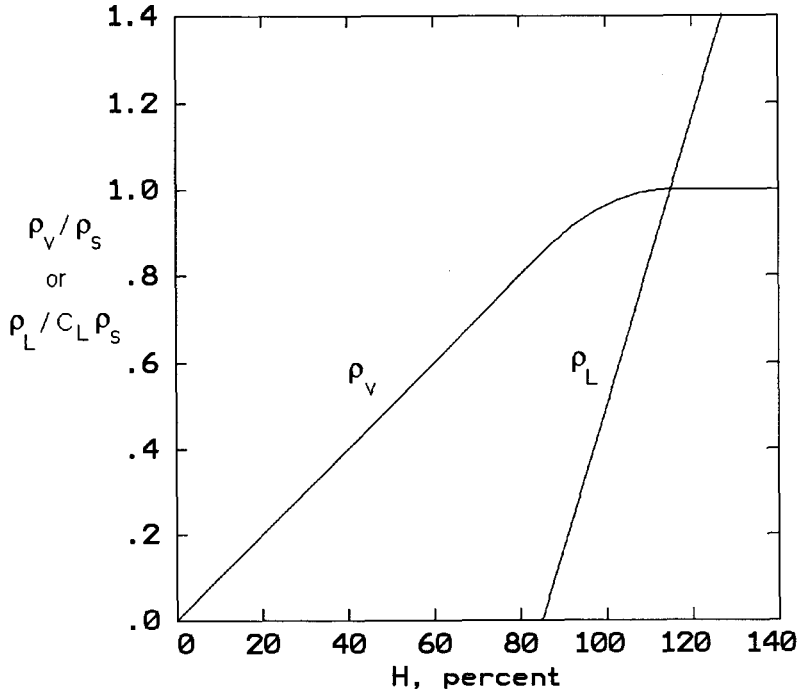

FIGURE 5.1.5 WATER VAPOR (ρ_v) AND CLOUD LIQUID (ρ_L) DENSITIES AS FUNCTIONS OF H

The average vapor density in the field of view is

$$\rho_V = \begin{cases} \rho_s[H/100] & \text{if } H \le H_{cth} \\ \rho_s\left[(100 - H_{cth})(2b - b^2) + H_{cth}\right]/100 & \text{if } H_{cth} < H \le (200 - H_{cth}) \\ \rho_s & \text{if } H \ge (200 - H_{cth}) \end{cases} \quad (5.1.9)$$

and the liquid water density averaged over the field of view is assumed to be given by

$$\rho_L = \begin{cases} 0 & \text{if } H \le H_{cth} \\ C_L \rho_S b & \text{if } H > H_{cth} \end{cases} \quad (5.1.10)$$

In the above, ρ_s is the saturation value of vapor density,

$$b = \frac{H - H_{cth}}{2(100 - H_{cth})}, \quad (5.1.11)$$

and C_L is a preset constant, currently 0.02. Note that when $H \leq H_{cth}$, H is equal to relative humidity, but H can take values > 100% in cloudy regions.

The saturation vapor density is computed from the temperature profile. Saturation vapor density is calculated with respect to liquid water (by extrapolation) even when the temperature is below 273 K, because ice clouds are not considered within the context of this algorithm. (Absorption from ice is much less than from liquid water, and scattering is not included in the radiative transfer formulation.) This model therefore allows supercooled liquid water and water vapor greater than the saturation value over ice.

5.1.2.3 Estimation of Surface Brightness and Atmospheric Moisture

This part of the algorithm is based on retrieval methods described by Wilheit (1990), Kuo *et al.* (1994), and Wilheit and Hutchison (1997). It uses the four channels of HSB and channels 1, 2, 3 and 15 of AMSU. The HSB measurements are weighted averages over 3x3 spatial arrays which approximate the AMSU field of view. The H profile and the three surface brightness parameters R_o, T_o, and T_∞ can be concatenated into a vector $\bar{Y}$. For small departures of $\bar{Y}$ from an existing estimate $\bar{Y}_{est_{n-1}}$, measured brightness temperature $\bar{\Theta}_{obs}$ is assumed to be related to the true $\bar{Y}$ profile by

$$\bar{\Theta}_{obs} = \bar{\Theta} + \mathbf{W_Y}\left[\bar{Y} - \bar{Y}_{est_{n-1}}\right] + e \tag{5.1.12}$$

where $\bar{\Theta}$ is a brightness temperature vector computed from the current values of temperature, moisture, and surface brightness, $(\mathbf{W_Y})_{ij} = \partial\Theta_i/\partial Y_j$ and e represents unknown measurement errors. It follows from (4) and the chain rule for differentiation that the matrix elements of $\mathbf{W_Y}$ corresponding to the surface parameters are equal to

$$\partial\Theta/\partial R_o = (\partial\Theta/\partial\Theta_s)\, R(\nu)\, (T_o - T_\infty)\, (R_o + R(\nu))^{-2} \tag{5.1.13a}$$

$$\partial\Theta/\partial T_o = (\partial\Theta/\partial\Theta_s)\, R_o\, (R_o + R(\nu))^{-1} \tag{5.1.13b}$$

$$\partial\Theta/\partial T_\infty = (\partial\Theta/\partial\Theta_s)\, R(\nu)\, (R_o + R(\nu))^{-1} \tag{5.1.13c}$$

where, from (5.1.3),

$$\partial\Theta/\partial\Theta_s = \tau\left(1-\Theta_{sky}/T_s\right). \tag{5.1.14}$$

The elements of $\mathbf{W_Y}$ corresponding to H values are

$$\frac{\partial\Theta}{\partial H} = G\bullet\left(\frac{\partial\kappa}{\partial\rho_v}\bullet\frac{\partial\rho_v}{\partial H}+\gamma\frac{\partial\rho_L}{\partial H}\right), \tag{5.1.15}$$

in which $G = \partial\Theta/\partial\kappa$ where κ represents the opacity of the layer, and $\gamma = \partial\kappa/\partial\rho_L$. G is equal to the integral over an atmospheric layer of the function G(h) for which an expression is given by Schaerer and Wilheit (1979). The rapid transmittance algorithm computes the coefficient γ in the small-droplet (Rayleigh) approximation. Hence, it is intended to be applied only to non-precipitating cloud situations. A quadratic model is used to compute the opacity of water vapor:

$$\kappa = \beta_1\rho_v + \beta_2\rho_v^2 + \text{other contributions;} \tag{5.1.16}$$

hence

$$\frac{\partial\kappa}{\partial\rho_v} = \beta_1 + 2\beta_2\rho_v + \ldots \tag{5.1.17}$$

where

$$\beta_1 = \beta\left(\rho_{v_{est}}, T_{est}\right) - \beta_2\rho_{v_{est}}, \tag{5.1.18}$$

$$\beta_2 = d\beta/d\rho_v \tag{5.1.19}$$

The coefficients β and $d\beta/d\rho_v$ are computed by the rapid transmittance algorithm using the temperature profile retrieval and the initial moisture profile. As a consequence of (5.1.9-11), $\partial\rho_v/\partial H$ and $\partial\rho_L/\partial H$ depend on H as follows:

$$\frac{\partial\rho_v}{\partial H} = \begin{cases} \rho_s/100 & \text{if } H \le H_{cth} \\ \rho_s(1-b)/100 & \text{if } H_{cth} < H \le (200 - H_{cth}) \\ 0 & \text{if } H \ge (200 - H_{cth}) \end{cases} \tag{5.1.20}$$

$$\frac{\partial \rho_L}{\partial H} = \begin{cases} 0 & \text{if } H \le H_{cth} \\ C_L \rho_S / 2(100 - H_{cth}) & \text{if } H > H_{cth} \end{cases} \tag{5.1.21}$$

The estimate of $\bar{Y}$ is obtained by Newtonian iteration (see Rodgers, 1976), except that Eyre's (1989) method of damping is used to avoid large relative humidity increments, because of the nonlinearity of the problem:

$$\bar{Y}_{est_n} = \bar{Y}_{est_{n-1}} - \delta \left[\bar{Y}_{est_{n-1}} - \bar{Y}_{est_o} \right] + \delta \, \mathbf{S_Y} \mathbf{W_Y^T} \bar{X}_Y \tag{5.1.22}$$

in which $\bar{Y}_{est_o}$ contains the *a priori* mean parameter values, $\mathbf{S_Y}$ is the *a priori* covariance matrix of $\bar{Y}$, superscript T indicates transpose, $\bar{X}_Y$ is the solution vector to

$$\left[\mathbf{W_Y} \delta \, \mathbf{S_Y} \, \mathbf{W_Y^T} + \mathbf{S_e} \right] \bar{X}_Y = \bar{\Theta}_{obs} - \bar{\Theta} + \mathbf{W_Y} \, \delta \left[\bar{Y}_{est_{n-1}} - \bar{Y}_{est_o} \right] \tag{5.1.23}$$

where $\mathbf{S_e}$ is the (assumed diagonal) covariance matrix of *e*, and

$$\delta = \begin{cases} 1.0 & \text{if } \left(\Theta_{i_{obs}} - \Theta_i \right) \le 10 \text{ K} \quad \text{for all channels} \quad i \\ 0.1 & \text{otherwise} \end{cases} \tag{5.1.24}$$

Here δ is a scalar rather than a matrix as in Eyre's paper. The parts of $\bar{Y}_{est_o}$ and $\mathbf{S_Y}$ corresponding to relative humidity were calculated from the TIGR profile ensemble (Chedin *et al*, 1985) while the surface parts are given by equations (5.1.7-8). For the moisture channels, the measurement error covariance $\mathbf{S_e}$ is the sum of contributions due to instrument noise plus a diagonal error of $(1.5 \text{ K})^2$ which approximately represents errors in Θ resulting from errors in the temperature profile retrieval. It is important to note that because convergence is determined from the brightness temperature residuals, which in turn are computed using the vapor and liquid column densities, the role of H in this algorithm is only to introduce the *a priori* statistics and constraints.

The estimated H profile is limited by 1 percent from below and from above by a value which converts to 1 g/m^3 liquid water density. This latter value is intended as an approximate upper limit for non-precipitating cloud densities, and hence it will tend to leave large brightness temperature residuals in situations of precipitation, and especially when scattering is occurring (if these are not excluded by use of the precipitation flag).

After update of $\bar{Y}$ by (5.1.22-23), the water vapor and liquid water profiles are computed

from (5.1.9-11), and surface brightness is computed for both window and sounding frequencies from (5.1.4), using the new estimate.

5.1.2.4 Estimation of the Temperature Profile

The atmospheric temperature vector is augmented by T_s, which is considered to be distinct from the air temperature near the surface. The measured Θ's used in the temperature profile retrieval are channels 4-14 of AMSU. Given an existing estimate $\bar{T}_{est_{n-1}}$, the new estimated profile is to be determined from a vector Θ_{obs} of observed brightness temperatures, which for small difference profiles $\bar{T} - \bar{T}_{est_{n-1}}$ is related to the true profile $\bar{T}$ by

$$\Theta_{obs} = \Theta + \mathbf{W_T} [\bar{T} - \bar{T}_{est_{n-1}}] + e \tag{5.1.25}$$

in which Θ is the brightness temperature vector that would theoretically be emitted from the atmospheric profile described by $\bar{T}_{est_{n-1}}$. The sensitivities of the measured Θ's to the elements of the temperature profile vector constitute the observation matrix $\mathbf{W_T}$. The elements of this matrix corresponding to the atmospheric part of the temperature vector are given by

$$\partial\Theta/\partial T = K + G\partial\kappa/\partial T \tag{5.1.26}$$

where K is equal to the temperature weighting function as defined by Schaerer and Wilheit (1979) integrated over the given atmospheric layer, $G = \partial\theta/\partial\kappa$, and $\partial\kappa/\partial T$ is computed by the rapid transmittance algorithm. The second term on the right side of (26) is a small correction to the temperature weighting function.

The elements of $\mathbf{W_T}$ corresponding to T_s are obtained by partial differentiation of Eq. (3):

$$\frac{\partial\Theta}{\partial T_s} = \frac{\tau\,\Theta_{sky}\,\Theta_s}{T_s^2} \tag{5.1.27}$$

The dependence on T_s is nonlinear here because Θ_s is considered to be a known input from the moisture algorithm. If the validity of a channel is zero, then the row of $\mathbf{W_T}$ corresponding to that channel is set to zeros. The dimensions of the matrix remain the same.

The covariance of the temperature vector was computed from the TIGR ensemble (Chedin *et al.*, 1985). The difference between T_s and the air temperature near the surface (T_{1013}) is assumed to have zero mean and standard deviation of 4 K. Thus, T_s has a larger variance, by 16 K^2, than T_{1013}, but its covariances with other levels are equal to those of T_{1013}.

Initially, the temperature profile, including surface temperature, is set to a climatological profile $\bar{T}_{est_o}$ which depends on latitude and season. The new, minimum-variance estimate of $\bar{T}$ is obtained by Newtonian iteration (Rodgers, 1976, eq. 101)

$$\bar{T}_{est_n} = \bar{T}_{est_o} + \mathbf{S_T W_T^T} \bar{X}_T, \tag{5.1.28}$$

where $\mathbf{S_T}$ is the temperature covariance matrix, and X_T is the solution vector to

$$\left[\mathbf{W_T S_T W_T^T} + \mathbf{S_e}\right]\bar{X}_T = \bar{\Theta}_{obs} - \bar{\Theta} + \mathbf{W_T}\left[\bar{T}_{est_{n-1}} - \bar{T}_{est_o}\right]. \tag{5.1.29}$$

The error covariance matrix $\mathbf{S_e}$ includes the effects of surface brightness uncertainty and instrument noise.

5.1.2.5 Iteration Procedure and Convergence Tests

After the temperature profile is updated using (28) and (29), the algorithm returns to the moisture and surface-brightness section for another iteration of (22) and (23), using weighting functions computed for the updated temperature and moisture profiles. Convergence is tested separately for the temperature channels and for the moisture/surface channels; iteration of either part of the algorithm is suspended when one

of the following conditions is met : (1) the computed brightness temperature vector $\bar{\Theta}$ meets the closure criterion

$$\sum_{i=1}^{N_B} \frac{\left[\Theta_{obs_i} - \Theta_i\right]^2}{\Delta T_i^2} \leq N_B, \qquad (5.1.30)$$

where ΔT_i is the instrument noise on channel i and N_B is the number of valid elements in $\bar{\Theta}_{obs}$; or (2) when successive computations of the left side of (30) change by less than 1% of the right side, for the temperature channels, or 2% for the moisture/surface channels; or (3) when the number of iterations exceeds a preset limit, currently 12 for the temperature channels and 16 for the moisture/surface channels. Typically, iteration of the temperature profile ceases after one or two iterations, but the moisture profile often requires six or more iterations.

If the mean square of brightness temperature residuals for the HSB channels is greater than a preset threshold value, then an ice scattering flag is set at all altitudes for which clouds are present and the temperature estimate is below 273 K. The scattering threshold is currently set at 64 (i.e., 8K rms per channel).

5.2 Cloud Clearing

5.2.1 Local Angle Adjustments of AIRS Observation

The cloud-clearing algorithm assumes that the observed AIRS footprints falling within the composite AMSU retrieval footprint differ only in the cloud amount. Other parameters, such as the viewing angle, are assumed constant over the 3 x 3 array of AIRS footprints being used. This means the 9 AIRS footprints at 3 different zenith angles (φ) must be adjusted to a common central zenith angle (φ_{cen}) before cloud clearing is attempted.

The coefficients of the correction are based on synthetic regression, a process in which regression coefficients are generated using radiances that are simulated for a range of cloud conditions and profiles that cover the expected atmospheric range. AIRS radiances are calculated for each of the 90 AIRS viewing angles and AMSU radiances are calculated for the AMSU footprint viewing angle. Noise is added, but care must be taken that it be treated properly. The radiances being calculated are an attempt to simulate the measurement that would have been observed if the viewing angle was different. Thus all other factors, including the noise, do not change with angle. What this means for the simulation is that the added noise is random over the set of profiles and for each channel, but is constant over the viewing angle. In other words, once the noise is determined for a channel and a profile, that same noise is used for all 90 AIRS viewing angles. It must only be constant over the 3 viewing angles that cover each AMSU footprint, but it is easier to keep it constant over all 90 spots.

Let prof be the profile index, fp be the footprint number, ν be channel frequency and φ be the zenith angle, respectively; the noisy radiance for a given profile, footprint, channel and local zenith angle is:

$$R(\text{prof},\text{fp},\nu,\varphi) = R_o(\text{prof},\text{fp},\nu,\varphi) + \varepsilon(\text{prof},\text{fp},\nu) \qquad (5.2.1)$$

where $R_o(\text{prof},\text{fp},\nu,\varphi)$ is the noise free radiance, and $\varepsilon(\text{prof},\text{fp},\nu)$ is the noise for the particular profile, spot, and channel. The consequence of not treating the noise

properly is to cause large errors in the predictants used to generate the coefficients, with a corresponding adverse effect on the resulting coefficients. Many angle adjustment procedures currently in use do not properly handle the instrumental noise.

In the following discussion, the term "weighting function" is used to denote the contribution function that describes the region of the atmosphere being viewed by a particular channel. The observed radiance for a particular channel changes with angle in two ways. One is that the weighting function peaks in a higher region of the atmosphere when the angle moves away from nadir. The other is that the weighting function becomes slightly narrower. This occurs because, to a first approximation, the majority contribution to the observed radiance for a particular channel arises within a confined slab of the atmosphere. When viewed at an angle, the slab is thinner in atmospheric height. For the small angles under consideration, the second effect is small. If the weighting function peak for a channel is raised slightly in the atmosphere, there is a linear combination of the given channel with nearby channels that, for a given profile, provides the same radiance at the observed angle as the given channel would have provided if observed at nadir. The correction procedure employed here seeks to find and use that linear combination.

For a given channel, regression coefficients are generated that give the change in radiance as a linear function of observed radiances. Radiances are used rather than brightness temperatures to avoid Planck equation calculations. The exponentiation within the Planck equation is computationally intensive. Furthermore, an error can result if a low temperature coupled with noise causes the calculated value to go negative. For daytime conditions, the predictors are principal component scores of the eigenvectors of the radiances plus the cosine of difference of the solar zenith angles between the AIRS and AMSU observations. For nighttime conditions the predictors are the principal component scores of the eigenvectors of the radiances. The additional term for daytime conditions is proportional to the change in solar energy falling on a horizontal surface due to the change in viewing angle. This term is important for the shortwave channels.

In applying the angle correction, the first step is to normalize the observed radiances by dividing by the instrumental noise for the given channel. The next step is to generate the eigenvectors of the predictors. In practice, the regression uses the 45 principal component scores for the 45 eigenvectors with the highest eigenvalues as predictors. Use of the eigenvectors prevents the solution from becoming singular. For daytime, the matrix of predictors is given by:

$$\mathbf{X_{day}} = \left[\frac{R_o(prof, fp, \nu, \varphi)}{\varepsilon(\nu)} + \left(\cos(\phi) - \cos(\phi_{cen})\right) \right] \times \mathbf{E} \tag{5.2.2}$$

for nighttime, the matrix of predictors is given by:

$$\mathbf{X_{night}} = \left[\frac{R_o(prof, fp, \nu, \varphi)}{\varepsilon(\nu)} \right] \times \mathbf{E} \tag{5.2.3}$$

where $\mathbf{E}$ denotes the matrix of eigenvectors and $\varepsilon(\nu)$ denotes the instrumental noise for the channel. Once the predictors are available, the regression is given by:

$$\bar{A}(\nu, \varphi) = \bar{C}_o(\nu, \varphi) + \bar{C}(\nu, \varphi)\bar{X}(\varphi) \tag{5.2.4}$$

where $\bar{C}(\nu, \varphi)$ denotes the vector of regression coefficients.

The vector of adjusted radiances may then be computed:

$$\bar{R}(\nu, \varphi)_{angle\_adjusted} = \bar{R}(\nu, \varphi)_{obs} + \bar{A}(\nu, \varphi) \tag{5.2.5}$$

where $\bar{R}(\nu, \varphi)_{obs}$ denotes the vector of original measured radiances.

Separate coefficients are generated for day and night. Although the daytime coefficients may be used to calculate the adjusted radiances at night, the errors that are generated are of the same magnitude as those produced during the day and thus larger than they would otherwise be. While the errors in the daytime corrections are small, nighttime corrections produced with nighttime coefficients are much more accurate. This is an important consideration because in daylight, the visible channels can be used to help cloud detection. At night, cloud detection has to rely on relationships between channels

at different wavelengths. The increased accuracy for the short wavelength channels is an important factor in the ability to detect clouds.

5.2.2 Principles of Cloud Clearing

Infrared observations at most wavelengths are affected by clouds in the field-of-view. Three basic approaches used for accounting for effects of clouds in satellite remote sensing are: 1) identify clear areas and only perform retrievals in those areas, with no cloud correction needed; 2) use channel observations in adjacent potentially partially cloudy scenes to reconstruct what the channel radiances would have been if the scenes were clear, and use these reconstructed observations to determine geophysical parameters; and 3) determine both surface and atmospheric geophysical parameters, as well as cloud properties, from the radiance observations themselves. An example of the first approach is given by Cuomo *et al.*(1993). Eyre (1989a, 1990) has used the third approach in simulation by assuming an unknown homogeneous amount of black clouds at an unknown pressure, and attempted it with real TOVS data as well (Eyre, 1989b). Our approach, like that used in Susskind (1993), is of the second type and is an extension of that used by Smith (1968), Chahine (1974), and Chahine (1977). This approach utilizes satellite observed radiances, $R_{i,k}$, corresponding to channel i and field-of-view k, made over adjacent fields-of-view. In this approach, there is no need to model the radiative and reflective properties of the clouds. The only assumption made is that the fields-of-view are homogeneous except for the amount of cloud cover in K different cloud formations in each field-of-view. $R_{i,clr}$ the radiance which would be observed if the entire field of view were clear and $R_{i,cld,\ell}$, the radiance which would be observed if the entire field of view were covered by cloud formation ℓ, are therefore assumed to have the same respective values in each field-of-view. If the observed radiances in each field-of-view are different, the differences in the observed radiances are then attributed to the differences in $\alpha_{\ell k}$, the fractional cloudiness for cloud formation ℓ in field-of-view k.

Using the above assumptions, Chahine (1977) showed that the reconstructed clear-column radiance for channel i, $\tilde{R}_{i,clr}$, can be written as a linear combination of the measured radiances in the K+1 fields-of-view, $R_{i,1} .. R_{i,K+1}$, according to

$$\tilde{R}_{i,CLR} = R_{i,1} + \eta_1 \left[R_{i,1} - R_{i,K+1}\right] + \ldots \eta_k \left[R_{i,1} - R_{i,(K+2)-k}\right] + \ldots \eta_K \left[R_{i,1} - R_{i,2}\right] \quad (5.2.6)$$

where $\eta_1 \ldots \eta_K$ are unknown channel independent constants, and K+1 fields-of-view (FOV's) are needed to solve for K cloud formations. The fields-of-view are ordered such that FOV 1 is the clearest field-of-view based on observations in the 11 μm window (the field-of-view with the highest 11 μm radiances is assumed to be FOV 1) and FOV K+1 is the cloudiest. Thus η_1 multiplies the largest radiance differences and η_K the smallest. Once $\eta_1 \ldots \eta_K$ are determined, Equation (5.2.6) is used to produce the reconstructed clear column radiances for all channels used in the retrieval process. The reconstructed clear column radiances are then used when solving for the geophysical parameters. This approach has been successfully applied to fields-of-view, assuming one cloud formation, in the analysis of HIRS2/MSU operational sounding data by several authors (McMillin and Dean, (1982), Susskind *et al.* (1984), Susskind and Reuter (1985a) and Chahine and Susskind (1989)) and is the method used by NOAA/NESDIS in production of their clear column radiances used in generation of operational HIRS2/MSU retrievals (McMillin and Dean, 1982). Chahine and Susskind (1989) show that retrieval accuracy, verified by co-located radiosondes, does not degrade appreciably with increasing cloud cover, for retrieved cloud fractions of up to 80%. Susskind and Reuter (1985b) have performed simulations with two cloud formations and three fields-of-view for the AMTS instrument -- an earlier version of AIRS (Chahine, *et al.*, 1984), used in conjunction with MSU.

The key to determining optimal values of η lies is in the best estimation of $\tilde{R}_{i,CLR}$. There are two basic approaches to this. The first uses regression-based relationships between microwave channel brightness temperatures and AIRS clear column radiances. This will be referred to as the regression based approach. The second computes the clear column radiances from a physical state, which is consistent with the microwave radiances. This will be referred to as the physically based approach. There are potential benefits to each approach, depending on the conditions encountered, and both are tested as to which performs optimally to produce clear column radiances. The regression based approach has the advantage that it can be determined from a sample of clear radiances

taken shortly after launch and produces cloud cleared radiances that are independent of any errors in the forward calculation procedure. This will be particularly useful in the early stages of operation after launch before the radiative transfer calculations have been optimized to account for detector characteristics and uncertainties in the forward model. The physically based approach has the advantage that it can be iterated and take advantage of the infrared channels as the solution improves with each iteration.

5.2.2 Physically Based Cloud Clearing

An improved physically-based methodology has been developed to account for multiple cloud formations using the AIRS/AMSU/HSB instruments, for use in the final product retrieval algorithm. This methodology is also used as part of the start up procedure to produce cloud-cleared radiances used in the first product retrieval. The methodology to determine η_k is first presented for a single cloud formation and then generalized for use with multiple cloud formations.

5.2.3 Single cloud formation with two fields-of-view

For one cloud formation and two fields-of-view, the reconstructed clear-column radiance for channel i from Equation (5.2.6) is given by

$$\tilde{R}_{i,CLR} = R_{i,1} + \eta_1 \left[R_{i,1} - R_{i,2} \right]. \tag{5.2.7}$$

Given these assumptions, the value of η_1 is independent of cloud spectral properties and has the same value for all channels. η_1 is written in terms of α_1 and α_2 as

$$\eta_1 = \frac{\alpha_1}{\alpha_2 - \alpha_1}, \tag{5.2.8}$$

where α_1 and α_2 are the cloud fractions in each field-of-view (Chahine, 1974). It is not necessary to know α_1 or α_2 to determine η_1.

The determination of η is sequential and is done in a number of passes based on the latest estimate of the surface and atmospheric parameters. An expected value of $R_{i,CLR}$ for any channel can be used to estimate η according to

$$\eta_{i,1}^{n} = \frac{R_{i,CLR}^{n} - R_{i,1}}{R_{i,1} - R_{i,2}}, \tag{5.2.9}$$

where $\eta_{i,1}^{n}$ is the n^{th} iteration estimate of η, obtained from channel i, based on the n^{th} iteration estimate of the cloud-cleared radiance $R_{i,CLR}^{n}$. $R_{i,CLR}^{n}$ is obtained by using the radiative transfer equation to compute the i^{th} channel radiance with the n^{th} pass estimates of atmospheric and surface parameters. The general iterative procedure indexed by n is discussed later.

If the estimated temperature profile is too warm (cold) over coarse layers of the atmosphere, the estimated cloud-cleared radiances $R_{i,CLR}^{n}$ are too high (low), and $\eta_{i,1}^{n}$ is too large (small). In performing HIRS2/MSU retrievals, Susskind *et al.* (1984) correct potential biases in the n^{th} iteration coarse-layer temperatures by adjusting computed brightness temperatures for the infrared channels used to estimate η. The adjustment is based on the difference between the observed brightness temperature for an AMSU channel sensitive to mid-lower tropospheric temperatures and that computed from the n^{th} iteration temperature profile. This in effect adjusted the n^{th} iterative temperature profile to be consistent with the observations in a single AMSU channel.

The superior sounding capability of AMSU, compared with MSU, is utilized to first produce an AMSU-only retrieval of atmospheric temperature-moisture profile. This is then used as the initial guess to start the retrieval process, and in the first pass estimation of η_1. The AMSU retrieval is done before the cloud correction because AMSU radiances are not affected significantly by non-precipitating clouds. The temperature retrieval obtained from AMSU has the property that radiances computed from it agree well with all AMSU channels and is unbiased over coarse layers of the atmosphere, though local errors still exist. When used in the start up mode before the first product retrieval, (n=0), the radiances are calculated based on the microwave product state. In subsequent passes, it is ensured that state also agrees with the AMSU radiances.

Using different IR channels in Equation (5.2.9) results in different estimated values of $\eta_{i,1}$ due to a combination of local errors in the temperature profile, and channel noise effects. Many channels are used to estimate η_1 in order to reduce potential errors. For the case of a single cloud formation, this is accomplished by simply taking a weighted average of $\eta_{i,1}$ over a set of cloud filtering channels to get a single value of η_1 as done in Susskind and Reuter (1985a) and Susskind *et al.*. (1993). Once a value of η_1 is computed, the cloud-cleared radiances for all channels are reconstructed using Equation (5.2.7).

If the denominator in Equation (5.2.9) is small, errors in estimating the numerator are amplified in the determination of η. Therefore, a large contrast in radiance between the two fields-of-view is important for cloud-filtering channels.

5.2.4 Channel selection for cloud filtering

Although some previous techniques (Chahine (1974), Halem *et al.* (1978), and Susskind *et al.* (1993)) used the 15 μm longwave channels for cloud clearing and the 4.3 μm channels for retrievals, the rationale for use of only 15 μm channels for cloud filtering neglected the effects of solar radiation reflected off cloud tops. When sunlight is reflected off the surface and clouds, the scene can exhibit significant contrast in the 4.3 μm region, especially for low clouds. In addition, cloud effects on radiances can be of opposite sign at short wavelengths than at long wavelengths. This change in sign eases the distinction of cloud effects on the observed radiances from thermal effects of the clear atmosphere. Therefore, it is desirable to include 4.3 μm channels in the cloud filtering set during the day. Furthermore, it is desirable to use the same methodology for both cloud filtering and retrieval of geophysical parameters during the day and night. We therefore use both 15 μm and 4.3 μm channels to estimate η. The 15 μm and 4.3 μm cloud-filtering channels are a subset of those used to determine the atmospheric temperature profile. Window channels are more sensitive to clouds than atmospheric sounding channels, but are also more sensitive to uncertainties in surface parameters. Tthe methodology has been improved to include window channels in the determination of η, weighted to reflect the uncertainty in the clear-column radiances. The same weighting

procedure is used for all channels. The relative weighting of the 15 μm and 4.3 μm channels in the determination of η is done objectively and differs under daytime and nighttime conditions as is described later.

5.2.5 Determination of η for a single cloud formation

Figure 5.2.1 is a flow diagram for the cloud-clearing program.

Following Susskind *et al.* (1993), set

$$\eta = \frac{\sum_{i}^{I} W_i^2 \, \eta_i}{\sum_{i} W_i^2} \tag{5.2.10}$$

where W_i is a weight for channel i. An appropriate value of W_i account s for propagated errors in η_i resulting from instrumental and computational noise. For example, channels more sensitive to clouds, with large values of $\left| R_{i,1} - R_{i,2} \right|$, receive larger weight.

Equation (5.2.9) for i channels becomes in matrix form

$$\mathbf{W}\left(\bar{R}^n_{clr} - \bar{R}_1\right) = \mathbf{W}\left(\bar{R}_1 - \bar{R}_2\right) \eta^n \tag{5.2.11}$$

where **W** is an I x I diagonal weight matrix with weight W_{ii} for channel i, $\left(\bar{R}^n_{clr} - \bar{R}_1\right)$ and $\left(\bar{R}_1 - \bar{R}_2\right)$ are I x 1 vectors, and η^n is the unknown. The standard weighted least squares solution to this matrix problem is given by

$$\eta^n = \left[\left(\bar{R}_1 - \bar{R}_2\right)^T \mathbf{W}^T \mathbf{W} \left(\bar{R}_1 - \bar{R}_2\right)\right]^{-1} \left(\bar{R}_1 - \bar{R}_2\right)^T \mathbf{W}^T \mathbf{W} \left(\bar{R}^n_{clr} - \bar{R}_1\right) \tag{5.2.12}$$

and reduces to

$$\eta^n = \frac{\sum_i W_{ii}^2 \left(R_{i,1} - R_{i,2}\right)\left(R_{i,clr}^n - R_{i,1}\right)}{\sum_i W_{ii}^2 \left(R_{i,1} - R_{i,2}\right)^2} = \frac{\sum_i W_{ii}^2 \left(R_{i,1} - R_{i,2}\right)^2 \eta_i^n}{\sum_i W_{ii}^2 \left(R_{i,1} - R_{i,2}\right)^2} \quad (5.2.13)$$

where η_i^n is given by Equation (5.2.9). Equation (5.2.13) is analogous to Equation (5.2.10), but in Equation (5.2.13), the contribution of the difference of radiances in the two fields-of-view to the channel weight is explicitly taken into account. Therefore W_i in this context represents any residual weight factors, such as effects of channel noise. Susskind *et al.* (1993) used Equation (5.2.11), including in W_i the term $\left|\Theta_{i,1} - \Theta_{i,2}\right|^2$, that is roughly proportional to $\left|R_{i,1} - R_{i,2}\right|^2$ for the 15 μm channels they used.

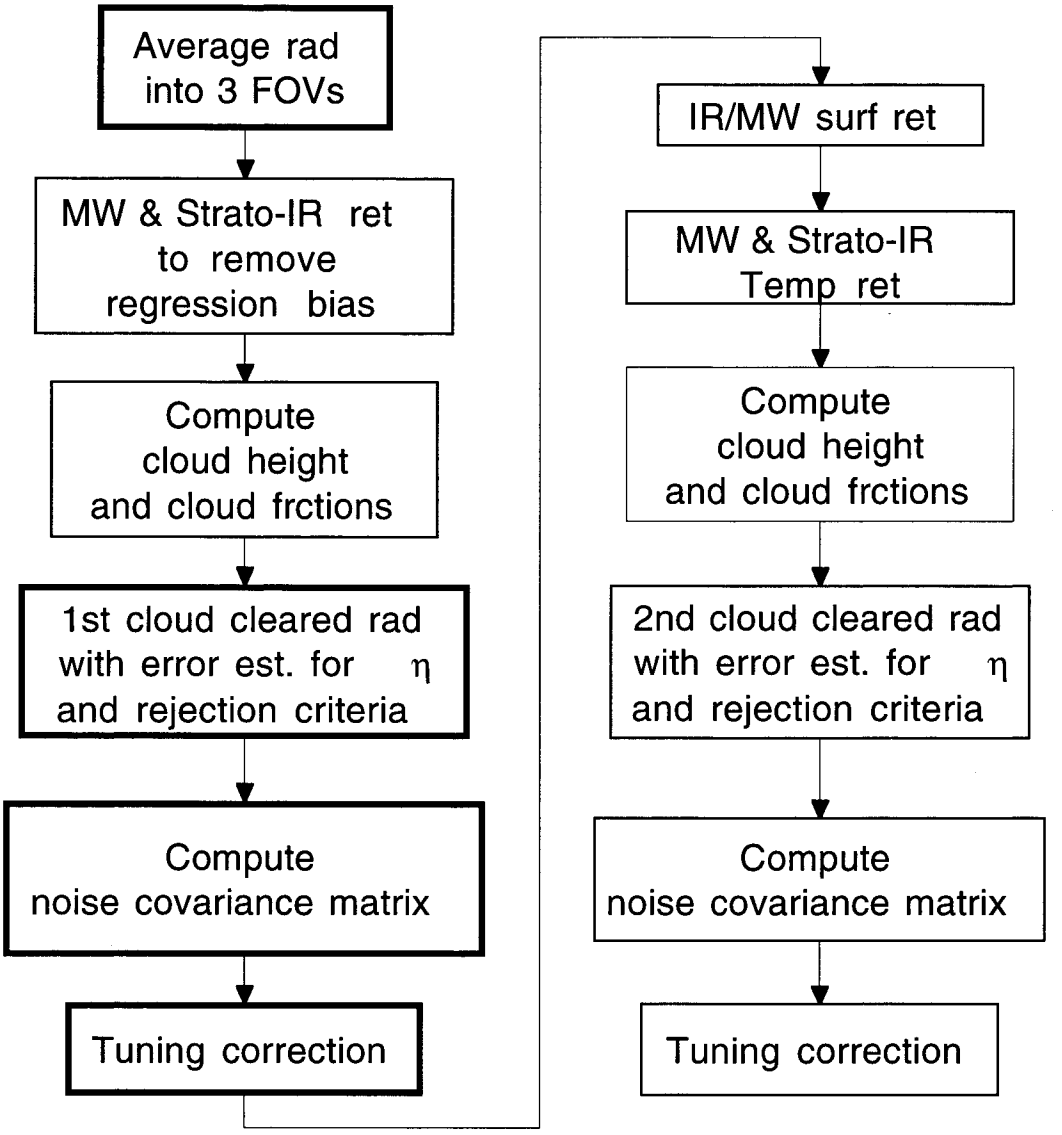

FIGURE 5.2.1 CLOUD CLEARING FLOW DIAGRAM. NOTE: THE FIRST PRODUCT EXEXUTES THE CLOUD-CLEARING MODULE IN HIGHLIGHTED SEGMENTS ONLY WHILE THE FINAL PRODUCT EXECUTES THE COMPLETE CLOUD-CLEARING PROCESS.

The above discussion is accurate as long as sources of channel noise are uncorrelated from channel-to-channel. Under these conditions, an appropriate value of W_i is inversely

proportional to sources of noise. There are two sources of noise in Equation (5.2.11), instrumental noise and computational noise. Instrumental noise is random and affects $R_{i,1}$ and $R_{i,2}$. Computational noise affects $R^n_{i,CLR}$ and are correlated channel-to-channel. In the case of channel correlated noise, the appropriate equation is

$$\eta^n = \left[\left(\bar{R}_1 - \bar{R}_2\right)^T \hat{\mathbf{M}}^{-1} \left(\bar{R}_1 - \bar{R}_2\right) \right]^{-1} \left(\bar{R}_1 - \bar{R}_2\right)^T \hat{\mathbf{M}}^{-1} \left(\bar{R}^n_{CLR} - \bar{R}_1\right) \quad (5.2.14)$$

where $\hat{\mathbf{M}}$ is the channel noise covariance matrix, indicating errors in $\left(\bar{R}^n_{CLR} - \bar{R}_1\right)$.

The iterative methodology to determine cloud-cleared radiances consists of three passes to determine η^n (n=1,2,3), using three sets of conditions, to give $\bar{R}^n_{CLR}$, in which $\bar{R}^n_{CLR}$ and hence η^n become increasingly more accurate in each iteration. Each pass has its own $\hat{\mathbf{M}}$, reflecting expected errors in $R^n_{i,CLR} - R_{i,1}$. The noise covariance matrices are modeled according to

$$\hat{M}^n_{ij} = N_{ij} + \frac{\partial R_i}{\partial T_S}\frac{\partial R_j}{\partial T_S}\left(\delta T^n_S\right)^2 + \frac{\partial R_i}{\partial \varepsilon_{\nu_l}}\frac{\partial R_j}{\partial \varepsilon_{\nu_m}}\left(\delta\varepsilon^n_{\nu_l}\delta\varepsilon^n_{\nu_m}\right) + \frac{\partial R_i}{\partial \rho_i}\frac{\partial R_j}{\partial \rho_j}\left(\delta\rho_i\,\delta\rho_j\right)^2 + \frac{\partial R_i}{\partial T(p)}\frac{\partial R_j}{\partial T(p)}\left(\delta T^n(p)\right)^2 + \frac{\partial R_i}{\partial \ln(q)}\frac{\partial R_j}{\partial \ln(q)}\left(\delta \ln(q)\right)^2 \quad (5.2.15)$$

where **N** is the observed noise covariance matrix (see section 5.3.8, and equation 5.3.33) and the remaining terms are contributions to errors in the computed value $R^n_{i,CLR}$ from errors in estimated surface skin temperature, surface spectral emissivity, surface spectral bi-directional reflectance of solar radiation, and temperature and moisture profile respectively. The partial derivatives are determined empirically by computing the radiance using the current estimate of each parameter and recomputing it after a small change in that parameter. The profile terms are obtained by either shifting the entire temperature profile by $\delta T(P)$ or multiplying the moisture profile by $(1+\delta q(P))$. In Susskind *et al.* (1998), the uncertainties, such as δT^n_S, are specified so as to be indicative

of the expected errors for that parameter in the n^{th} iteration. These errors are predicted on a profile-by-profile basis for each pass by propagating the expected sources of error through the retrieval process in the manner described in Section 5.4. A principal source of retrieval error arises from errors in the reconstructed cloud-cleared radiances. These errors propagate into degraded estimates of all the variables shown in Equation (5.2.15).

5.2.6 Multiple Cloud Formations with Multiple Fields-of-View

In order to solve for K cloud formations with unknowns $\eta_1 \ldots \eta_K$, K+1 fields-of-view are needed. A simple relationship between α_k and η_k does not exist for the case of multiple cloud formations, nor is the solution $\eta_1 \ldots \eta_K$ necessarily unique. For example, consider a case of only one cloud formation with cloud fractions of 20%, 40%, and 60% in fields-of-view 1 - 3 respectively. $\eta_1^{(1)} = 1$, $\eta_2^{(1)} = 0$ and $\eta_1^{(2)}=0$, $\eta_2^{(2)} = 0.5$ are two solutions to the problem, as are appropriate linear combinations of these solutions, given by

$$\begin{pmatrix} \eta_1 \\ \eta_2 \end{pmatrix} = (1-f)\begin{pmatrix} \eta_1^{(1)} \\ \eta_2^{(1)} \end{pmatrix} + f\begin{pmatrix} \eta_1^{(2)} \\ \eta_2^{(2)} \end{pmatrix} \tag{5.2.16}$$

The optimal solution provides the correct cloud-cleared radiances and does so with the smallest values of η in order to minimize amplification of instrumental noise when used in Equation (5.2.6).

Determining an optimal set of η_k is analogous to the determination for a single cloud formation. Using a set of I channels to estimate K values of η, Equation (5.2.6) is expressed as a set of linear equations in matrix form according to

$$\begin{pmatrix} \tilde{R}^n_{1,CLR} - R_{1,1} \\ \tilde{R}^n_{2,CLR} - R_{2,1} \\ \vdots \\ \tilde{R}^n_{I,CLR} - R_{I,1} \end{pmatrix} = \begin{pmatrix} R_{1,1} - R_{1,K+1} & R_{1,1} - R_{1,K} & \cdots & R_{1,1} - R_{1,2} \\ R_{2,1} - R_{2,K+1} & R_{2,1} - R_{2,K} & \cdots & R_{2,1} - R_{2,2} \\ \vdots & \vdots & \ddots & \vdots \\ R_{I,1} - R_{I,K+1} & R_{I,1} - R_{I,K} & \cdots & R_{I,1} - R_{I,2} \end{pmatrix} \begin{pmatrix} \eta_1^n \\ \eta_2^n \\ \vdots \\ \eta_K^n \end{pmatrix} \tag{5.2.17}$$

or

$$\bar{C}^n = \mathbf{D}\,\bar{\eta}^n \quad , \tag{5.2.18}$$

The solution to Equation (5.2.18) is given by

$$\bar{\eta}^n = \left(\mathbf{D}^T\,\hat{\mathbf{M}}^{-1}\,\mathbf{D}\right)^{-1}\mathbf{D}^T\,\hat{\mathbf{M}}^{-1}\,\bar{C}^n \tag{5.2.19}$$

where $\hat{\mathbf{M}}$ is the channel noise covariance matrix as given in Equation (5.2.15). Given η^n, $\tilde{R}^n_{i,CLR}$ is constructed for all channels according to Equation (5.2.6). $\tilde{R}^n_{i,CLR}$ is used as the observation in the subsequent retrieval process. If the observation in a channel is not sensitive to the presence of clouds in the field-of-view, it is better to average the observations in all fields-of-view

$$\tilde{R}^n_{i,CLR} = \frac{1}{K+1}\sum_{k=1}^{K+1} R_{i,k} \tag{5.2.20}$$

This is equivalent to defining separate values of η for channels that do not see clouds, $\bar{\eta}^n_{i,CLR} = -\frac{1}{K+1}$, and using them to produce $\tilde{R}^n_{i,CLR}$ for the appropriate channels. Currently, channel i is considered not to be sensitive to clouds if $\left|R_{i,1} - R_{i,k+1}\right| \le 3\sqrt{2}\,\mathbf{N}_i$ and it is included in a set of channels expected not to see clouds given the retrieved cloud height.

The first product retrieval algorithm calls the first part of the composite cloud-clearing package once, to provide the cloud-cleared radiance for inversion to thermal and humidity profiles. The final retrieval algorithm calls the complete composite cloud-clearing package twice, providing cloud heights and cloud fractions in addition to cloud-cleared radiances.

5.2.6.1 Contribution of clouds to the retrieval channel noise covariance matrix

The basic retrieval methodology described in Section 5.4 requires a channel noise covariance matrix **M** representing channel correlated errors in the terms $\left(\tilde{R}_{i,CLR} - R^n_i\right)$ and $\left(\tilde{R}_{j,CLR} - R^n_j\right)$ where R^n_i is the radiance computed for channel i

based on the n^{th} iterative solution. The optimal solution for η minimizes the noise in the cloud-cleared radiances. The channel noise covariance matrix is the sum of two parts, resulting from noise in the reconstructed clear column radiances $\delta\tilde{R}_i$ with noise covariance $\tilde{\mathbf{M}}$, and noise in the computed radiances δR_i^n due to uncertainty in the parameters, with noise covariance $\mathbf{M}$. $\tilde{\mathbf{M}}_{ii} = \left[\delta\tilde{R}\delta\tilde{R}^T\right]_{ii}$ is the expected noise covariance matrix for the channel clear-column radiances. The noise in $\tilde{R}_{i,CLR}$ obtained from Equation (5.2.6) has two parts, arising from instrumental noise $\mathbf{N}_i$, and from cloud clearing errors coming from errors in η_k, which may be correlated with each other. Even if the vector η_k were perfect then

$$\tilde{\mathbf{M}}_{ii} = \left[\delta\tilde{R}\delta\tilde{R}^T\right]_{ii} = \mathbf{N}_i^2\left[\left(1+\sum_k \eta_k\right)^2 + \sum_k \eta_k^2\right] \equiv \mathbf{N}_i^2\left[A(\eta_k)\right]^2 \qquad (5.2.21)$$

In general, $A(\eta_k)$ is a channel noise amplification factor resulting from extrapolating cloud contaminated observed radiances to cloud-cleared radiances.

Cloud-cleared radiances for those channels affected by clouds have an additional error due to errors in η, giving the final result

$$\tilde{\mathbf{M}}_{ij} = \left[\delta\tilde{R}\delta\tilde{R}^T\right]_{ij} = \mathbf{N}_{ij}^2\left[A(\eta_k)\right]^2 + \left[\mathbf{D}\delta\eta\delta\eta^T\mathbf{D}^T\right]_{ij} \qquad (5.2.22)$$

and where $\delta\eta\delta\eta^T$ is the error covariance of η and $\mathbf{D}$ is defined in Equation (5.2.18). If $\hat{\mathbf{M}}$, as defined in Equation (5.2.15), is indeed representative of the noise in the determination of η, then

$$\left[\delta\eta\delta\eta^T\right] = \left[\mathbf{D}\,\hat{\mathbf{M}}^{-1}\mathbf{D}^T\right]^{-1} \qquad (5.2.23)$$

where $\mathbf{D}$ in Equation (5.2.23) refers only to those channels used to determine η. $\delta\eta\delta\eta^T$ is therefore based only on observed channel radiance differences in the separate fields-of-view and the modeled channel noise covariance matrix used to determine η,

and hence is easily computed for a given profile and substituted in Equations (5.2.22) to give $\tilde{\mathbf{M}}$ for channels affected by clouds.

In the special case for which channel i is determined to not "see" the clouds (i.e., stratospheric sounding channels or tropospheric sounding channels peaking significantly above the highest cloud top), radiances in the k fields-of-view are averaged for the cloud-cleared radiances. For these channels, the scene appears to be clear and effective values of η_{CLR} are defined for "clear" channels as $\eta_{CLR} = -1/(K+1)$. For these channels, $A(\eta_{CLR,k}) = \frac{1}{\sqrt{k+1}}$, which is a noise reducer. For "clear" channel i,

$$\tilde{M}_{ij} = \frac{1}{k+1} N_{ij}^2 \delta_{ij} \qquad (5.2.24)$$

where j is any other channel and δ_{ij} is the Kronecker delta function.

Even if only 2 cloud formations exist, it is better to make use of the characteristics of radiances in all 9 fields-of-view than to arbitrarily divide the 9 spots into 3 equal area fields of view as done by Susskind et al. (1998). There are numerous reasons for this. Equation (5.2.6) extrapolate $\tilde{R}_{i,CLR}$ from $R_{i,1}$ with coefficients η_k. One desires:

(1) $R_{i,1}$ to be as close to $\tilde{R}_{i,CLR}$ as possible to minimize extrapolation,
(2) to maximize the contrast between different fields-of-view to have lower values of η_k and less noise amplification, and
(3) to use the average of many fields-of-view to minimize noise effects.

If, for examples, footprints 1 and 2, 3-7, and 8 and 9 each have roughly equivalent scenes, it is better to group them accordingly to form the three fields-of-view.

5.2.6.2Selection of Optimal Fields of View

Rather than choose radiances for the warmest field-of-view to be the average of the three highest radiance valued observations, N_a is the average of nearly equivalent observations to give $\underline{R_{i,1}}$, where N_a is variable and scene dependent. This leaves 9-N_a=N_f other fields of view (when dealing with observations in 9 spots) giving the equation

$$\tilde{R}_i = \underline{R_{i,1}} + \sum_{k=1}^{N_f} \eta_k (\underline{R_{i,1}} - R_{i,9-k+1}) = \underline{R_{i,1}} + \sum_k \eta_k \Delta R_{i,k} \qquad (5.2.25)$$

It is advantageous to take a linear combination of the remaining N_f fields of view

$$\underline{R_{i,1}} = \sum_{k,k'} U_{k,k'} R_{i,k'} \qquad (5.2.26)$$

where **U** is dimensioned N_f x N_f. **U** is chosen so as to diagonalize $\left[\mathbf{D}^T \hat{\mathbf{M}}^{-1} \mathbf{D}\right]$

$$\left[\mathbf{U}^T (\mathbf{D}^T \hat{\mathbf{M}}^{-1} \mathbf{D}) \mathbf{U}\right]_{j,j'} = \lambda_j \delta_{j,j'} \qquad (5.2.27)$$

The solution in this transformed space becomes

$$\tilde{R}_i = \underline{R_{i,1}} + \sum_{k=1}^{N_f} \underline{\eta_k} (\underline{R_{i,1}} - \underline{R_{i,9-k+1}}) = \underline{R_{i,1}} + \sum_k \underline{\eta_k} \underline{\Delta R_{i,k}} \qquad (5.2.28)$$

where

$$\underline{\vec{\eta}} = \mathbf{U}^T \vec{\eta} \text{ and } \vec{\eta} = \mathbf{U} \underline{\vec{\eta}} \,. \qquad (5.2.29)$$

The solution for $\underline{\vec{\eta}}$ is given by

$$\underline{\eta_j} = (\Delta \underline{R_{CLR}^T} \mathbf{N}^{-1} \Delta \underline{R_{CLR}})_{jj}^{-1} (\Delta \underline{R_{CLR}^T} \mathbf{N}^{-1} \Delta \underline{R_{CLR}})_{j,1} = \lambda_j^{-1} (\Delta \underline{R_{CLR}^T} \mathbf{N}^{-1} \Delta \underline{R_{CLR}})_{j,1} \qquad (5.2.30)$$

where $\Delta \underline{R_{CLR}}$ is $(R^n_{j,CLR} - \underline{R_{j,1}})$. Cloud-cleared radiances are most easily obtained in the untransformed space using Equations (5.2.30), (5.2.29), and (5.2.25).

If all N_f eigenfunctions of **U** are used in Equations (5.2.28) and (5.2.30), then the results would be identical to those in the untransformed space. The eigenvalues λ_j provide information about the degrees of freedom in the observed radiances. Significant eigenvalues correspond to different cloud formations in the scene, while small eigenvalues arise from various sources of noise such as instrumental noise and non-homogeneities in the clear portion of the scene. The solution is stabilized in transformed

space by keeping only a subset of N_s eigenvectors, which provide the N_s optimal linear combinations of observations in untransformed space.

The eigenvalues are representative of signal-to-noise in the solutions. Typical eigenvalues for the first cloud formation are the order of 10000 and for the second, the order of 1000. Subsequent eigenvalues in cases with a two cloud formations are typically less than 100. Eigenvectors with eigenvalues less than 20 are eliminated.

Aside from reducing noise and determining the number of cloud formations from the data, transforming the fields-of-view provides a better treatment of the estimated noise in the cloud-cleared radiances because the error in $\underline{\eta_j}$ is uncorrelated with that in $\underline{\eta_{j'}}$. The contribution to the channel noise covariance matrix arising from instrumental noise

$$\tilde{\mathbf{M}}_{ij} = \mathbf{N}_{ij}\left[\frac{1}{N_a}(1+\sum_{k=1}^{N_S}\underline{\eta_k})^2+\sum_k\underline{\eta_k^2}\right]\delta_{ij}+\left[\sum_k(\Delta\underline{R_{ik}}\,\Delta\underline{R_{jk}}\,\lambda_k^{-1})^2\right]^{1/2} \tag{5.2.31}$$

where λ_k^{-1} can be shown to be a statistical estimate of $\left(\delta\underline{\eta_k}\,\delta\underline{\eta_k^T}\right)$ if N_{ij} represents the true noise covariance error. Hence, the details of the channel noise covariance matrix are not needed to compute $\tilde{\mathbf{M}}$.

The accuracy of λ_k^{-1} is predicted from the subset of N_c cloud clearing channels. Calculate the RMS of the radiance residuals as the difference between the cloud cleared radiance estimate, $R^n_{i,CLR}$, and the cloud cleared radiance value, $\tilde{R}_{i,CLR}$, over the N_c cloud clearing channels. The prediction is accurate if this matches $\sum_i \tilde{M}_{ii}$. The case dependent uncertainty in the noise covariance is given by the difference of these two values

$$\delta\varepsilon^2 = \frac{1}{N_c}\sum_{i=1}^{N_c}(R^n_{i,CLR}-\tilde{R}_i)^2-\frac{1}{N_c}\sum_{i=1}^{N_c}\tilde{\mathbf{M}}_{ii}\ . \tag{5.2.32}$$

To produce a more accurate estimate of the channel noise covariance matrix, an additional uncertainty is added to the extrapolation uncertainty estimate, $\delta\vec{\eta}$, if $\delta\varepsilon^2$ is positive. The best way to add the uncertainty is to only modify the predicted value of $\delta\eta_1$, since higher order $\delta\eta_j$ terms require more knowledge of the interaction extrapolation parameters for multiple cloud formations. Therefore, only $\delta\eta_1$ is modeified if $\delta\varepsilon^2$ is positive, by adding a term $\delta'\eta_k$ as follows

$$\delta'\eta_k = 0 \qquad \text{for} \qquad k > 1$$

$$\delta'\eta_k^2 = \frac{\delta\varepsilon^2}{S_1^2} + 0.01^2 \qquad \text{for } k = 1 \tag{5.2.33}$$

where S_1 is the RMS channel contrast in transformed space

$$S_1^2 \equiv \frac{1}{N_c} \sum_{i=1}^{N_c} \left(\Delta R_{i,1}\right)^2 \quad . \tag{5.2.34}$$

The additional factor of 0.01 is to allow for a null space error between the surface retrieval and the cloud clearing parameter retrieval. The total error estimate for the cloud cleared radiances for all the channels is now expressed as

$$\tilde{M}_{ij} = N_{ij} \cdot A^2 \delta_{ij} + \left[\sum_k \left[\Delta R_{ik}\, \Delta R_{jk} (\lambda_k^{-1} + \delta'\eta_k^2) \right]^2 \right]^{1/2} \tag{5.2.35}$$

where A is the noise amplification factor shown in the first bracket in Equation (5.2.31). The ability to average N_a spots to produce radiances for field of view 1 significantly reduces A. The use of the truncated transformation matrix **U** also lowers the noise amplification factor, as low values of λ_k which would contribute to large values of η_k have been eliminated.

From Equations (5.2.31) and (5.2.35), it is apparent that increasing N_a is desirable. On the other hand, it is also desirable to maximize contrast between the fields-of-view to minimize the values of η and extrapolate least from R_{i1}. The field-of-view containing

the highest radiance in a select 8 μm cloud filtering window channel is always included in $\bar{R}_1$. In addition, for each other field-of-view, the standard deviation is evaluated over all cloud filtering channels of the difference between this radiance and that in field-of-view 1

$$\sigma_s = \left[\frac{1}{N_c} \sum_{i=1}^{Nc} \left(\frac{R_{i,1} - R_{i,s}}{N_{ii}} \right)^2 \right]^{1/2} \tag{5.2.36}$$

and select the radiances in fields-of-view to be averaged with $R_{i,1}$ into $\underline{R_{i,1}}$ if $\sigma_s <$ 0.3 or $\sigma_s < 0.2$ MAX (σ_s). If more than three fields-of-view satisfy this criterion, the three with the lowest standard deviations are selected, so as to maximize N_a at 4. A special case arises if all eigenvalues λ_k are less than 20. Here, no clouds are present and set $N_a = 9$, averaging radiances in all 9 spots.

5.2.6.3 Regression Approach to Find $\tilde{\mathbf{R}}_{\mathbf{i,CLR}}$

An alternative to computing $\tilde{R}_{i,CLR}$ is to use regression-based relationships between AMSU observations and clear column radiances for a set of AIRS driver channels. These relationships are found shortly after launch by identifying areas where no clouds are thought to be present in any of the 9 fields-of-view. Such areas are identified when only low eigenvalues of $(\mathbf{D}^T \hat{\mathbf{M}}^{-1} \mathbf{D})$ exist [see Equation (5.2.27)] and the values of $R^n_{i,CLR}$ computed physically are very close to $\tilde{R}_{i,CLR}$. The regression-based approach depends on driver channels. These are channels for which an estimate of the clear column radiance is obtained from the microwave measurements. These channels are selected in the following manner. For each of 10 atmospheric microwave channels (5-14), the four AIRS channels with the highest correlation with a particular AMSU channel are selected. Although only one channel is needed, four are selected to reduce the noise in this crucial step. Then angle dependent regression coefficients are generated, based on observations in the clear cases, to predict each of these 40 AIRS channels from the 10 AMSU

channels. The predicted cloud-cleared radiances become the values of $\tilde{R}_{i,CLR}$ used in subsequent inversion of level 2 parameters.

5.3 First Product

5.3.1 AIRS First Guess Regression Procedure

An eigenvector global regression procedure provides fast and accurate initial guesses for temperature and moisture profiles as well as surface emissivity. All independent AIRS radiances are preprocessed by the cloud-clearing module described in the last section. Following the approach of Smith & Woolf (1976), eigenvectors from a brightness temperature covariance matrix, calculated over some dependent training ensemble, are used as basis functions to represent the AIRS/AMSU/HSB radiometric information. Eigenvectors of covariance matrices are commonly referred to as **Empirical Orthogonal Functions** (**EOF**'s) in the literature, a convention that will be adopted throughout the remainder of this section. Because of the large number of channels measured by AIRS/AMSU/HSB, the eigenvector form of regression is crucial for exploiting the information content of all channels in a computationally efficient form. By representing radiometric information in terms of a reduced set of EOF's (much fewer in number than the total number of instrument channels) the dimension of the regression problem is reduced by approximately two orders of magnitude. Another advantage of using a reduced set of EOF's is that the influence of random noise is reduced by elimination of higher order EOF's which are dominated by noise structure. It should be noted that if all EOF's are retained as basis functions the eigenvector regression reduces to the ordinary least squares regression solution in which satellite measurements are used directly as predictors. The mathematical derivation of the EOF regression coefficients is detailed in the following sub-sections.

5.3.2 Generating the Covariance Matrix and Regression Predictors

A training ensemble of temperature, humidity, and ozone profile data are used to generate brightness temperatures for all AIRS/AMSU/HSB channels. The deviations of the brightness temperatures from their sample mean are stored in the matrix $\Delta\Theta_{Train}$, a matrix of dimensions [**nchan** x **nsamp**], where **nsamp** is the sample size of the training data set and **nchan** is the total number of instrument channels. The brightness

temperature covariance matrix from which the EOF's are derived is then generated as follows:

$$\Theta_{\mathbf{cov}} = \frac{1}{\mathrm{nsamp}} \Delta\Theta_{\mathbf{Train}} (\Delta\Theta_{\mathbf{Train}})^{T} \tag{5.3.1}$$

where superscript T denotes matrix transpose and the matrix Θ_{cov} is a square matrix of order **nchan**. The diagonal elements of Θ_{cov} represent the variance of the respective channel brightness temperatures while the off diagonal elements represent the covariance between pairs of channels. An eigenvector decomposition is performed on the matrix Θ_{cov} giving:

$$\Theta_{cov} = \Gamma \Lambda \Gamma^{T} \tag{5.3.2}$$

where Γ is the [**nchan** x **nchan**] matrix containing the eigenvectors, or EOF's, of Θ_{cov} in its columns. Λ is the diagonal matrix of eigenvalues, the first eigenvalue being the first diagonal element, the second eigenvalue the second diagonal element, etc. The EOF's are ordered in terms of the amount of the total data variance each explains; the first explains the most variance and each successive EOF explains progressively less of the total data variance. As discussed in the beginning of this section, some subset of the total number of EOF's is best for capturing the information content of the radiometric data while minimizing the effects of random measurement noise. For the purposes of notation let **m** be the optimal number of EOF's for describing the information content of the covariance matrix from Equation (5.3.14). Considering the large number and interdependent nature of the AIRS/AMSU/HSB weighting functions it is reasonable to assume that **m** << **nchan**, where **m** represents in some sense the number of independent pieces of information available from the measurements. Experiments with AIRS/AMSU/HSB simulated data have shown **m** = 40 to be optimal for capturing the information content of the measurements from these three instruments. Only very small improvements in retrieval accuracy have been observed when using greater numbers of eigenvectors. Once **m** is determined from experimentation those EOF's are used as basis functions to represent the original brightness temperature information in terms of

expansion coefficients commonly referred to as **principal components**. First we express $\Delta\Theta_{Train}$ as an expansion of the EOF's as follows:

$$\Delta\vec{T}^{j}_{Train} = a^{j}_{1}\tilde{\Gamma}_{1} + a^{j}_{2}\tilde{\Gamma}_{2} + \cdots + a^{j}_{m}\tilde{\Gamma}_{m} \tag{5.3.3}$$

where $\Delta\vec{T}^{j}_{Train}$ is the jth column of matrix $\Delta\Theta_{Train}$ and $a^{j}_{1}, a^{j}_{2}, \cdots, a^{j}_{m}$ are the corresponding m principal components for the jth sample. In order to solve Equation (5.3.16) for the individual principal components recall that the EOF's $\tilde{\Gamma}_{1}, \tilde{\Gamma}_{2}, \cdots, \tilde{\Gamma}_{m}$ are mutually orthonormal. That is:

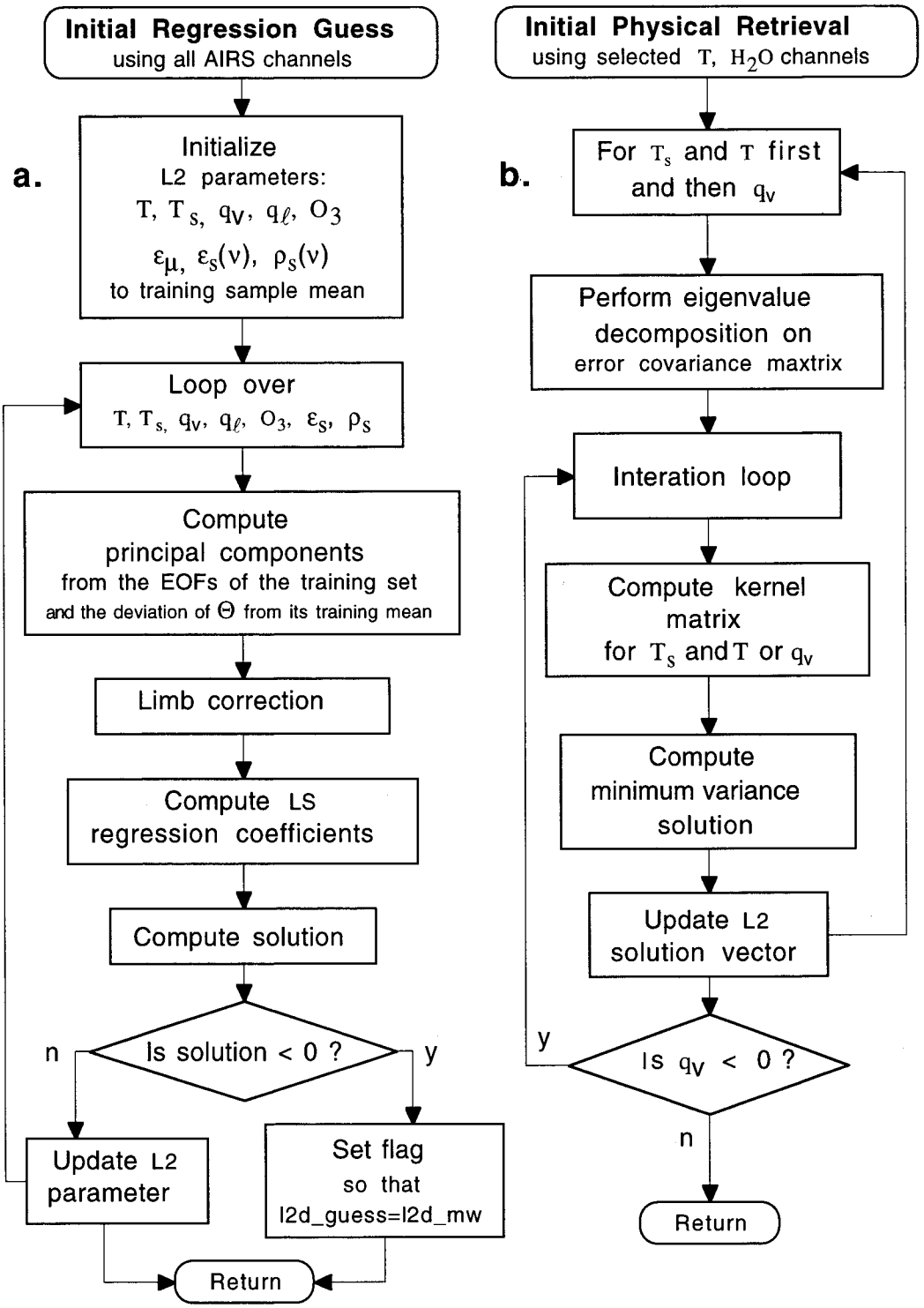

FIGURE 5.3.1 FIRST PRODUCT FLOW DIAGRAM: A) INITIAL REGRESSION AND B) PHYSICAL RETRIEVAL

$$\tilde{\Gamma}_i \bullet \tilde{\Gamma}_j = \begin{cases} 1 & \text{for } i = j \\ 0 & \text{for } i \neq j \end{cases} \tag{5.3.4}$$

where (•) denotes the *inner product* of two vectors. Using the condition of orthonormality and the distributive property of the (•) operator, each individual principal component is expressed as:

$$a_i^j = \Delta T_{Train}^j \bullet \tilde{\Gamma}_i \qquad \begin{array}{l} i = 1, 2, \cdots, \text{ m and} \\ j = 1, 2, \cdots, \text{ nsamp} \end{array} \tag{5.3.5}$$

5.3.3 Generating the Regression Coefficients

A standard least squares regression technique is used to generate regression coefficients using an *a priori* training database such as an operational radiosonde match file. The following regression model is used to generate the coefficients:

$$\Delta \mathbf{V} = \mathbf{C}\mathbf{A}_{Train} \tag{5.3.6}$$

where $\Delta \mathbf{V}$ is the matrix of deviations of the predictants (temperature, moisture etc.) from the training sample mean, $\mathbf{A}_{Train}$ is the [**m** x **nsamp**] matrix of principal components calculated using Equation (5.3.5), and **C** is the [**n** x **m**] matrix of regression coefficients to be solved for where **n** is the total number of predictants. More specifically:

$$\Delta \mathbf{V} = \begin{bmatrix} V_1^1 - \overline{V}_1 & V_1^2 - \overline{V}_1 & \cdots & V_1^{nsamp} - \overline{V}_1 \\ \vdots & \vdots & \vdots & \vdots \\ V_n^1 - \overline{V}_n & V_n^2 - \overline{V}_n & \cdots & V_n^{nsamp} - \overline{V}_n \end{bmatrix} \tag{5.3.7}$$

and,

$$\mathbf{A}_{Train} = \begin{bmatrix} a_1^1 & a_1^2 & \cdots & a_1^{nsamp} \\ \vdots & \vdots & \vdots & \vdots \\ a_m^1 & a_m^2 & \cdots & a_m^{nsamp} \end{bmatrix} \tag{5.3.8}$$

where **n** = number of predictants (i.e. the number of temperature, moisture, and/or emissivity/reflectivity points), **nsamp** = number of samples in the training set, **m** = number of principal components used and bars indicate averages over the training sample set.

The least squares regression solution of Equation (5.3.6) is:

$$\mathbf{C} = \Delta\mathbf{V}\mathbf{A}_{\text{Train}}^{\text{T}}(\mathbf{A}_{\text{Train}}\mathbf{A}_{\text{Train}}^{\text{T}})^{-1} \tag{5.3.9}$$

where the T superscript denotes matrix transpose, and the -1 superscript denotes matrix inversion.

5.3.4 Applying the Coefficients to Independent Data

Once the coefficient matrix, **C**, is calculated from equation (5.3.9) the coefficients may be applied to independent data using equation (5.3.6). The matrix defined in equation (5.3.20) would now contain deviations of the independent data from the training sample mean. Mathematically, the application process is:

$$\mathbf{V} = \overline{\mathbf{V}} + \mathbf{C}\mathbf{A}_{\text{obs}} \tag{5.3.10}$$

where **V** is the [**n** x **nobs**] matrix of retrievals, $\overline{\mathbf{V}}$ the training vector from equation (5.3.7), **C** is the [**n** x **m**] matrix of regression coefficients from equation (5.3.9), and $\mathbf{A}_{\text{obs}}$ is the [**m** x **nobs**] matrix of principal components calculated from the level 1B observations. $\mathbf{A}_{\text{obs}}$ is generated using equation (5.3.5) where $\Delta\Theta_{\text{Train}}$ is replaced with $\Delta\Theta_{\text{obs}}$, the matrix of deviations of observed brightness temperatures from the training mean.

To account for off-nadir view positions the principal components in equation (5.3.10) are adjusted to nadir. This is accomplished by generating *a priori* coefficients to predict nadir principal components from off-nadir principal components (i.e. limb adjustment). Limb adjustment is used only in the regression step. The physical retrieval algorithms are applied to radiances at the given view angle.

5.3.5 Minimum Variance Physical Retrieval

Given a set of radiances, the objective of a physical retrieval algorithm is to find a realistic solution of geophysical parameters that will be consistent with those radiances.

The derivation begins with linearizing the radiative transfer equations (RTE) for microwave and infrared about some *a priori* estimate. This is accomplished by

expressing brightness temperature or radiance (R_υ^c) in equations (4.1.2) and (4.2.1) as a function of the regression guess using a first order Taylor expansion such that:

$$R_\upsilon^c = R_\upsilon^0 + \sum_{k=1}^{N} \frac{\partial R_\upsilon}{\partial V_k}(V_k - V_k^0) \tag{5.3.11}$$

where R_υ^0 is the total integrated radiance for frequency υ computed from the regression solution and the RTE, V_k and V_k^0 are the kth elements of the solution and regression first guess geophysical parameter vectors, $\partial R_\nu / \partial V_k$ is the incremental change of the radiance with respect to a incremental change in a particular geophysical parameter (e.g. V_k= temperature at 50 mb), and N is the number of geophysical parameters. The value of $\partial R_\nu / \partial V_k$ is computed in a manner similar to Eyre (1989a) by differentiating the numerical quadrature form of the RTE with respect to the geophysical parameters (see section "Computation of the Kernel Matrix"). Currently the geophysical parameters solved in the physical retrieval include surface and atmospheric temperature and moisture. The above equation is re-expressed in matrix notation as,

$$\vec{R} = \vec{R}_0 + \mathbf{A}(\vec{V} - \vec{V}_0) \tag{5.3.12}$$

where $\vec{R}$ represents the vector of cloud-cleared satellite observations for all retrieval channels, $\vec{R}_0$ represents the vector of radiances computed from the regression first guess for all retrieval channels, $\vec{V}$ and $\vec{V}_0$ represent the solution and regression first guess geophysical parameter vectors, and A, commonly referred to as the kernel matrix, contains the partial derivatives of radiance with respect to each of the individual geophysical parameters and for each of the retrieval channels. A minimum variance solution for $\vec{V}$ is employed in the retrieval process. Minimum variance has been used in the NOAA TOVS operational retrieval system since 1988 (Fleming et. al., 1986; Goldberg et. al., 1986). There are an infinite number of ambient atmospheric states that will satisfy the RTE to within the system noise (i.e. instrumental + cloud-clearing + transmittance). The minimum variance solution uses *a priori* constraints, in the form of a regression estimate and covariance matrix of regression errors, to produce realistic

atmospheric profile solutions minimizing the average squared-error over an ensemble. The iterative matrix form of the solution (Rodgers, 1976):

$$\vec{V}_{n+1} = \vec{V}_0 + (\mathbf{A}_n^T \mathbf{N}^{-1} \mathbf{A}_n + \mathbf{S}^{-1})^{-1} \mathbf{A}_n^T \mathbf{N}^{-1} \left\{ (\vec{R} - \vec{R}_n) - \mathbf{A}_n (\vec{V}_0 - \vec{V}_n) \right\} \quad (5.3.13)$$

where $\vec{V}_{n+1}$ is the n+1 iterative estimate of the retrieved temperature or moisture profile, $\vec{V}_n$ is the n-th iterative estimate of the retrieved profile, $\vec{V}_0$ is the initial guess profile of temperature or water vapor mixing ratio, $\vec{R}$ is the vector of satellite observed radiances, $\vec{R}_n$ is the corresponding vector of radiances computed from the most recent iterative solution, $\mathbf{A}_n$ is the kernel computed from the most recent iterative solution, **N** is the estimated radiance (observation) noise covariance matrix, and **S** is the estimate of the background error covariance matrix between the truth and the retrieval estimate. Superscripts T and -1 denote matrix transpose and matrix inversion, respectively.

Temperature, surface temperature, and water vapor are retrieved separately rather than simultaneously with the temperature retrievals preceding the water vapor retrieval. The temperature profile is retrieved first using channels selected from the 15μm and 4.3μm bands that are relatively unaffected by water vapor. By first improving the temperature retrieval, the subsequent H_2O retrieval will be more accurate because the temperature component of the signal in the water vapor channels will be better accounted for. Both retrieval steps can be iterated, however experiments with simulated data have shown that often the initial guess departure from the truth is in the linear regime such that only one iteration is required.

5.3.6 Expressing the Retrieval Solution in more Computationally Efficient Form

The retrieval solution in equation (5.3.13) can be expressed in a more computationally efficient form using eigenvector methods. Because **S** in equation (5.3.13) is a real symmetric matrix it may be written:

$$\mathbf{S} = \Gamma \Lambda \Gamma^T \quad (5.3.14)$$

where Γ is an [n x n] orthonormal matrix, Λ is an [n x n] diagonal matrix, and superscript T denotes matrix transpose. Substituting equation (5.3.14) into equation (5.3.13) and making use of the properties of eigenvectors it is easy to show that equation (5.3.13) can be written in the following equivalent form,

$$\Delta\vec{V} = \Gamma\left(\Gamma^T\mathbf{A}_n^T\mathbf{N}^{-1}\mathbf{A}_n\Gamma + \Lambda^{-1}\right)^{-1}\Gamma^T\mathbf{A}_n^T\mathbf{N}^{-1}\left\{\Delta\vec{R} - \mathbf{A}_n\left(\vec{V}_0 - \vec{V}_n\right)\right\} \tag{5.3.15}$$

The [**n** x **n**] matrix Γ contains the **n** orthonormal 'eigenvectors' of **S** in it's columns and the diagonal matrix Λ contains the **n** ordered 'eigenvalues' of **S**. More specifically

$$\Lambda = \begin{bmatrix} \lambda_1 & 0 & \cdots & 0 \\ 0 & \lambda_2 & \ddots & \vdots \\ \vdots & \ddots & \ddots & 0 \\ 0 & \cdots & 0 & \lambda_n \end{bmatrix} \quad \text{and} \quad \Gamma = \begin{bmatrix} & & & \\ \gamma_1^1 & \gamma_1^2 & & \gamma_1^n \\ \gamma_2^1 & \gamma_2^2 & \cdots & \gamma_2^n \\ \vdots & \vdots & & \vdots \\ \underbrace{\gamma_n^1}_{\Gamma_1} & \underbrace{\gamma_n^2}_{\Gamma_2} & & \underbrace{\gamma_n^n}_{\Gamma_n} \end{bmatrix} \tag{5.3.16}$$

where $[\Gamma_1, \Gamma_2, ..., \Gamma_n]$ are the **n** eigenvectors of **S** and $[\lambda_1, \lambda_2, ..., \lambda_n]$ are the corresponding eigenvalues.

The dimensions of the matrix to be inverted in equation (5.3.15) is reduced by truncating the matrices of eigenvectors and eigenvalues. If we retain **m** of the **n** eigenvectors (**m** < **n**) then equation (5.3.15) is rewritten:

$$\Delta\vec{V} = \tilde{\Gamma}\left(\tilde{\Gamma}^T\mathbf{A}_n^T\mathbf{N}^{-1}\mathbf{A}_n\tilde{\Gamma} + \overline{\omega}\tilde{\Lambda}^{-1}\right)^{-1}\tilde{\Gamma}^T\mathbf{A}_n^T\mathbf{N}^{-1}\left\{\Delta\vec{R} - \mathbf{A}_n\left(\vec{V}_0 - \vec{V}_n\right)\right\} \tag{5.3.17}$$

where $\overline{\omega}$ is a tuning parameter, and the definition of $\overline{\omega}\tilde{\Lambda}^{-1}$ and $\tilde{\Gamma}$ are as follows:

$$\overline{\omega}\tilde{\Lambda}^{-1} = \begin{bmatrix} \overline{\omega}/\lambda_1 & 0 & 0 & \cdots & 0 \\ 0 & \overline{\omega}/\lambda_2 & 0 & \cdots & 0 \\ 0 & 0 & \overline{\omega}/\lambda_3 & \ddots & \vdots \\ \vdots & \ddots & \ddots & \ddots & 0 \\ 0 & \cdots & 0 & 0 & \overline{\omega}/\lambda_m \end{bmatrix} \quad \text{and} \quad \tilde{\Gamma} = \begin{bmatrix} & & & \\ \gamma_1^1 & \gamma_1^2 & & \gamma_1^m \\ \gamma_2^1 & \gamma_2^2 & \cdots & \gamma_2^m \\ \vdots & \vdots & & \vdots \\ \underbrace{\gamma_n^1}_{\tilde{\Gamma}_1} & \underbrace{\gamma_n^2}_{\tilde{\Gamma}_2} & & \underbrace{\gamma_n^m}_{\tilde{\Gamma}_m} \end{bmatrix} \tag{5.3.18}$$

Notice that the dimension of the matrix to be inverted in equation (5.3.17) is **[m** x **m]** compared to the larger **[n** x **n]** matrix in equation (5.3.15). In addition to reducing the number of floating point operations, truncating the eigenvectors may also filter out unwanted noise in the retrieval process by excluding higher order terms containing spurious information.

Settings for the tuning parameter, γ, and the number of eigenvectors retained, **m**, are different for water vapor and temperature retrievals. Experimentally determined values for ($\overline{\omega}$, **m**) are currently set to (1.5, 15) for temperature, and (60, 15) for water vapor.

5.3.7 Computation of the Kernel matrix

The elements of the $\mathbf{A}_n$ matrix in Equation (5.3.17) are derived for infrared and microwave channels using a quadrature form of equations (4.2.1) and (4.1.2). As discussed, the elements of $\mathbf{A}_n$ are derivatives of radiance (brightness temperature for microwave) with respect to individual geophysical parameters (e.g. 50 mb temperature, 500 mb water vapor mixing ratio, surface temperature) from the most recent iterative solution. We begin by writing equations (4.2.1) and (4.1.2) in quadrature form using the trapezoidal rule of integration. For the IR region the quadrature form of equation (4.2.1) is,

$$R_\nu^c = \varepsilon_\nu B_\nu(T_s)\tau_{\nu s} + \sum_{j=1}^{J} \frac{1}{2}\left(B_\nu(T(p_j)) + B_\nu(T(p_{j-1}))\right)\left\{\tau_\nu(p_{j-1}) - \tau_\nu(p_j)\right\} + \rho_\nu B_\nu(T_{sun})\tau_{\nu s}^2 \cos\theta \tag{5.3.19}$$

where J represents the number of discrete pressure levels of the fast transmittance model, p_j is the pressure at the jth pressure level and all other quantities are as defined in equation (4.2.1). Similarly for the MW region of the spectrum equation (4.1.2) is expressed in equivalent quadrature form,

$$R_\nu^c = \varepsilon_\nu T_s \tau_{\nu s} + \sum_{j=1}^{J} \frac{1}{2}\left(T(p_j) + T(p_{j-1})\right)\left\{\tau_\nu(p_{j-1}) - \tau_\nu(p_j) + (1-\varepsilon_\nu)(\tau_\nu^*(p_j) - \tau_\nu^*(p_{j-1}))\right\} \tag{5.3.20}$$

where $\tau_\nu^*(p_j) = \tau_\nu^2(p_s) / \tau_\nu(p_j)$. Equation (5.3.20) can be simplified by using notation for *effective transmittances*, combining the upwelling and downwelling microwave components of radiance into a single term. The form of the simplified equation is

$$R_\nu^c = T_s \tilde{\tau}_{\nu s} + \sum_{j=1}^{J} \frac{1}{2}\left(T(p_j) + T(p_{j-1})\right)\left\{\tilde{\tau}_\nu(p_{j-1}) - \tilde{\tau}_\nu(p_j)\right\} \tag{5.3.21}$$

where $\tilde{\tau}$ indicates the effective transmittance and is defined,

$$\tilde{\tau}_\nu(p_k) = \left[1 - (1-\varepsilon_\nu)\left(\tau_\nu(p_s) / \tau_\nu(p_k)\right)^2\right] \cdot \tau_\nu(p_k) \tag{5.3.22}$$

Taking the derivative of equations (5.3.19) and (5.3.21), both with respect to temperature and water vapor mixing ratio, gives the elements of $\mathbf{A}_n$.

Making the assumption that transmittance is independent of temperature the temperature elements of $\mathbf{A}_n$ for infrared channels are defined as,

$$A_n^{ij} = \frac{dR_i^c}{dT_j} = \begin{cases} \frac{1}{2}\frac{dB_j}{dT_j}\left\{2 - \tau_j - \tau_{j+1}\right\} & \text{for } j = 1 \\ \frac{1}{2}\frac{dB_j}{dT_j}\left\{\tau_{j-1} - \tau_{j+1}\right\} & \text{for } 1 < j < J \\ \frac{1}{2}\frac{dB_j}{dT_j}\left\{\tau_{j-1} - \tau_j\right\} & \text{for } j = J \\ \varepsilon_s \frac{dB_s}{dT_s}\tau_s & \text{for surface skin term} \end{cases} \tag{5.3.23}$$

where J is the number of atmospheric levels and j = J corresponds to the lowest atmospheric level, τ_s is the atmospheric transmittance from the surface to space, τ_k is the atmospheric transmittance from the jth atmospheric pressure level to space, ε_s is the surface spectral emissivity, and dB/dT_k is the derivative of the Planck function evaluated at channel i and atmospheric temperature T_k. Similarly for the microwave region the definition of the temperature elements of $\mathbf{A}_n$ are as follows,

$$A_n^{ij} = \frac{dR_i^c}{dT_j} = \begin{cases} \frac{1}{2}\left\{2\tilde{\tau}_0 - \tilde{\tau}_j - \tilde{\tau}_{j+1}\right\} & \text{for } j = 1 \\ \frac{1}{2}\left\{\tilde{\tau}_{j-1} - \tilde{\tau}_{j+1}\right\} & \text{for } 1 < j < J \\ \frac{1}{2}\left\{\tilde{\tau}_{j-1} - \tilde{\tau}_j\right\} & \text{for } j = J \\ \tilde{\tau}_s & \text{for surface skin term} \end{cases} \tag{5.3.24}$$

where the effective transmittance, $\tilde{\tau}$, is as defined above.

The water vapor elements of the $\mathbf{A}_n$ matrix for IR channels are defined as follows,

$$A_n^{ij} = \frac{dR_i^c}{d\chi_j} = \left[\varepsilon_s B_s + 2\rho_\upsilon B_{Tsun}\tau_s \cos\theta - \frac{(B_{J-1} + B_J)}{2}\right]\frac{d\tau_s}{d\chi_j} + \sum_{k=1}^{J-1}\frac{(B_{k+1} - B_{k-1})}{2}\frac{d\tau_k}{d\chi_j} \tag{5.3.25}$$

where B_{Tsun} is the Planck function evaluated for channel i at the temperature of the sun, B_k is the Planck function evaluated for channel i at the first guess level temperature T_k, θ is the solar zenith angle, ρ_υ is the surface spectral reflectivity for channel i, χ_k is the initial guess mixing ratio at level k, and all other terms are as defined in equations (5.3.22) and (5.3.23). Assuming an isothermal atmosphere above the uppermost pressure level the definition of the water vapor elements of $\mathbf{A}_n$ in the microwave are as follows,

$$A_n^{ij} = \frac{dR_\upsilon^c}{d\chi_j} = \left[T_s - \frac{1}{2}\left(T_J + T_{J-1}\right)\right]\frac{d\tilde{\tau}_s}{d\chi_j} + T_1 \cdot \frac{d\tilde{\tau}_0}{d\chi_j} + \sum_{k=1}^{J}\frac{1}{2}\left(T_{k+1} - T_{k-1}\right)\frac{d\tilde{\tau}_k}{d\chi_j} \tag{5.3.26}$$

The derivative terms in equation (5.3.26) are evaluated using the definition of effective transmittance from equation (5.3.22),

$$\frac{d\tilde{\tau}_k}{d\chi_j} = \frac{d}{d\chi_j}\left[\tau_k - (1-\varepsilon)\frac{\tau_s^2}{\tau_k}\right] \tag{5.3.27}$$

which after some manipulation reduces to the following form,

$$\frac{d\tilde{\tau}_k}{d\chi_j} = \frac{d\tau_k}{d\chi_j} + (1-\varepsilon)\left[\frac{d\tau_k}{d\chi_j}\cdot\frac{\tau_s}{\tau_k} - 2\cdot\frac{d\tau_s}{d\chi_j}\right]\frac{\tau_s}{\tau_k} \tag{5.3.28}$$

The derivative of transmittance with respect to water vapor is given by:

$$\frac{d\tau_k}{d\chi_j} = \tau_k \frac{d\ell n\tau_k}{d\chi_j} = \tau_k \frac{d\ell n\tau_k}{dq_k}\frac{dq_k}{d\chi_j} \tag{5.3.29}$$

where q_k, the precipitable water from the space to pressure level k, is calculated by:

$$q_k = \tfrac{1}{2g}\sum_{n=1}^{k}(\chi_n + \chi_{n-1})(p_n - p_{n-1}) \tag{5.3.30}$$

the derivative of precipitable water is given by:

$$\frac{dq_k}{d\chi_j} = \begin{cases} (1/2g)\left(p_{j+1} - p_{j-1}\right) & \text{for } j < k \\ (1/2g)\left(p_j - p_{j-1}\right) & \text{for } j = k \\ 0 & \text{for } j > k \end{cases} \tag{5.3.31}$$

and the derivative of the natural log of transmittance with respect to precipitable water is:

$$\tau_k \frac{d\ell n\tau_k}{dq_k} = \tau_k \frac{\ell n(\tau_{k-1}) - \ell n(\tau_k)}{q_{k-1} - q_k} \tag{5.3.32}$$

[Note: $\tau_0 \equiv 1$ in the calculation of the above derivatives.]

5.3.8 The Observation Noise Covariance Matrix N

The observation noise covariance matrix, **N**, is nominally a diagonal matrix whose non-zero elements (the diagonal elements) represent the observation noise. In the case of a clear AMSU field of view the diagonal terms for AIRS is 1/9 the variance of the AIRS instrumental noise for each of the retrieval channels, since all 3 x 3 AIRS footprints within an AMSU footprint are averaged. Thus **N** has the form:

$$\mathbf{N} = \begin{bmatrix} \sigma_1^2 & 0 & \cdots & 0 \\ 0 & \sigma_2^2 & \cdots & 0 \\ \vdots & \vdots & \ddots & 0 \\ 0 & 0 & 0 & \sigma_n^2 \end{bmatrix} \tag{5.3.33}$$

The diagonal values, $[\sigma_1^2, \sigma_2^2, \cdots, \sigma_n^2]$, represent the noise of the **n** retrieval channels, and all off diagonal elements (i.e. all interchannel covariances) are assumed to be zero. Operationally **N** will include the total system noise and may include off diagonal elements. The total system noise for each channel is due to the combined effects of

measurement noise, cloud-clearing extrapolation (which is output from the cloud-clearing algorithm), forward model inaccuracies, and calibration error.

5.3.9 The Thermal and Moisture Covariance Matrix S

The retrieval parameter covariance matrix, denoted by **S** in the previous mathematical description of the physical retrieval, represents the expected error of the background field. As discussed above, a background field is generated from a regression scheme using a large training data base to estimate geophysical quantities from principal components derived from AIRS/AMSU/HSB brightness temperature observations. The same training data is used to estimate the magnitude of expected background errors when the regression coefficients are applied to independent data. The coefficients, matrix **C** from equation (5.3.22), are applied back to the dependent training data as follows:

$$\Delta\tilde{\mathbf{V}} = \mathbf{C}\Delta\mathbf{T} \tag{5.3.34}$$

where $\Delta\tilde{\mathbf{V}}$ is the regression retrieval of the dependent geophysical training data $\Delta\mathbf{V}$ in equation (5.3.7). The covariance matrix, **S**, is then calculated as follows:

$$\mathbf{S} = \frac{1}{m}\mathbf{E}\mathbf{E}^{T}, \text{ where } \mathbf{E} = \Delta\mathbf{V} - \Delta\tilde{\mathbf{V}} \tag{5.3.35}$$

where **S** is an **[n** x **n]** matrix whose diagonal elements represent the expected background variance of each of the predictants, and whose off diagonal elements represent expected interlevel covariances amongst the various predictants.

5.4 Final Product

5.4.1 Introduction

To satisfy the science requirements of NASA's Earth Science Enterprise, a final adjustment is made to the first product based on the difference between calculated and cloud-cleared radiances. It is here that the cloud parameters, and the research products (not described in this document) are calculated.

When solving for a set of geophysical parameters, it is desirable to be able to choose an appropriate set of parameters to solve for and select channels that are both sensitive to those parameters and relatively insensitive to other parameters. In general, channels will be affected by more than one type of parameter. For example, channels with radiances sensitive to the water vapor or ozone distribution are also sensitive to the temperature profile and often to the surface skin temperature. Our approach is to solve sequentially for the surface parameters, temperature profile, water vapor profile, and ozone profile in that order. In this approach, variables already solved for, used in conjunction with first guess variables, are kept fixed when solving for the next set of variables. Table 5.4.1 lists the variables solved for and the number of channels used in each step. The above order is chosen because channels can be selected for a given step that are relatively insensitive to variables to be solved for subsequently.

The iterative solution to the problem contains equations that are of the form of equation (5.3.13). However, the final product methodology solves for updates to coefficients of functions of temperature, moisture, etc., rather than updates to the geophysical parameters themselves. Therefore, the terms in the equation have a very different meaning. For this reason, a different notation is used so as not to confuse the reader. For example, in place of A in the analog of equation (5.3.13), which refers to the derivative of the radiance with respect to changes in a geophysical parameter, the sensitivity of the radiances to changes in the coefficients of the expansion functions, S, is used.

A total of 278 AIRS channels, 15 AMSU A channels, and 4 HSB channels are selected for use in the AIRS/AMSU/HSB retrieval algorithm. Some of the surface parameter sounding channels are also used in the water vapor or temperature profile retrievals. Therefore, the total number of channels is less than the sum of the channels in column 2. Likewise, the water vapor solved for in the ground temperature retrieval is subsequently updated in the water vapor profile retrieval step. The 297 channels are used to solve for 42 variables.

The general AIRS/AMSU/HSB retrieval algorithm does not require any field-of-view to be cloud-free (Susskind *et al.*, 1996). The algorithm used in the final product retrieval consists of the following main steps: (0) Obtain an initial guess for the temperature, moisture, and ozone profiles. (1) Derive a first estimate of the cloud cleared radiances and channel noise covariance matrix. (2) Retrieve surface parameters. If necessary, the first guess and cloud-cleared radiances may be improved at this point and the surface retrieval may be repeated. This loop ends the basic startup procedure. (3) Retrieve temperature profile. (4) Retrieve water vapor profile. (5) Retrieve ozone profile. (6) Produce final cloud cleared radiance estimates. Repeat (2) - (3) starting with updated cloud cleared radiances and water vapor and ozone profile. The general approach to solve for the parameters in steps (2) - (5) is in the form of iterative constrained least squares solutions, one for each set of variables to be solved for. The form of the equations to be solved is identical for each of the four steps. More details about the steps in the final product retrieval algorithms are given below.

Variables	Channels	Frequencies
		Ground Temperature Retrieval
T_S , $\Delta \ell nW$, 8 IR spectral emissivity functions, 3 IR spectral bi-directional reflectance functions, MW spectral emissivities	23 35 6	758 → 1235 cm^{-1} 2170 → 2669 cm^{-1} 23.8–150 GHz
		Temperature Profile Retrieval
14 layer temperature-functions (trapezoids)	103 33 12	651 → 768 cm^{-1} 2228 → 2501 cm^{-1} 50.3 → 57.29 GHz
		Water Vapor Profile Retrieval
8 layer column density functions	69 54	790 → 2650 cm^{-1} 150-183.31 GHz
		Ozone Profile Retrieval
5 layer column density functions	23	1001 → 1069 cm^{-1}

Total: 42 variables 297 channels (AIRS + AMSU)

TABLE 5.4.1. VARIABLES AND CHANNELS

Steps in the AIRS Final Product Algorithm

1. Obtain an initial guess which agrees with AMSU and HSB radiances. This is obtained from the first product physical retrieval, followed by a temperature profile retrieval using AMSU A radiances and AIRS radiances for channels sounding above the clouds, sequentially followed by a water vapor retrieval using HSB radiances.
2. Determine an initial η_k^1 from equations (5.2.30) and (5.2.29), using the initial guess parameters. Allow a maximum of two η's. Also produce the retrieval noise covariance $\mathbf{M}^1$ as described later.
3. Perform a start up surface parameter retrieval using $\hat{R}_i^1$ obtained from equation (5.2.20). All channels used in this step are sensitive to clouds, so there is no need to retrieve cloud height.
4. Produce an improved AMSU temperature profile retrieval, using the retrieved value T_S^1, and radiances in AMSU channels and a set of AIRS stratospheric sounding channels which do not see the clouds.

5. Determine updated η_k^2 taking advantage of the refined parameters. Allow a maximum of three η's. Also determine cloud parameters to decide which channels do not see clouds. This information is used to produce $\hat{R}_i^2$ as well as the retrieval channel noise covariance matrix $\mathbf{M}^2$. This is the end of start up system.

6-9 Use $\hat{R}_i^2$ and $\mathbf{M}^2$ to refine the surface parameters, temperature profile, humidity profile, and ozone profile. These steps give the first pass retrieved parameters.

10. Using the first pass retrieved parameters, determine refined η_k^3, allowing up to 4 values of η and final cloud parameters.

11. Produce the final clear column radiances $\hat{R}_i^3$, which is a product of the system, and M^3.

12. Perform a test AMSU temperature profile retrieval for rejection test.

13. Repeat steps 6-7 using $\hat{R}_i^3$ and $\mathbf{M}^3$ to obtain the final surface and temperature profile products, using the first pass retrieved water vapor and ozone parameters and first guess temperature profile as the initial guess.

14 Apply rejection tests. If solution is not accepted, return the microwave product as the final solution and set an appropriate flag.

5.4.2 General Iterative Least Squares Solution

An iterative approach is used to linearize the radiative transfer equation about the n^{th} iterative parameters X_ℓ^{n+1}. The iterative retrieval process described here is different from the use of different passes in the determination of η. The values of $\hat{R}_i$ used in the iterative retrieval loop are held fixed in a given pass. The $n+1^{th}$ iterative estimate of X_ℓ is expanded according to

$$X_\ell^{n+1} = X_\ell^n + \sum_{j=1}^{J} F_{\ell j}\, \Delta A_j^n = X_\ell^o + \sum_{j=1}^{J} F_{\ell j}\, A_j^n \qquad (5.4.1)$$

where the columns of F represent a set of functions, X_ℓ^o is the initial guess, and A_j^n are corresponding coefficients given by

$$A_j^n = A_j^{n-1} + \Delta A_j^n \qquad (5.4.2)$$

which together with X_ℓ^o determine the solution. A solution is found that attempts to minimize the residuals $\Delta\Theta_i^n$, weighted inversely with respect to expected noise levels, for the channels used to determine A_j. The residual for channel i is defined by

$$\Delta\Theta_i^n = \left(\hat{R}_i - R_i^n\right)\left(\frac{dB}{dT}\right)^{-1}_{\Theta_i^n} \tag{5.4.3}$$

where $\hat{R}_i$ is the reconstructed clear column radiance, R_i^n is the radiance computed from the nth iterative parameters, and Θ_i^n is the brightness temperature computed from the n^{th} iteration parameters. The n^{th} iteration residual for channel i is attributed to errors in the coefficients, δA_j^n, and to noise effects, i.e.,

$$\Delta\Theta_i^n = \sum_j S_{ij}^n \, \delta A_j^n + \tilde{\Theta}_i \tag{5.4.4}$$

where S_{ij} is an element of the sensitivity matrix or Jacobian given by

$$S_{ij}^n = \frac{\partial R_i^n}{\partial A_j^n}\left(\frac{dB}{dT}\right)^{-1}_{\Theta_i^n} \tag{5.4.5}$$

and the noise factor $\tilde{\Theta}_i$ for a given case has two parts: errors in observed cloud-cleared radiances $\delta\hat{\Theta}_i$, which are affected by instrumental noise and cloud clearing errors, and computational noise $\delta\Theta_i^c$.

In simulations, a perfect knowledge of physics is assumed, i.e., all the variables are known exactly, the exact noise free radiances are computed. Nevertheless, the transmittances depend on the variables to be solved for. Therefore, computational noise exists. Computational noise, arising from errors such as too low (high) an estimate of atmospheric water vapor, produce noise that is correlated between channels. Instrumental noise is uncorrelated from channel-to-channel but cloud-clearing errors are correlated from channel-to-channel. Each retrieval step uses an appropriate noise covariance matrix

$$M_{ij} = (\hat{M}_{ij} + \tilde{M}_{ij})\left(\frac{dB_i}{dT}\right)^{-1}_{\Theta_i}\left(\frac{dB_j}{dT}\right)^{-1}_{\Theta_j} \tag{5.4.6}$$

where $\hat{\mathbf{M}}$ is defined in Equation (5.2.30) and $\tilde{\mathbf{M}}$ is discussed later, with values which depend on the pass. Writing $\mathbf{W}$ as $\mathbf{M^{-1}}$ for simplicity.

A general form of the solution to this problem is given by

$$\Delta A^n = \left[\mathbf{S'}^n\,\mathbf{W}\,\mathbf{S}^n + \mathbf{H}^n\right]^{-1}\mathbf{S'}^n\,\mathbf{W}\Delta\Theta^n = \overline{\mathbf{M}}^n\Delta\Theta^n \tag{5.4.7}$$

where ΔA^n and $\Delta\Theta^n$ are column vectors of the updates to the coefficients and of the residuals, respectively, and $\mathbf{H}^n$ is a stabilizing or damping matrix.

Hanel *et al.* (1992) and Rodgers (1976) have reviewed several methods of constraining the ill-conditioned inverse problem. In the minimum variance approach (Rodgers, 1976), H is taken to be the inverse of the *a priori* error covariance. If the statistics of both the measurement and *a priori* are Gaussian, the maximum likelihood solution is obtained. If the *a priori* covariance is taken to be $H = \gamma I$, the maximum entropy solution is obtained. Other forms of H include the first or second derivative formulations (Twomey, 1963) that force a smoothness constraint on the solution. The solution can also be constrained by the relaxation method (Chahine, 1968) and by the Backus and Gilbert (1970) method.

The minimum variance and maximum likelihood solutions are often considered to be "optimal." However, if the *a priori* error covariance is not known or estimated incorrectly, the solution is sub-optimal. If the *a priori* errors are underestimated, the solution is overconstrained. Potentially, this creates biases in the retrievals. The biases mask small trends in the retrieved data that scientifically important. The approach described here attempts to keep the effects of instrument noise at a tolerable level without assumptions regarding the *a priori* data error covariance.

5.4.3 Transformation of Variables

As a consequence of stabilizing the potentially ill-conditioned solution, the addition of **H** also has the effect of damping the information content (reducing ΔA for all modes). The variables are transformed to apply a constraint such that the well-determined components of the variables are solved for without appreciable damping. If a different set of functions are chosen which are linear combinations of original functions, i.e.,

$$\mathbf{G} = \mathbf{FU} \tag{5.4.8}$$

where **U** is a unitary transformation ($\mathbf{UU}' = 1$), and expand the solution in the same way as in Eq. 5.4.1 with unknowns ΔB^n, this obtains the matrix form

$$\mathbf{X}^{n+1} = \mathbf{X}^n + \mathbf{G}\Delta\mathbf{B}^n = \mathbf{X}^n + \mathbf{FU}\Delta\mathbf{B}^n = \mathbf{X}^n + \mathbf{F}\Delta\mathbf{A}^n \tag{5.4.9}$$

The objective is to find a transformation matrix U with desirable properties. In the new basis set, the transformed Jacobian is given by

$$T^n = \frac{\partial R}{\partial B^n}\left(\frac{dB}{dT}\right)_\Theta^{-1} = \mathbf{S}^n\mathbf{U} \tag{5.4.10}$$

The constrained solution, as given by Eq. 5.4.7, in terms of this new set of functions is given by

$$\Delta\mathbf{B}^n = \left(\mathbf{T}'^n\,\mathbf{W}\,\mathbf{T}^n + \mathbf{H}\right)^{-1}\mathbf{T}'^n\,\mathbf{W}\left(\Delta\Theta^n - \delta\Theta^{n-1}\right) = \mathbf{U}'\Delta\mathbf{A}^n \tag{5.4.11}$$

The term $\delta\Theta^{n-1}$ is an iterative background correction term that is zero in the first iteration (it is discussed further below). $\mathbf{U}^n$ is selected such that $\mathbf{T}'^n\,\mathbf{W}^n\,\mathbf{T}^n = \mathbf{U}'\,\mathbf{S}'\,\mathbf{W}\,\mathbf{SU}$ is diagonal with real non-negative eigenvalues λ_j^n. The inverse of each eigenvalue is the variance in that eigenmode. The total variance is the trace of the $(\mathbf{S}'\mathbf{WS})^{-1}$ or, equivalently, the trace of $(\mathbf{U}'\mathbf{S}'\mathbf{WSU})^{-1}$. The unconstrained solution (**H**=0), with no background correction $\left(\delta\Theta^{n-1} = 0\right)$, is then given by

$$\Delta B_j^n(0) = \left(\lambda_j^n\right)^{-1} \sum_{k,i} T_{kj}^n \, W_{k,i} \, \Delta\Theta_i^n = \left(\lambda^n\right)_j^{-1} \overline{m}_j^n \, \Delta\Theta^n \tag{5.4.12}$$

where m_j^n is the vector corresponding to the j^{th} row of $\mathbf{T'W}$. In general, the ill-conditioned cases arise from those components of **G** having low information content and small eigenvalues (high variance), indicating that those components are not well determined from the observations alone and need damping. Components with large eigenvalues are quite well determined and require little or no damping to achieve a stable solution. If **H** is chosen to be diagonal with values $\Delta\lambda$, the constrained solution with no background correction term is given by

$$\Delta B_j^n \left(\Delta\lambda^n\right) = \left(\lambda_j^n + \Delta\lambda_j^n\right)^{-1} \overline{m}_j^n \, \Delta\Theta^n \tag{5.4.13}$$

The coefficients $\Delta B_j^n \left(\Delta\lambda_j^n\right)$ are damped from the unconstrained coefficients ΔB_j^n (0) by

$$\Delta B_j^n \left(\Delta\lambda_j^n\right) = \frac{\lambda_j^n}{\lambda_j^n + \Delta\lambda_j^n} \Delta B_j^n (0) = \Phi_j^n \, \Delta B_j^n (0) \tag{5.4.14}$$

where Φ_j can be thought of as a filter or damping function. This formulation is the same as the maximum entropy solution, applied in transformed space, if $\Delta\lambda$ is set equal to a constant. However, instead of using a single constant for every $\Delta\lambda_j^n$, a different value is computed for each eigenfunction. For well-determined eigenmodes, $\Delta\lambda$ is set equal to 0, giving no weight to the *a priori*. For modes that are not well determined by the measurements, $\Delta\lambda$ is determined in such a way as to limit the propagation of instrument noise to a pre-specified amount. The determination of $\Delta\lambda_j^n$ is discussed in detail in the next section.

5.4.4 Application of a Constraint

The residual $\Delta\Theta_i^n$ can be thought of as having both a signal and a noise component, i.e.,

$$\Delta\Theta_i^n = \Delta\Theta_i^{signal} + \tilde{\Theta}_i \tag{5.4.15}$$

The component of ΔB_j that arises from the propagation of channel noise, $\tilde{\Theta}_i$, is given by

$$\delta\tilde{B}_j^n\left(\lambda_j^n\right) = \left(\lambda_j^n + \Delta\lambda_j^n\right)^{-1}\left[\mathbf{T}'^n\,\mathbf{W}\right]\tilde{\Theta}\,. \tag{5.4.16}$$

A statistical estimate of $\delta\tilde{B}_j^n$ over an ensemble of profiles can be obtained by

$$\delta\tilde{B}_j^n = \left[\delta\tilde{B}^n\,\delta\tilde{B}^{n\,\prime}\right]_{jj}^{1/2} = \left(\lambda_j^n + \Delta\lambda_j^n\right)^{-1}\left[\mathbf{T}'\,\mathbf{W}\,\tilde{\Theta}\,\tilde{\Theta}'\,\mathbf{W}'\,\mathbf{T}\right]_{jj}^{1/2} = \frac{\left(\lambda_j^n\right)^{1/2}}{\lambda_j^n + \Delta\lambda_j^n} \tag{5.4.17}$$

because $\tilde{\Theta}\tilde{\Theta}' = \mathbf{M} = \mathbf{W}^{-1}$. This formulation of $\delta\tilde{\Delta}$ is similar to that given by Rodgers (1990). If $\Delta\lambda_j^n$ were zero, $\delta\tilde{B}_j^n$ becomes large if λ_j^n is small. $\Delta\lambda_j^n$ is selected such that $\delta\tilde{B}_j^n$ is less than or equal to a threshold value. If $\delta\tilde{B}_j^n$ is allowed to be no more than δB_{MAX}, then $\Delta\lambda_j$ is set to zero if $\lambda_j \geq \delta B_{MAX}^{-2}$ and $\Delta\lambda_j = \dfrac{\lambda_j^{1/2} - \delta B_{MAX}\,\lambda_j}{\delta B_{MAX}}$ otherwise. For example, if $\delta B_{MAX} = 0.5$, $\Delta\lambda_j = 0$ for $\lambda_j \geq 4$, and if $\delta B_{MAX} = 1$, $\Delta\lambda_j = 0$ for $\lambda_j \geq 1$, corresponding to less damping. Constraints are only applied to those eigenfunctions with lower information content than the critical value corresponding to δB_{MAX}. The value of δB_{MAX} has been determined empirically for each type of retrieval. The AMSU temperature retrieval step behaves best with $\Delta B_{MAX} = 1.0$, the AIRS surface temperature retrieval step with a value of $\Delta B_{MAX} = 0.35$, the AIRS

temperature and moisture profile retrieval steps with $\Delta B_{MAX} = 1.2$ and 1.0, respectively, and the ozone profile retrieval with $\Delta B_{MAX} = 4$. The computation of all matrix elements shown above, including λ and $\Delta\lambda$, is done in each iteration.

5.4.5 Formulation of the background term

The need for an iterative process arises because the radiative transfer equation is not linear. In every iteration, Θ_i^n, $\mathbf{S}^n$, $\mathbf{U}^n$ and λ^n are each recomputed. If the solutions were completely linear, and no damping is applied then

$$\Delta\Theta^{n+1}(0) \cong \Delta\Theta^n - \mathbf{S}^n\,\mathbf{U}^n\,\Delta\mathbf{B}^n(0) \tag{5.4.18}$$

and $\Delta\mathbf{B}^{n+1}(0)$ is zero because $\Delta\mathbf{B}^n(0)$ already minimizes the residuals.

Eq. 5.4.18 is not exact, because both $\Theta^{n+1}(0)$ is not given exactly by $\Theta^n + \mathbf{S}^n\mathbf{U}^n\Delta\mathbf{B}^n$, and $\Delta B_j^n \neq \Delta B_j^n(0)$. As a result of applying ΔB_j^n rather than $\Delta B_j^n(0)$, which minimizes the radiance residuals

$$\Delta\Theta^{n+1} \approx \Delta\Theta^{n+1}(0) + \mathbf{S}^n\mathbf{U}^n\left[\Delta\mathbf{B}^n(0) - \Delta\mathbf{B}^n\right] = \Delta\Theta^{n+1}(0) + \delta\Theta^n \tag{5.4.19}$$

In Eq. 5.4.19, $\Delta\Theta^{n+1}(0)$ represents the portion of $\Delta\Theta^{n+1}$ that is due to effects of non-linearity on the solution, while $\delta\Theta^n$ represents the residual portion of $\Delta\Theta^{n+1}$ due to the effects of damping in iteration n. The second term is zero for undamped modes and increases in significance with increased damping. This term is also zero for all modes in the first iteration. It is desirable to include the effects of non-linearity in the iterative procedure used in the determination of $\Delta\mathbf{B}^n$. Therefore, the background term to be used in Eq. (5.4.11) is given by

$$\delta\Theta^n = \mathbf{S}^n\,\mathbf{U}^n\left[\Delta\mathbf{B}^n(0) - \Delta\mathbf{B}^n\right]$$

and we solve for ΔB_j^{n+1} according to

$$\Delta B_j^{n+1} = \left(\lambda_j^{n+1} + \Delta\lambda_j^{n+1}\right)^{-1} \mathbf{U}'^{n+1}\,\mathbf{S}'^{n+1}\,\mathbf{W}^{n+1}\left[\Delta\Theta^{n+1} - \delta\Theta^{n}\right]$$
$$= \Phi^{n+1}\,\Delta B_j^{n+1}(0) - \left(\lambda_j^{n+1} + \Delta\lambda_j^{n+1}\right)^{-1} \tag{5.4.20}$$
$$\left[\mathbf{U}'^{n+1}\,\mathbf{S}'^{n+1}\,\mathbf{W}^{n+1}\,\mathbf{S}^{n}\mathbf{U}^{n}\left(\Delta B_j^{n}(0) - \Delta B_j^{n}\right)\right]$$

where ΔB_j^n is the value of ΔB_j which applied in iteration n. Inclusion of the background term in Eq. (5.4.20) ensures second order convergence along the lines discussed by Rodgers (1976) with regard to treatment of the *a priori* term.

5.4.6 Convergence Criteria

Solving Eq. 5.4.20 finds solutions to the radiative transfer equations which minimize weighted residuals of observed and computed brightness temperatures, corrected for the background term. To test convergence of the solution, the weighted residual is monitored

$$\mathbf{R} = \left[\left(\Delta\Theta - \delta\Theta\right)' \mathbf{V}'\,\mathbf{V}\left(\Delta\Theta - \delta\Theta\right)\right]^{1/2} \tag{5.4.21}$$

where the weight matrix **V** accounts for noise effects on the channel residuals, as well as the relative information content of the channels with regard to the variables being solved for. For example, if a channel (or linear combination of channels) carries little information content in terms of signal-to-noise, it is given little weight in the estimation of the residual in Eq. (5.4.21). An appropriate choice of **V**, expressing the information content of the channels is

$$\mathbf{V} = \left(\lambda_j + \Delta\lambda_j\right)^{-1}\left(\mathbf{T}'\,\mathbf{W}\right) \tag{5.4.22}$$

in which case we obtain

$$\mathbf{R} = \left[\Delta\mathbf{B}'\,\Delta\mathbf{B}\right]^{1/2} \tag{5.4.23}$$

As shown in Eq (5.4.23), a reasonable way to determine if the solution has converged, in terms of weighted residuals, is to see if the solution converges in terms of the iterative changes in the solution itself. Initially, $\Delta B_j = 0$ if $\Phi_j^1 < 0.05$, that is,

coefficients of very heavily damped components with little information content are given no weight. The solution is said to have converged when the RMS value of ΔB_j^n is less than 10% of the RMS value of $\delta\tilde{B}^n$ for all components not set equal to zero. The iterative procedure is also terminated if the RMS value of ΔB_j^n is not less than 75% of ΔB_j^{n-1} for the non-zero components. This indicates the solution is not converging rapidly enough and is responding primarily to unmodeled noise. The iterative procedure, which usually converges in 3 iterations, is carried out analogously for all retrieval steps.

5.4.7 The retrieval noise covariance matrix

The retrieval noise covariance matrix **M** used in Eq. (5.4.11) (writing $\mathbf{W} \equiv \mathbf{M}^{-1}$ for simplicity) is given by a sum of two terms

$$M_{ij} = (\hat{M}_{ij} + \tilde{M}_{ij})\left(\frac{dB_i}{dT}\right)_{\Theta_i}^{-1}\left(\frac{dB_j}{dT}\right)_{\Theta_j}^{-1} \tag{5.4.24}$$

where $\hat{\mathbf{M}}$ represents the error covariance in the reconstructed cloud-cleared radiances and $\tilde{\mathbf{M}}$ represents the error covariance in the radiances computed from the estimated profile, as a result of errors in parameters assumed known (being held fixed) in a retrieval step. $\hat{\mathbf{M}}$ is given in Equation (5.2.35).

The computational noise covariance matrix $\tilde{\mathbf{M}}$ is designed to account for errors in the computed cloud-cleared radiance, R_i^n, resulting from errors in the geophysical parameters used in the retrieval step. It is assumed that these errors arise primarily from errors in variables X_j, assumed to be known and held fixed in the retrieval step. $\tilde{\mathbf{M}}$ is modeled according to

$$\tilde{M}_{ii} = \sum_j \left[\frac{\partial R_i}{\partial X_j}\delta X_j^n\right]^2 + (0.1^2)\left(\frac{dB_i}{dT}\right)_{\Theta_i}^2 \tag{5.4.25}$$

and

$$\tilde{M}_{ii'} = \sum_j \frac{\partial R_i}{\partial X_j} \frac{\partial R_{i'}}{\partial X_j} \delta X_j^{n\,2} \tag{5.4.26}$$

where $\frac{\partial R_i}{\partial X_j}$ represents the derivative of R_i^n with respect to parameter X_j and δX_j^n is the estimated uncertainty in parameter X_j in iteration n. The parameters used for X_j in modeling $\tilde{\mathbf{M}}$ represent uncertainties in surface skin temperature, surface emissivity and surface reflectance, as well shifts in the temperature profile, and multiplication of the water vapor and ozone profiles by functions of height. The derivatives $\frac{\partial R_i}{\partial X_j}$ are computed empirically. The term 0.1 in Eq. (5.4.25) is taken to represent additional unmodeled errors. Appropriate functions $\delta X^n(P)$ are computed for each pass m in a manner to be described below.

5.4.8 Variable and Channel Selection

5.4.8.1 Surface Parameter Retrieval

Channel radiances depend on several unknown surface parameters: the surface skin temperature (T_s); the spectral emissivity, $\varepsilon(\nu)$, and bi-directional reflectance $\rho(\nu)$; and the microwave spectral emissivity (ε_m). The retrieval uses 88 infrared window channels and 6 microwave window channels. Inclusion of the microwave window channels stabilizes the surface parameter retrieval and also provides one piece of information about the microwave spectral emissivity.

In the surface parameter retrieval, w infrared window channels are selected from both long- and short-wave infrared window regions generally avoiding even weak absorption lines. For window channels, the transmittance at the surface, $\tau(p_s)$, is generally close to unity. Although the opacity of infrared window channels is small, there is absorption and emission due to the water vapor continuum and the nitrogen continuum, both absorbing primarily in the lowest portions of the atmosphere. Therefore, the radiance in window regions depends not only on T_s, $\varepsilon(\nu)$, and $\rho'(\nu)$, but also on the temperature and moisture in the boundary layer. The radiances of window channels do not depend appreciably on temperature and moisture above the boundary layer. To account for the additional dependencies in the surface parameter retrieval, two additional variables are solved for by scaling the total precipitable water ($\Delta\ell n\ W$) and shifting the

air temperature (ΔT_{AIR}). A few channels centered on weak water vapor absorption lines are included to help account for these additional variables that are subsequently modified in the temperature and moisture retrievals. These weak water vapor lines are in the 3.7 μm window and are sensitive to water vapor absorption as well as reflected solar radiation. The reflected solar radiation causes the surface to appear hotter than in other window regions not affected by reflected solar radiation. Therefore, in the short wavelength window, the contrast between the radiance leaving the surface and that emitted by the boundary layer is enhanced. This effect, coupled with the increased path length of the solar radiation, makes channels on weak water vapor lines in this window very sensitive to water vapor in the boundary layer. Several of the channels in the surface parameter retrieval are also used later in the moisture profile retrieval. Currently, no attempt is made to shift the temperature profile in any pass because the input temperature profile agrees with the AMSU radiances and is assumed to be accurate enough. The water vapor profile is scaled in the second pass surface parameter retrieval because a water vapor profile is retrieved using AIRS infrared channels in the first pass.

When scaling the water vapor, profile, a total of fourteen variables are solved for in the surface parameter retrieval for daytime cases (eleven for nighttime cases). The perturbation functions include a perturbation to T_s, a perturbation to each of 8 infrared spectral emissivity functions, 3 spectral bi-directional reflectance functions, and a scaling of the water vapor profile, and a piece of information about the microwave spectral emissivity. The values of the perturbations are selected to give comparable values of the **S** matrix for a typical case. If all perturbation functions F_j were half as large, S_{ij} would be half as large for each mode, and the solution vector ΔA_j would be twice as large. The perturbations are large enough to produce significant **S** matrix elements, but not so large as to produce an appreciable non-linear response.

The Jacobian or sensitivity matrix $\mathbf{S}^n$ is computed every iteration. The partial derivative of channel radiance with respect to the coefficients of each of the above functions are computed empirically as follows: (1) Compute the i^{th} channel radiance using the n^{th} iteration parameters (i.e., T_S^n , $\varepsilon^n(\nu)$, $q^n(P)$, etc.) (2) Compute the i^{th}

channel transmittance (if necessary) and radiance using the n^{th} iteration parameters but setting the coefficient (ΔA_j) of perturbation function F_j to unity. (3) The sensitivity S_{ij}, related to the change in channel radiance per unit change in coefficient ΔA_j, is given by the difference in radiances computed in steps (1) and (2), divided by $(dB/dT)_{\Theta_i^n}$. The sensitivity or partial derivative of radiance with respect to surface temperature, spectral emissivity, and surface bi-directional reflectance can be computed theoretically by differentiating the clear column radiative transfer equation because the transmittance functions do not depend on these parameters.

After the sensitivity matrix is computed, the inversion procedure described earlier proceeds. In the surface temperature retrieval, modeled channel computational noise is not included in the noise covariance matrix, but includes only an estimate of 0.1K for unmodeled computational noise from other sources in Equation (5.4.22). The retrieved values of T_s , $\varepsilon(\nu)$, and $\rho(\nu)$ are held constant and used in the subsequent iterative steps for temperature, moisture, and ozone profile retrievals. The shifted water vapor profile are held fixed in the transmittance and radiative transfer calculations for the temperature profile retrieval and used as the first guess in the water vapor retrieval.

5.4.8.2 Temperature Profile Retrieval

The temperature profile retrieval problem is set up and solved in a manner completely analogous to the surface parameter retrieval. The solution for the retrieved temperature profile is written in the form

$$T^n(P_\ell) = T^o(P_\ell) + \sum_{j=1}^{J} F_j(P_\ell)\, A_j^n = T^o(P_\ell) + \mathbf{FA} \qquad (5.4.27)$$

where ℓ ranges over the number of levels used to compute channel transmittances and radiances, and j ranges over the number of functions that are solved for, currently set to 14. The functions in the surface parameter retrieval are taken as discrete changes in different surface or atmospheric parameters. Following the approach of the surface parameter retrieval, the functions F_j are selected as localized functions of pressure,

corresponding to changes in temperature primarily in a layer from P_j to P_{j-1}. Use of localized functions is convenient for computing the **S** matrix and makes the problem more nearly linear. The methodology discussed previously does not require the functions to be orthogonal. In order for the solution to be continuous, the functions chosen are trapezoids, with a value of 0.5K between P_j and P_{j-1} and falling linearly in log P to 0K at P_{j+1} and P_{j-2}. The highest and lowest functions in the atmosphere are special cases, with values of 1K at the upper or lower limit of the atmosphere (1 mb or the surface), 0.5K at the adjacent pressure, and followed by 0K at the next pressure level.

The Jacobian matrix is computed exactly as in the surface parameter retrieval. In any iteration, transmittances and radiances are computed for the temperature sounding channels using $T^n(P)$ and $T^n(P) + F_j(P)$, where $F_j(P)$ is one of the trapezoids, and the Jacobian is obtained empirically according to

$$S_{ij}^n = \left[R_i\left(T^n(P) + F_j(P)\right) - R_i\left(T^n(P)\right)\right]\left(\frac{dB}{dT}\right)_{\Theta_i}^{-1}. \qquad (5.4.28)$$

It can be shown that for an opaque temperature sounding channel, a shift of the entire atmospheric temperature profile by 1K will cause roughly a 1K change in brightness temperature (Susskind *et al.*, 1984). Moreover, a localized change of 1K in an atmospheric layer containing the non-zero part of the channel's weighting function likewise result in a 1 K change in brightness temperature. This brightness temperature change decreases as the layer becomes thinner than the weighting function. To insure sensitivity of at least one sounding channel to changes in the layer (or trapezoid) temperatures, layers are selected to be sufficiently coarse as to have an element of the **S** matrix of at least 0.2 for the layer. While the Jacobian is profile dependent, the layer structure used to define the trapezoid functions is held fixed for all soundings. They are selected so as to be neither too thin, resulting in lack of sensitivity, nor too coarse, resulting in lack of resolution. The pressure boundaries for the 14 functions used are shown in Table 5.4.2. According to Equation (5.4.27), the only structure in the solution with finer spacing than these boundary levels must come from the initial guess. In fact, the transforming and damping functions, as discussed earlier, further decrease the ability

of the solution to discern fine structure not contained in the information content matrix **S'WS**. This damping is profile dependent.

In the first pass temperature profile retrieval, channels are selected which are relatively insensitive to the ozone and water vapor distributions as these variables have not been solved for, except for an estimate of the column water vapor content obtained in the surface temperature retrieval step. In addition, temperature-sounding channels are selected between absorption lines to optimize the channel weighting functions (Kaplan *et al.* 1977). Along the lines of Kaplan *et al.* (1977) and outlined in Table 4.3.1, the retrieval uses 96 channels in the 15 μm CO_2 band, including the Q-branch near 666 cm^{-1} to sound the mid to upper stratosphere; channels in between CO_2 absorption lines and near the 720 cm^{-1} and 740 cm^{-1} Q-branches to sound through the upper troposphere; and 33 channels in the CO_2 4.3 μm band P and R branches, primarily in the vicinity near 2380 cm^{-1}, to sound the mid- to lower troposphere. The noisiest spectral region is near 15 μm. For this reason, many of the 15 μm channels represent spectral intervals sampled twice per channel width. This adds little information about the vertical structure but increases signal-to-noise. There are 12 AMSU channels included (3-14 from Table 2.3) in the temperature profile retrieval.

Unlike Kaplan *et al.* (1977), 7 temperature sounding channels are included, which lie between absorption lines in the 15 μm CO_2 band, that are sensitive to the mid-lower tropospheric temperature profile. The inclusion of these channels does not appreciably affect sounding accuracy under clear sky conditions but are significant under cloudy daytime conditions. This somewhat compensates for the increase in effective noise levels of the 4.3 μm tropospheric sounding channels during sunlight conditions. The selection of these channels avoids spectral regions near water vapor lines of appreciable strength. The channel radiances of the mid-lower tropospheric temperature sounding 15 μm channels are still affected by water vapor due to the wings of nearby water vapor lines as well as the water vapor continuum. As described previously, our sounding methodology involves two temperature profile retrieval steps, one (first pass) before the water vapor retrieval, and the other (final pass) subsequent to it. In the final pass, a number of additional channels in the water vapor absorption band are included which produce sharp

temperature weighting functions. Even though the water vapor retrieval has been performed, these channels are still treated as "noisy" in the channel noise covariance matrix to the extent that the predicted uncertainty in water vapor distribution produces uncertainty in the computed radiances.

Errors in the estimate of the water vapor profile used to compute the radiances, produces errors in the computed brightness temperature for a given channel, as well as correlated errors in other temperature sounding channels sensitive to water vapor absorption. These errors are accounted for in the noise covariance matrix $\tilde{\mathbf{M}}$.

The effect of errors in the estimated water vapor profile on computed radiances, as well as radiance errors due to errors in ozone profile and surface parameters, are taken into account in the computational noise covariance matrix (Equations 5.4.25, 5.4.26). The

Temperature retrieval	Moisture retrieval	Ozone retrieval
0.016	0.016	0.016
0.975	170.1	20.92
2.701	260.0	51.53
5.878	300.0	71.54
11.00	343.6	103.0
18.58	407.5	142.4
51.53	496.6	300.0
89.52	596.3	surface
142.4	706.6	
190.3	857.8	
314.1	surface	
478.0		
661.2		
827.4		
surface		

Table 5.4.2. Trapezoid or Layer Endpoints

noise due to errors in the ozone profile is computed analogously to that for water vapor.

Incorporation of these terms into the noise covariance matrix has the effect of making channels sensitive to water vapor absorption, ozone absorption and/or the surface temperature appear noisier. It should be noted that in general, the mid-lower tropospheric sounding 15 μm channels will be "noisier" for humid cases than for very dry ones, where uncertainty in water vapor profile will have a smaller effect on the 15 μm radiances. Conversely, 4.3 μm channels are "noisier" during the day than at night.

The contributions to the noise covariance matrix due to errors in estimated total precipitable water and surface skin temperature are included for all temperature sounding channels. Neither is included in the ground temperature retrieval because both variables are being solved for. The estimated error in surface temperature is included in the noise covariance matrix in the subsequent steps of water vapor profile retrieval and ozone profile retrieval, and the estimated error in water vapor profile is also included in the ozone profile retrieval, but not in the water vapor retrieval.

The retrieval step described above is done after the AMSU temperature profile retrieval step has been completed. That AMSU retrieval step is analogous, but uses only AMSU channels and stratospheric AIRS temperature sounding channels, and solves for one piece of information about the microwave spectral emissivity as well as coefficients of the 14 temperature perturbation functions.

5.4.8.3 Water Vapor Profile Retrieval

Unlike the surface parameter and temperature profile retrievals, the water vapor profile retrieval problem is highly non-linear. A change in water vapor abundance in a given level affects the transmittance in that layer as well as the atmospheric emission and absorption at all lower levels in a complex manner. Nevertheless, the problem is solved in a completely analogous manner. In the surface parameter retrieval, the entire water vapor profile (up to 50 mb) is multiplied by a constant unknown factor. Following this form, the solution for the retrieved moisture profile is expressed as

$$q^n(P_\ell) = q^0(P_\ell)\left[1 + \sum_{j=1}^{J} F_j(P_\ell)\, A_j^n\right], \qquad (5.4.29)$$

where ℓ ranges over the 64 levels used to compute transmittances and radiances, and j ranges over J solution functions. The functions $F_j(P_\ell)$ are expressed as trapezoids with a value of 0.05 in coarse atmospheric layers, in a manner analogous to that described above for the temperature profile retrieval. The endpoints of the 10 trapezoids used in the moisture profile retrieval are included in Table 5.4.2. The highest trapezoid has a value of 0.05 at 170.1 mb and 260 mb and 0 at .016 mb and 300 mb. The lowest function is comprised of two straight lines, with a value at the surface and 857.8 mb of 0.05, and a value of 0 at 706.6 mb.

In the moisture retrieval, we include channels between absorption lines in the 6.3 μm water vapor band that are sensitive to humidity throughout the troposphere. These channels provide sharper weighting functions (more localized absorption) than centers of strong lines and make the problem more linear. In addition, some channels are used on the peaks of the strongest absorption features in the 6.7 μm band, which are sensitive to stratospheric water vapor. Channels are also included on and off weak water vapor absorption lines in both the 11 μm and 8 μm windows, sensitive to the water vapor continuum which improves the sounding capability for lower tropospheric humidity. Channels in the 3.7 μm window provide improved sensitivity to low level moisture during the day. The **S** matrix is computed empirically exactly as in the temperature profile retrieval. The parameters determined from the surface and temperature profile retrievals are kept fixed in the calculations.

In constructing the noise covariance matrix, terms for uncertainties in ground temperature are included, as in the temperature profile retrieval, as well as a term shifting the entire temperature profile, as done in the noise covariance matrix used in the determination of η (Equation 5.2.15).

5.4.8.4 Ozone Profile Retrieval

The solution for the ozone profile retrieval has the same form as that for the moisture retrieval. The ozone retrieval uses 7 trapezoid functions with values of 0.05, as in the water vapor retrieval. The end points of the trapezoids are included in Table 5.4.2. The same steps outlined in the previous section are used to compute the Jacobian. It is critical

to solve for water vapor before ozone because ozone channels are sensitive to absorption by boundary layer water vapor. There are 23 channels in the 9.6 μm ozone band selected for the ozone retrieval. Uncertainties in surface parameters, temperature profile, and water vapor profile are included in the ozone noise covariance matrix.

5.4.8.5 Retrieval of Cloud Properties

The observed radiance for the i^{th} channel, $\overline{R}_i$, in a scene with j cloud types is given by

$$\overline{R}_i = (1 - \sum_j \alpha_j) R_{i,CLR} + \sum_j \alpha_j R_{i,CLD,j} \tag{5.4.30}$$

where α_j is the fraction of the scene (in a nadir view) covered by cloud type j, $R_{i,CLR}$ is the clear-column radiance for channel i (i.e., the radiance emerging from the clear portion of the scene), and $R_{i,CLD,j}$ is the i^{th} channel radiance emerging from the cloudy portion of the scene covered by cloud type j (Chahine, 1982).

The computation of $R_{i,CLD,j}$ for a given scene is complex due to the detailed spectral absorption and reflection properties of clouds, cloud morphology within the field-of-view, and geometric shadowing factors. Assuming plane parallel cloud formations and nadir viewing, $R_{i,CLD,j}$ is expressed as

$$R_{i,CLD,j} = \tau_{ic_j} R_i(p_{c_j}) \tau_i(p_{c_j}) + \varepsilon_{ic_j} B_i(T_{c_j}) \tau_i(p_{c_j}) + \int_{p_{c_j}}^{0} B_i[T(p)] \left(\frac{d\tau_i}{d\ell np} \right) d\ell np$$
$$+ \rho'_{ic_j} H_i \tau'_i(p_{c_j}) \cos\theta_o \tag{5.4.31}$$

where $R_i(p_{c_j})$ is the upwelling radiance at cloud top pressure p_{c_j}, and τ_{ic_j} and ε_{ic_j} are respectively the transmissivity and emissivity of cloud type j at channel frequency ν_i, $B_i(T_{c_j})$ is the Planck function evaluated at channel frequency ν_i and cloud top temperature T_{c_j}, ρ'_{ic_j} is the cloud bi-directional reflectance of solar radiation

incoming at solar zenith angle θ_o and outgoing in the direction of the satellite, $\tau_i'(p_{c_j})$ is the two path atmospheric transmittance from the top of the atmosphere to the cloud top pressure p_{c_j}, and H_i is the solar irradiance. In Eq. (5.4.32), the first term represents upwelling radiation from below the cloud that passes through the cloud. The second term represents radiation emitted by the cloud that is transmitted by the atmosphere to the satellite. The third term represents that portion of the radiation absorbed and emitted by the atmosphere above the cloud, and the fourth term represents solar radiation reflected by the cloud in the direction of the satellite. This neglects a small term due to downwelling thermal radiation reflected off the cloud in the direction of the satellite.

If there is only one cloud type in the scene, $R_{i,CLD,1}$ is expressed as

$$R_{i,CLD,1} = \tau_{ic_1} R_{i,CLR} + \varepsilon_{ic_1} B_i(T_{c_1}) \tau_i(p_{c_1}) + (1-\tau_{ic_1}) \int_{p_{c_1}}^{o} B_i[T(p)] \left(\frac{d\tau_i}{d\ell np} \right) d\ell np + \rho'_{ic_1} H_i \tau_i'(p_{c_1}) \cos\theta_o \quad . \tag{5.4.32}$$

When retrieving cloud properties, the channels used are limited to those at frequencies less than 1250 cm^{-1}, for which the last term in equation (5.4.32) is not significant. Making the approximation that $\tau_{ic_1} = (1-\varepsilon_{ic_1})$, then equations (5.4.30 and 5.4.32) combine to give

$$\overline{R}_i = \left(1-\alpha_1 \varepsilon_{ic_1}\right) R_{i,CLR} + \left(\alpha_1 \varepsilon_{ic_1}\right) R^B_{i,CLD}\left(p_{c_1}\right) \tag{5.4.33}$$

where $R^B_{i,CLD}(p_{c_1})$ is the radiance form a black cloud ($\tau_{ic} = 0, \varepsilon_{ic} = 1$) at cloud top pressure p_{c_1}. It is apparent that the term $\alpha_1 \varepsilon_{ic_1}$ appears only as a product in equation (5.4.33). Therefore α and ε_{ic} are not determined independently, but only as a product, which can be thought of as the radiatively effective cloud fraction that may be a function of frequency. To the extent that ε_{ic} is a function of frequency, the frequency dependent term $\alpha_1 \varepsilon_{ic_1}$ is expressed as $\left(\alpha\varepsilon_{c\bar{\nu}}\right)_1 F_1(\nu)$ where $(\alpha\varepsilon_{c\bar{\nu}})_1$ is a representative

value of the effective cloud fraction $\alpha_1 \varepsilon_{ic_1}$ at a given frequency $\bar{\nu}$, and $F_1(\nu)$ expresses the frequency dependence of $\frac{\varepsilon_{c\nu}}{\varepsilon_{c\bar{\nu}}}$.

In the case of two cloud types, assuming $\tau_{ic_2} = (1 - \varepsilon_{ic_2})$, then the radiances are written as

$$R_i = (1 - \overline{\alpha\varepsilon}_{i,1} - \overline{\alpha\varepsilon}_{i,2}) R_{i,CLR} + \overline{\alpha\varepsilon}_{i,1} R_i^B(p_{c_1}) + \overline{\alpha\varepsilon}_{i,2} R_i^B(p_{c_2}) \qquad (5.4.34)$$

where $\overline{\alpha\varepsilon}_{i,1}$ and $\overline{\alpha\varepsilon}_{i,2}$ are the radiatively effective cloud fractions for the clouds at p_{c_1} and p_{c_2}. For the higher cloud at p_{c_1}, $\overline{\alpha\varepsilon}_{i,1} = \alpha_1 \varepsilon_{ic_1}$ as before. On the other hand, for the lower cloud

$$\overline{\alpha\varepsilon}_{i,2} = \varepsilon_{ic_2} [\alpha_2 + (1 - \varepsilon_{ic_1}) \alpha_1 \alpha_{12}] \qquad (5.4.35)$$

where α_{12} is the fraction of the area covered by cloud type 1 which is under-covered by cloud type 2. In equation (5.4.35), ε_{ic_2} multiplies the cloud fraction for layer 2 as seen from above, and is comprised of two parts: α_{12} is the fraction of the scene covered only by clouds in layer 2, and $(1 - \varepsilon_{ic_1}) \alpha_1 \alpha_{12}$ is that part of the scene covered by clouds of both type 1 and type 2, which is seen through cloud type 1, with transmissivity $(1 - \varepsilon_{ic_1})$. If either ε_{ic_1} is independent of frequency or α_{12} is the same for all fields of view, this situation corresponds to two cloud formations. In the first case, the radiances are equivalent to a well-defined, frequency independent amount of each type of black cloud. In the second case, cloud type 1 has a constant spectral dependence in each field-of-view which combines properties of cloud types 1 and 2. To the extent that $(1 - \varepsilon_{ic_1})$ is frequency dependent, and α_{12} depends on field-of-view, this situation actually contains three cloud formations, because the spectral dependence of radiances in areas covered by clouds at both levels is different from that of clouds at either of the two levels, in a manner that is field-of-view dependent. The significance of this with regard to determination of cloud-cleared radiances remains to be tested. With regard to

determination of cloud parameters, the spectral dependence of $\overline{\alpha\varepsilon}_{i,2}$ contains the product of two spectrally dependent terms ε_{ic_2} and ε_{ic_1}. To first order, $\overline{\alpha\varepsilon}_{i,2} = \alpha\varepsilon_{c_2} F_2(\nu)$ but care must be taken in interpreting $F_2(\nu)$.

Currently, cloud parameter retrievals have been attempted using the AIRS team simulations, which contain two layers of clouds with constant known spectral emissivity (=0.9) with α_{12} equal to zero for all fields-of-view. Observations in each of the nine fields of view k=1,9 were used to determine cloud parameters. The channel radiances $\overline{R}_{i,k}$ is expressed as

$$\overline{R}_{i,k} = (1-(\overline{\alpha\varepsilon})_{1k}-(\overline{\alpha\varepsilon})_{2k})R_{i,CLR}+(\overline{\alpha\varepsilon})_{1k}R_i^B(p_{c_1})+(\overline{\alpha\varepsilon})_{2k}R_i^B(p_{c_2}) \quad (5.4.36)$$

The cloud parameter retrieval is performed after all other parameters are solved for, in an exactly analogous manner to that of all other retrieval steps. Given a surface skin temperature, surface spectral emissivity, and atmospheric temperature, moisture, and ozone profiles, $R_{i,CLR}$ and $R_i^B(p_{c_j})$ are readily computed. The only unknowns in equation (5.4.36) are $(\overline{\alpha\varepsilon})_{jk}$ $(j=1, 2;\ k=1, 9)$, and p_{c_1} and p_{c_2}. Using $\overline{R}_{i,k}$ in the 9 fields-of-view for the 15 μm and 8-12 μm channels used to determine η and to solve for these 20 variables. The noise covariance matrix **N** used to retrieve cloud parameters, which represents both noise in the observations and uncertainties in the computed values of $R_{i,CLR}$, is taken to be identical to that used to determine η (Eq. 5.2.15).

Given the n^{th} iteration cloud parameters $\overline{\alpha\varepsilon}^n_{1k}$, $\overline{\alpha\varepsilon}^n_{2k}$, p^n_{c1}, p^n_{c2}, define

$$Y^n_{ik} \equiv \overline{R}_{i,k} - R^n_{ik} = \left(\overline{R}_{i,k} - R_{i,CLR}\right) + \sum_{j=1,2} \overline{\alpha\varepsilon}^n_{jk}\left(R_{i,CLR} - R_i(p^n_{c_j})\right) \quad (5.4.37)$$

where $\overline{R}_{i,k}$ is the i^{th} channel radiance in field-of-view k (Eq. 5.4.36) and $\overline{R}^n_{i,k}$ is computed from the n^{th} iteration parameters. This gives rise to the iterative equation

$$Y_{ik}^{n+1} - Y_{ik}^{n} = \sum_{j=1,2}\left[\left(R_{i,CLR} - R_i(p_{c_j}^{n})\right)\right]\Delta\overline{\alpha\varepsilon}_{jk}^{n} + \sum_{j=1,2}\left[\overline{\alpha\varepsilon}_{jk}^{n}\left(\frac{-\partial R_i(\partial p_{c_j})}{\partial p_{c_j}}\right)\right]\Delta p_{c_j}^{m}$$

$$= \sum_{j=1,2}\left[S_{ik,\Delta\alpha\varepsilon_{jk}}^{n}\right]\overline{\alpha\varepsilon}_{jk}^{n} + \sum_{j=1,2}\left[S_{ik,\Delta p_{c_j}}^{n}\right]\Delta p_{c_j}^{n} \qquad (5.4.38)$$

where the terms in brackets are the appropriate Jacobians, computed empirically as are all other Jacobians. Note that if $\overline{\alpha\varepsilon}_{jk}$ (for all k) and/or $\partial R_i/\partial p_{c_j}$ (for all i) are small for a given p_{c_j}, the Jacobian for that cloud top pressure is small and the cloud top pressure is contained primarily in a heavily damped mode and is not changed significantly from the initial guess. In analysis of simulation data thus far, the second cloud formation usually contains small amounts of low clouds, and p_{c_2} is in general not well determined from the data.

For our retrievals, the first guess cloud top pressures are taken as 350 mb and 650 mb, and the first guess effective cloud fractions taken as 0.25 for each cloud type. The solution is constrained such that $p_{c_1} \geq 100$ mb, $p_{c_2} \leq p_s - 50$ mb where p_s is the surface air pressure. In addition $\alpha\varepsilon_{1,k} + \alpha\varepsilon_{2,k}$ are constrained to be ≤ 1.0. If the second cloud fraction is either set very small in the first guess, or becomes very small in the retrieval, no useful information about the second cloud top pressure is determined.

5.4.8.6 Rejection Criteria

A number of tests are made to test whether the retrieval is rejected. The major cause of rejection is difficulty in dealing with the effects of clouds on the AIRS radiances.

5.4.8.6.1 Assessment of the Cloud-Clearing Fit.

Equations (5.2.30), (5.2.29), and (5.2.25) give the solution for the vectors $\vec{\eta}$ and η and the resultant clear column radiances $\hat{R}_i$. If a successful solution is produced, the

ensemble $\hat{R}_i$ for the cloud-clearing channels should match the incoming estimates of cloud-cleared radiances $R_{i,CLR}$ to a reasonable degree. A poor match is indicative of either a particularly poor first guess or problems in handling the effects of clouds on the radiances. The weighted residuals of the clear-column radiances are computed, as used in the computation of η in brightness temperature units

$$\Delta F = \left(\frac{\sum_i (\hat{R}_i - R_{i,CLR})^2 N_{ii}^{-1}}{\sum_i N_{ii}^{-1} \left(\frac{\partial B_i}{\partial T} \right)^2_{\Theta_i}} \right)^{1/2} \tag{5.4.39}$$

and reject the solution if ΔF computed when generating $\bar{\eta}^1$ is greater than 1.75K.

5.4.8.6.2 Difficult Cloud Cases.

Cases with extensive cloud cover and low contrast are particularly difficult to analyze. The solution is rejected if the sum of the final retrieved cloud fractions for all cloud layers is greater than 80% or the total cloud fraction is greater than 65% and the noise amplification factor (see Equation 5.2.31) is greater than 2.5.

5.4.8.6.3 Large Residuals in Second Pass Retrievals.

The general iterative solution is terminated when either the residual R^n (Equation 5.4.23) is less than 10% of the RSS of the predicted noise for each mode $\delta\tilde{B}_\ell$, (Equation 5.4.17) or R^n is more than 75% of R^{n-1}. Slow convergence indicates a poor solution. The solution is rejected if the converged value of R is greater than 1.75 times the root-sum-square of $\delta\tilde{B}_\ell$ in either the surface parameter retrieval or the temperature profile retrieval in the second pass. Poor convergence generally indicates problems with the clear column radiances $\hat{R}_i^3$.

5.4.8.6.4 Inconsistency of Test "Microwave-Only" and Combined Infrared/Microwave Retrievals.

Under some conditions, the cloud-cleared radiances $\hat{R}_i^3$ is poor but all convergence tests are passed. Nevertheless, the test microwave-only retrieval produces low level temperatures which differ significantly from those of the second pass retrieval. This generally indicates poor cloud-cleared radiances. The solution is rejected if the root-mean-square differences between the temperature in the lowest 3 km of the test microwave-only retrieval differs from that of the second pass retrieval by more than 2K.

5.5 Tuning

To be useful for numerical forecasts, AIRS data must be consistent with data from other sources such as radiosondes. Errors in both the AIRS data and the other data contribute to systematic differences between different data sets. These are removed by a statistical adjustment procedure. There are other errors in the AIRS data that can be recognized in the data and removed before the tuning step. A linear shift in the detector array is one example. For tuning, it is assumed that these corrections have been made. It is also assumed that there exist matched pairs of radiance vectors, one calculated from some measure of truth and one observed by AIRS. The problem is to make an adjustment to remove the systematic differences between the two sets of data.

Before proceeding, it is useful to discuss the procedures used to calculate radiances. Although the calculation of radiances using the procedures of Section 4 is easy once the atmospheric state is completely specified, radiosondes and other sources of information often provide an incomplete description of the atmospheric state. For example, a radiosonde specifies the temperature and water vapor in the lower part of the atmosphere. The radiances depend on these conditions as well as the conditions in upper atmosphere and the surface skin temperature. Estimates of these conditions can be obtained from the satellite retrieval. Values of other gases such as ozone can be obtained from the retrieval as well. When this is done, the adjustment will preserve the original calculated values for the upper atmosphere where little independent knowledge of the atmosphere is available, but it will adjust those variables in the lower atmosphere where an independent measure of truth is available. Further this is done in a way that minimizes the systematic differences between the calculated value and the measure of truth.

5.5.1 Approach

To remove the systematic differences between the calculated and observed radiances, one can be used to predict the other. It is common practice to use the measured radiances to predict adjustments to the calculated values because the data are frequently used in an iterative retrieval procedure in which the radiances are calculated for a series of successive iterations. By using the measured values, the adjustment needs to be done

only once. If the calculated values are used as predictors, a new adjustment would have to be calculated for the new estimate at each iteration. We use a constrained regression for the adjustment. Using standard regression for the adjustment has some potential problems. One is that the regression is probably numerically unstable due to the large number of highly correlated predictors. A second is that unconstrained regression coefficients are often physically unrealistic. For example, channels with weighting functions that peak high in the atmosphere often become major predictors for channels with weighting functions which peak near the surface. It is reasonable to expect that the regression coefficients be slight perturbations to the identity matrix. That is, the calculated radiance for a given channel depends on the measured radiance for that channel, with a coefficient that is nearly unity, while the dependence on other channels is small. This is the form one expects for a slight error in the weighting function peak height. The desired solution is given by the shrinkage operator (Oman *et al.*, 1982). The particular derivation is found in the appendix of Crone *et al.* (1996). The shrinkage estimator, $\mathbf{C}_s$ is obtained by finding the $\mathbf{C}$ that minimizes the trace of $[(\mathbf{C}-\mathbf{C}_0)^T (\mathbf{C}-\mathbf{C}_0)]$ subject to the constraint that the trace of $[(\vec{\mathbf{Y}}-\mathbf{C}\vec{\mathbf{X}})(\vec{\mathbf{Y}}-\mathbf{C}\vec{\mathbf{X}})^T]$ is held constant and where $\mathbf{C}_0$ is an initial estimate for regression coefficients, $\vec{\mathbf{Y}}$ is the value being predicted and $\vec{\mathbf{X}}$ denotes the predictors. In our case, $\vec{\mathbf{Y}}$ is the adjustment, and $\vec{\mathbf{X}}$ is the vector of measured radiances. The shrinkage estimator can be obtained by setting the derivative

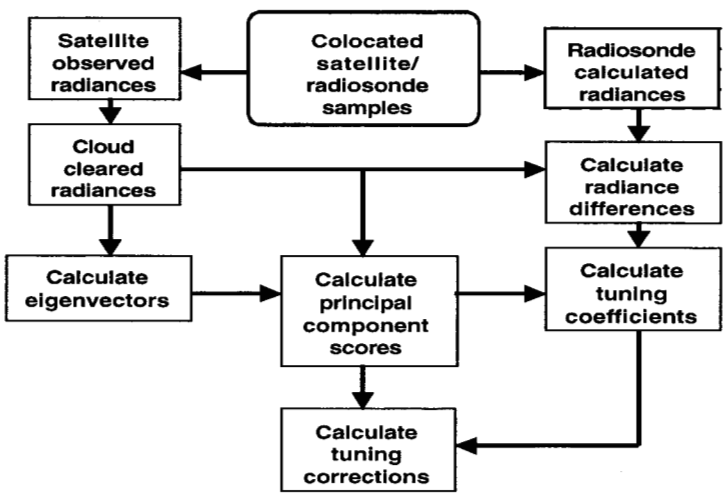

FIGURE 5.5.1 TUNING ALGORITHM FLOW DIAGRAM

$$2(\mathbf{C}-\mathbf{C}_0)+\gamma(-2\vec{\mathbf{Y}}\vec{\mathbf{X}}^{\mathrm{T}}+2\,\mathbf{C}\vec{\mathbf{X}}\vec{\mathbf{X}}^{\mathrm{T}})=0 \tag{5.5.1}$$

which leads to

$$\mathbf{C}_s=(\vec{\mathbf{Y}}\vec{\mathbf{X}}^{\mathrm{T}}+\gamma\mathbf{C}_0)(\vec{\mathbf{X}}\vec{\mathbf{X}}^{\mathrm{T}}+\gamma\mathbf{I})^{-1} \tag{5.5.2}$$

For current instruments with tens of channels, this form of the equation is adequate. For a high spectral resolution instrument like AIRS, the number of channels increases by a factor of about 100. Not only does the large number of channels increase the computations, the larger number, coupled with the fact that more channels are similar, increases the numerical instability. The retrievals are being done with linear transformations such as eigenvectors or "super channels", which are averages of channels that are highly correlated with each other, or with a subset of the channels. Many groups of channels contain no unique information, but can be averaged to reduce the noise. We used eigenvector regression to suppress noise. In this procedure, only the eigenvectors associated with the largest eigenvalues are preserved. We note that, while in general, an equation of the form

$$\mathbf{C}=(\vec{\mathbf{Y}}-\mathbf{C}_0\vec{\mathbf{X}})\vec{\mathbf{X}}^{\mathrm{T}}(\vec{\mathbf{X}}\vec{\mathbf{X}}^{\mathrm{T}})^{-1} \tag{5.5.3}$$

produces regression coefficients that are equal to those given by standard least squares regression, this is not the case if the small eigenvalues of $\vec{\mathbf{X}}\vec{\mathbf{X}}^{\mathrm{T}}$ are suppressed. We use eigenvector regression and use only the eigenvectors associated with the larger eigenvectors. Then, because we expect the calculated value for a channel to be the measured value with a small correction, we set $\mathbf{C}_0$ equal to the identity matrix, $\mathbf{I}$, to give

$$\mathbf{C}=(\vec{\mathbf{Y}}-\vec{\mathbf{X}})\vec{\mathbf{X}}^{\mathrm{T}}(\vec{\mathbf{X}}\vec{\mathbf{X}}^{\mathrm{T}})^{-1} \tag{5.5.4}$$

which leads to the solution

$$\vec{\mathbf{Y}}=(\mathbf{I}+\mathbf{C})\vec{\mathbf{X}} \tag{5.5.5}$$

where the values of $\mathbf{C}$ are small because of the eigenvector constraint. This is the form that we want. It produces a set of regression coefficients that give nearly the same reduction in variance on the dependent set as is given by standard regression, but that

have the desirable physical property that the calculated value for each channel is equal to the measured value plus small corrections. Details of the procedures for doing constrained regressions have been documented in a series of papers (McMillin *et al.* 1989, Crone *et al.* 1996, Uddstrom and McMillin 1994a, Uddstrom and McMillin 1994b). In the equations above, we have been using variables that have the mean subtracted. When the mean is included, equation (5.2.5) becomes

$$\vec{\mathbf{Y}} = [\overline{\mathbf{Y}} - (\mathbf{I} + \mathbf{C})\overline{\mathbf{X}}] + (\mathbf{I} + \mathbf{C})\vec{\mathbf{X}} \tag{5.5.6}$$

We also note that there may be occasions where it is desirable to have a correction that depends on predictors other than radiances such as latitude. This can be done by adding columns to $\vec{\mathbf{X}}$ so that $\vec{\mathbf{X}}'$ has more columns than $\vec{\mathbf{Y}}$ and the identity matrix has corresponding columns of zeroes added. We add this capability because, while one would expect the state of the atmosphere to be defined by the radiances, some current adjustment approaches use other predictors and it is possible that some other predictors that might lead to a more accurate adjustment. This is an aspect that can't be fully determined until launch. The initial system, while it allows for additional predictors to be added, will not use this feature.

6 UNCERTAINTY ESTIMATES

Error estimates of AIRS products, on a retrieval-by-retrieval basis, are an important part of the dataset. In deriving the first thermal and moisture product (section 5.3) an error estimate is derived through the regression and minimum variance physical retrieval using the observational noise covariance matrix (equation 5.3.33) and estimated as thermal and moisture covariance matrix (5.3.35). This chapter deals with the final product (section 5.4) error estimates. This involves estimating likely sources of error and propagating them through the retrieval process. These errors are also important in the construction of the cloud-clearing noise covariance matrix $\tilde{\mathbf{M}}$ (equation 5.2.15) and the retrieval covariance matrix **M** (equations 5.4.23, 5.4.24). In our discussion we distinguish between error estimates of cloud-cleared radiances, discussed in section 5.2 and those of other "geophysical" products discussed here.

Equations (5.2.15) and (5.4.25) contain terms such as $\delta T(P)^n$, indicative of expected errors in retrieved parameters. These errors are case dependent and can be estimated by propagating expected errors through the retrieval system. At any step in the iterative process, the estimate of a parameter, such as $T(P)^n$, is given by

$$T(P)_j^n = T^\circ(P)_j + \sum_{k=1}^{L} F_{jk} A_k^n = T^\circ(P)_j + (\mathbf{FUB}^n)_{j,1}. \qquad (6.1)$$

There are three contributions to the expected error $\delta T(P)_j$. The first contribution comes from the null space error, arising from the error of the first guess in the space outside that of the L eigenfunctions used to expand the solution. The second component arises from errors in the coefficients $\mathbf{B}^n$. The last contribution arises from the damping of the solution in which $(1-\Phi)$ of the first guess (or previous iteration) is believed for each eigenfunction G.

The expected error in parameter X_j^n, δX_j^n, can be expressed in terms of errors in the expansion coefficients A according to

$$\delta X_j^n = \delta X_j^N + \left(\sum_k F_{jk} (\delta A_k)^2 \right)^{1/2} \tag{6.2}$$

where δX_j^N is the null space error and δA^n is the error in the coefficients A^n used to represent X^n. These arise from both errors in the **B** coefficients and errors in the damped portion of the first guess. In every step in the iterative retrieval process, we begin with parameters X^{n-1} having an uncertainty δX_j^{n-1}. The uncertainty of the first guess is specified based on expected errors, as is the null space error. If we knew the signed errors of state X_j^{n-1}, δA^{n-1} could be solved for exactly according to

$$(\delta A_k^{n-1})^2 = (\mathbf{F'F})^{-1}\mathbf{F'}(\delta X^{n-1} - \delta X^N) = (\mathbf{F'F})^{-1}\mathbf{F'}\,(\delta \tilde{X}^{n-1})^2 \tag{6.3}$$

The magnitude of errors in a given state are only estimates. It is preferable to use an analogous form which averages the estimated errors of X over pressure layers in the trapezoid functions **F** to approximate δA_K^{n-1}

$$(\delta A_k^{n-1})^2 = \frac{1}{F_{max,k}} \frac{\sum_j F_{jk} (\delta \tilde{X}_j^{n-1})^2}{\sum_j F_{jk}} \tag{6.4}$$

where $F_{max,k}$ is the largest value of F_{jk} in function k.

In a given iteration, we can now express δA_k^m according to

$$\delta A_k^n = \left[\sum_\ell \left(U_{k\ell} \cdot \frac{\Phi_\ell^n}{\sqrt{\lambda_\ell^n}} \right)^2 + \sum_\ell \left(U_{k\ell} (1 - \Phi_\ell{}^n) \left[U_{j\ell}^2 \sum_j (\delta A_j^{n-1})^2 \right]^{1/2} \right)^2 \right]^{1/2} \tag{6.5}$$

where $\dfrac{\Phi_\ell^n}{\sqrt{\lambda_\ell^n}}$ represents the predicted error in δB_ℓ^n due to propagation of noise and the second term represents the damped error of the previous iteration profile, with δA^{n-1}

coming from Equation (6.4). Given δA_k^n from Equation (6.5), the corresponding profile errors for use in Equations (5.2.15), (5.4.25), and (5.4.26) are computed according to Equation (6.2).

For moisture and ozone profile, the form of the expansion is slightly different (see Equation 5.4.29) and we write

$$\delta q^n(P) = q^{n-1}(P)\left(\delta q^N(P) + \sqrt{\sum_k F_k(P)(\delta A_k)^2} \right) \quad gm/cm^2 \tag{6.6}$$

or

$$\delta q^n(P) = 100\left(\delta q^N(P) + \sqrt{\sum_k F_k(P)(\delta A_k)^2} \right) \quad \% \tag{6.7}$$

Equation (5.4.44) is case dependent through the parameters Φ_ℓ and λ_ℓ which depend on the **S** matrix, and more significantly on the **M** matrix. **M** contains contributions from clouds, $\hat{\mathbf{M}}$, and parameter uncertainty $\tilde{\mathbf{M}}$. The uncertainties determined from Equations (6.3) and (6.7) in turn are used in the computation of $\tilde{\mathbf{M}}$ (Equation 5.4.25) and **N** (Equation 5.2.15). The null space error is taken as 0.5K at all levels and the first guess error is modeled as a function of first guess type. The null space error in percent is taken as 5% for water vapor and ozone respectively.

7 QUALITY ASSESSMENT

Separate plans have been drafted (to be released in early 2000) to describe the AIRS implementation of quality assessment (QA) processing for each data level. This section gives a brief overview of these plans for the level 2 processing. There is often confusion when first encountering the concept of quality assessment and how this is distinguished from quality control, data validation, diagnostics, and retrieved parameter uncertainties. Appropriately enough, each EOS instrument team uses quality assessment processing quite differently. The AIRS implementation emphasizes diagnostics more than the other elements.

AIRS quality assessment processing can be divided into two types. The first type of quality assessment is performed within the product generation software. In the course of data product generation, quality assessment parameters are calculated and quality assessment results are reported. Because this quality assessment information is calculated and collected without user intervention, it is referred to as *automatic quality assessment*. During automatic quality assessment, a variety of summary statistics are calculated which provide insight into product quality. If these summary statistics indicate a probable quality problem, a message is generated in the log, the product is flagged as bad, and quality assessment personnel are notified that *manual quality assessment* is required for that product.

Manual quality assessment is the second type of AIRS quality assessment and is performed by a human operator. If automatic quality assessment indicates that a product is bad, the DAAC first checks to see if there was some type of DAAC operational problem (e.g., input files were not staged and were unavailable during processing). If so, the problem is corrected and the product is re-generated. If no operational problem is found, manual quality assessment is performed at the AIRS Team Leader Science Computing Facility (TLSCF) to determine the problem and whether it can be corrected. During manual quality assessment the archived logs may be used as ancillary information, along with other metadata. Identification and correction activities conducted within investigative quality assessment are also recorded for future reference. Once these

activities have been completed, the data product in question is marked as either good or bad.

There is also a second form of manual quality assessment at the TLSCF, known as *routine quality assessment*. The normal data production stream will be sampled on a daily basis to provide an additional check on data product quality. On average, 10% of the daily granule production will be examined, with sampling criteria supplied by the AIRS Science Team.

The result of Level 2 Quality Assessment is a set of parameters describing retrieval algorithms 'health.' The retrieval algorithm may fail in a number of ways, including complete breakdown of one or several parts of the retrieval process (e. g. the microwave-only retrieval). Alternatively, individual retrieval processes may run to completion but with some unusual computational characteristics (e. g. final retrieval converges only after very many iterations). Additionally, quality assessment information from Level 1A and Level 1B processing may affect retrieval algorithm functioning. This information must be propagated forward to the retrieval. An example of such a situation would be when fewer than nine AIRS spectra (but a sufficient number for cloud-clearing) are available from Level 1B. The most detailed quality assessment information is propagated into the Level 2 Quality Assessment Support Product, produced only when diagnostic options are switched on in the product generation executive. It is intended to be produced at the AIRS TLSCF to aid with problem-solving.

Many small quality assessment fields are included in all AIRS products. For each profile there are flags of processing paths taken and continuous variables reflecting such parameters as speed and quality of algorithm convergence. At a granule level, quality assessment fields include counts of per-profile flags and statistics of per-profile continuous variables. Some of these granule-level quality assessment fields will be used as Product-Specific Attributes so they can be used in ordering interesting data.

8 IMPLEMENTATION OVERVIEW

8.1 AIRS Science Data Processing System

The core of AIRS Science Data Processing System (SDPS) has been designed around several execution units or Product Generation Executables (PGEs); each tailored to process a particular level of data for AIRS, AMSU, HSB and VIS instruments. The Figure 8.1 shows a high level architecture of the AIRS SDPS.

The high level capabilities of these PGEs are:

- L1A PGEs: decommutation, data-number to engineering unit conversion of engineering & geolocation
- L1B PGEs: Radiance conversion with appropriate corrections

- L2 PGE: retrieval of cloud, surface & atmospheric state

Each PGE can be run independently of each other, including the Level 2 PGE where options exist to process through to any desired stage (e.g., microwave, first, or final retrievals). Not shown are additional PGEs. The first group are designed to provide summary or subset of the data products to create Browse images to facilitate data ordering. The second, referred to as the RaObs PGE, is designed to accumulate matchups between coincident radiosonde and AIRS observations for tuning (see Section 5.5).

8.2 Data Storage and Data Processing Requirements

The AIRS SDPS requires approximately 73 GB of archive per day. Table below

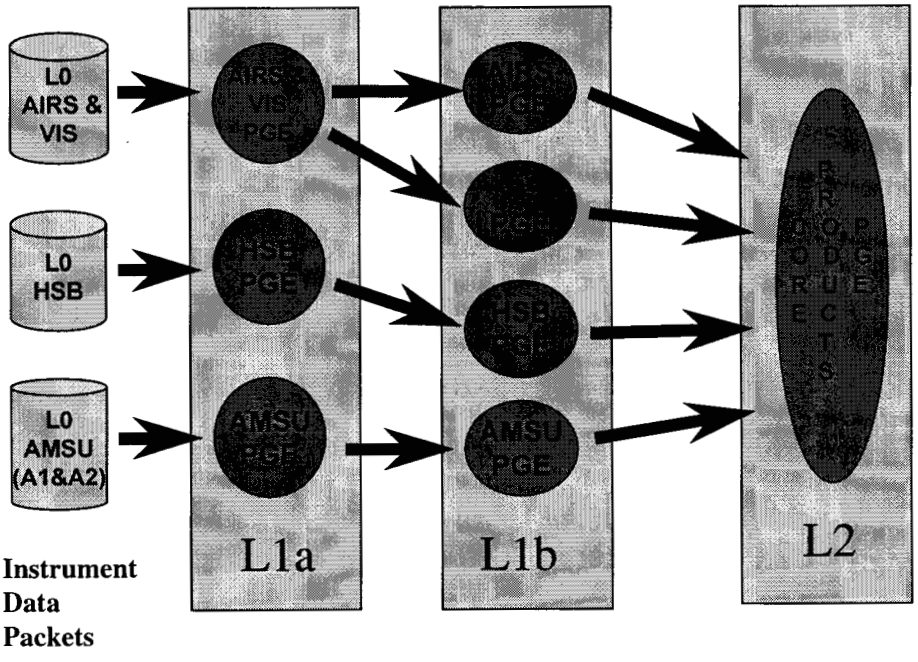

FIGURE 8.1 – HIGH LEVEL REPRESENTATION OF THE AIRS SDPS ARCHITECTURE OF PGES.

summarizes the various categories of data required for processing as well as data produces by the AIRS SDPS.

Data Product Type	Volume
Level 0 data (primary input)	13 GB/day
Aviation forecast	.03 GB/day
Radiosonde data	.08 GB/day
Level 1A products	17 GB/day
Level 1B products	34 GB/day
Level 2 products	8 GB/day
Raobs matchup file	.03 GB/day
Browse files	.4 GB/day
Total	72.54 GB/day

Level 0 data: 54 MB per 6 minutes (granule) of data. Total per day is: 54*240 or 12.96 GB.

L1A data: 70 MB of level 1A for one granule of AIRS, HSB, AMSU, and VIS combined. Total per day is 70*240 or 16.8 GB.

L1B data: 138 MB of level 1B for one granule of AIRS, HSB, AMSU, and VIS combined. Total per day is 138*240 or 33.12 GB.

L2: 32 MB of output per granule. Total per day is 32*240 or 7.68 GB

8.3 Required input data

Geolocated, Calibrated Observed Radiances provided by L1B processing:

- AMSU-A
- HSB
- IRS
- VIS

Static Ancillary Data files provided by TLSCF:

- Decommutation Map
- Constant Sets
- Red and Yellow Limits
- Namelist giving default values for L2 parameters
- AMSU and HSB Sidelobe Correction Matrices
- AMSU and HSB Sunglint Data
- AMSU and HSB Cold Sidelobe Interpolation Arrays
- Lists of Channels to be used at various stages of retrieval
- Calibration Parameters for AMSU, HSB, AIRS and VIS
- AIRS Channels Frequency List
- AIRS Channels Focal Plan Map
- AIRS Correction Parameters and Spectral Features
- Climatology to set initial guess profiles
- Topographic data

- Transmittances for AMSU, HSB and AIRS channels
- Angle Correction Coefficients
- Solar Radiances
- Tuning Coefficients
- Microwave Emissivity Coefficients
- Ancillary Error Estimates
- Covariance Matrices
- Eigenvector Matrices
- Radiance Regeneration Eigenvectors
- Tables of Contribution Weighting Functions
- MW to IR regression coefficients
- Principal Component Mode Regression Coefficients
- Principle Components for Angle Adjustment

Dynamic and Static External Ancillary Data Files provided at the DAAC:

- NCEP 1-Degree Aviation Model (AVN) Product
- Global 1 KM DEM
- Quality Controlled Radiosonde observations, including ship/buoy observations
- Third Generation Vegetation Index

8.4 Simulation System

The architecture of the AIRS SDPS simulation system and its role in validation and verification of AIRS products is shown in the following figure 8.2. The current software has a full level 0 to level 2 data product simulation with three goals in mind: (1) core algorithm performance is based on the simulation, (2) robustness testing of the AIRS data product algorithms is based partly on simulation, (3) data product validation requires an extensive simulation effort. The simulations are to be as realistic and challenging as possible as well as extensive enough to provide a complete set of exception conditions.

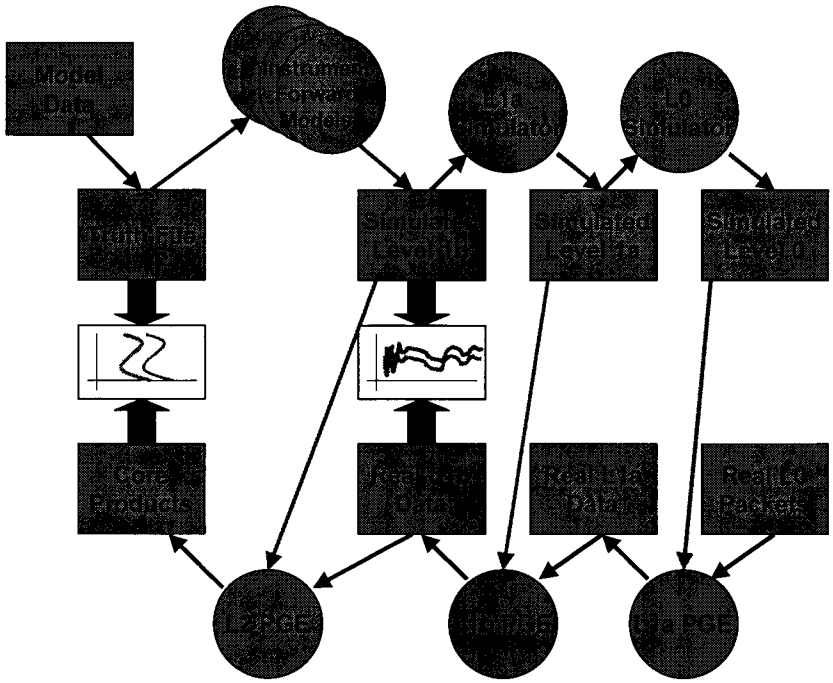

FIGURE 8.2 – THE AIRS SIMULATION SYSTEM INCLUDES SIMULATORS TO GENERATE APPROPRIATE DATA FOR EVERY LEVEL

Early development used simulations based on 4 orbital tracks, each of approximately a quarter orbit in length. Algorithm performance and simple testing has moved to focus on using a number of shorter data granules of pairs of AMSU scanlines or 6 AIRS scanlines (an AIRS data granule is normally 135 AIRS scanlines) with simple changes to represent various geophysical conditions (noise-free, noisy, clear, cloudy, ocean, land, etc.). These simulations of AIRS/AMSU/HSB observations are based on the NCEP eta model forecast for November 5, 1996. Up to two cloud formations were present in each AIRS footprint with cloud amounts and cloud top pressures predicted by the GCM. The cloud top pressures and amounts varied between the nine AIRS footprints encompassed in the single AMSU footprint for which a retrieval was performed. All other geophysical parameters, including surface spectral emissivity and bi-directional reflectance, varied as well. Results are shown for the average of six scan lines with latitudes and longitudes in the vicinity of 11N, 80E; 28N, 110W, and 0N, 116W. Average cloud fractions in a single

AMSU footprint ranged from 1% to 69%. All cases were accepted by the rejection criteria described in section 5.4.8.6

Figure 8.3 shows RMS layer mean temperature errors in roughly 1 km layers between the surface and 200 mb and 3 km layers above. Results are shown for the microwave product, the AIRS regression, the first product retrieval and the final product retrieval. Also indicated on the plot are the errors in surface skin temperature as well as the average RMS error in layers from 100 mb to the surface (called trop) and 700 mb to the surface. The microwave product has large errors beneath 500 mb, where the intrinsic vertical solution is poor. The AIRS regression guess improves over the microwave retrieval in the mid- lower troposphere but still has 2 K errors near the surface, with an average error in the lower troposphere of 1.51 K, compared to 2.67 K for the microwave retrieval. The first product retrieval significantly improves on the regression results, especially beneath 200 mb. While this is the portion of the atmosphere where results are most affected by clouds, both the regression and first product results use the same cloud cleared radiances, based on the first estimate of eta. The first product has an average RMS error of 1.0 K in the lower troposphere, but an error of 1.42 K in the lowest 1 km layer. The final product retrieval, which benefits from the use of improved cloud cleared radiances, further improves on the first product retrieval, with a lower tropospheric temperature error of 0.82 K, and a value in the lowest 1 km of roughly 1 K. Results above 100 mb are also roughly 0.2 K better in the final product retrieval compared to the first product.

Figure 8.4 shows results for the water vapor profile. Values shown are for layer precipitable water in roughly 2 km layers between the surface and 200 mb, plus results for the layer between 200 mb on the top of the atmosphere. Also indicated in the figure is the error in total precipitable water. The microwave product has an error in total precipitable water of 6.8%. 2 km layer errors are typically in the range 10%-25%, with the exception of water vapor between 300 mb and 400 mb, and above 200 mb. The AIRS

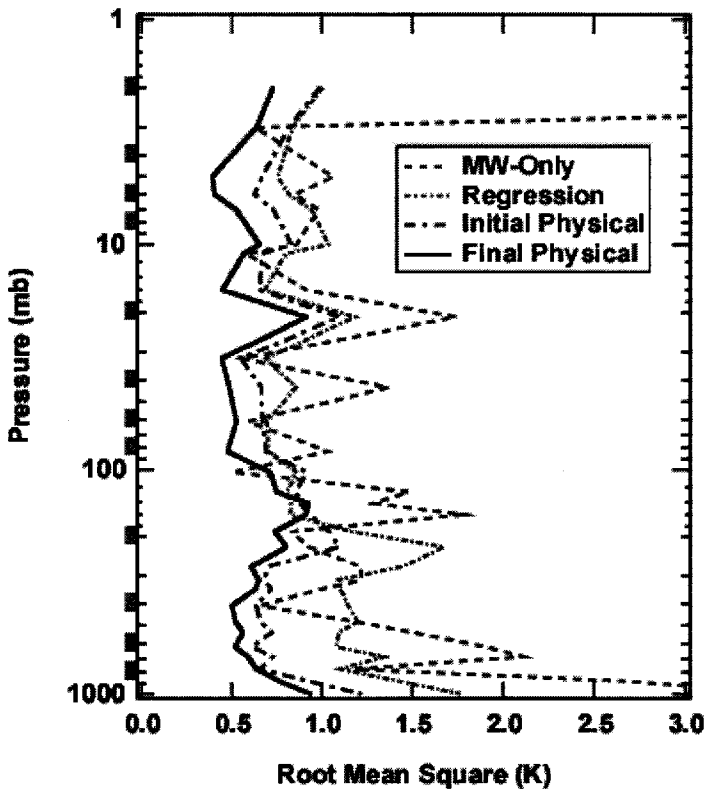

FIGURE 8.3 COMPARISON OF RETRIEVAL PERFORMANCE IN ATMOSPHERIC TEMPERATURE AT EACH STAGE FROM MICROWAVE-ONLY (SECTION 5.1), FIRST PRODUCT REGRESSION AND FIRST PRODUCT PHYSICAL RETRIEAVL (SECTION 5.3), AND THE FINAL PRODUCT PHYSICAL RETRIEVAL (SECTION 5.4)

regression and first product are poorer than the microwave product with regard to total precipitable water and water in the lowest 2 km, but significantly improve on the

microwave result at higher levels of the atmosphere. The first product is also significantly more accurate than the regression guess above 800 mb. The final product has RMS errors better, or slightly poorer, than 15% at all levels in the atmosphere and is comparable to the microwave product with regard to errors in total precipitable water and water vapor in the lowest 2 km.

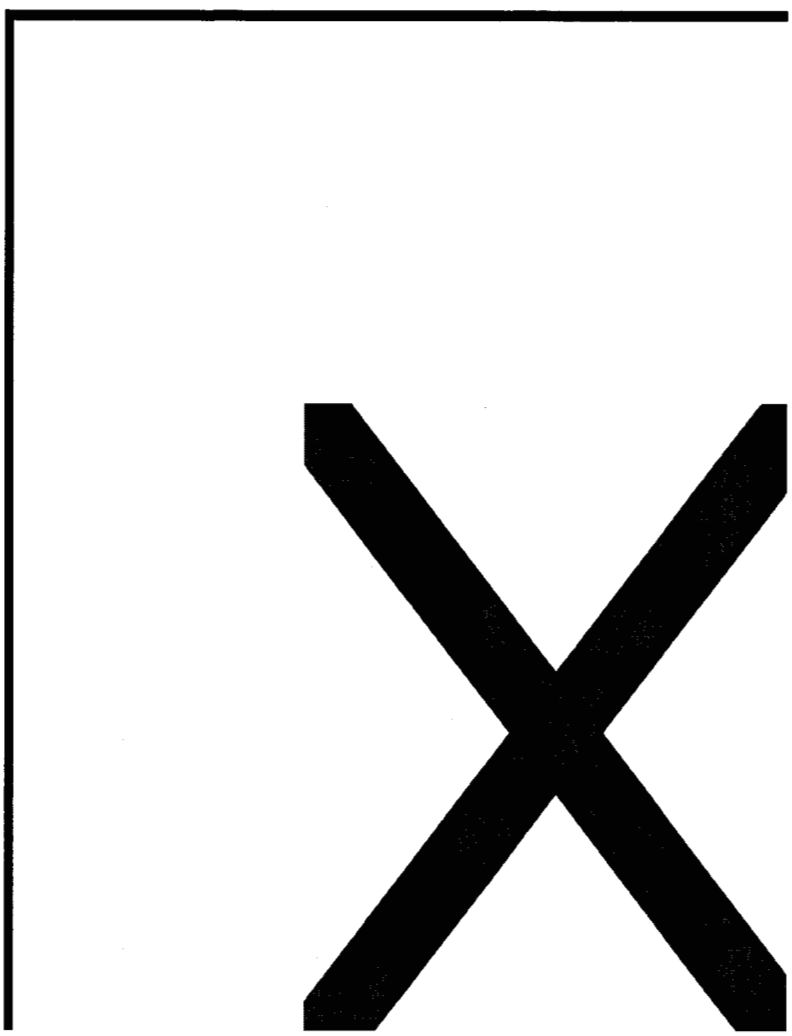

FIGURE 8.4 COMPARISON OF RETRIEVAL PERFORMANCE IN ATMOSPHERIC HUMIDITY AT EACH STAGE FROM MICROWAVE-ONLY (SECTION 5.1), FIRST PRODUCT REGRESSION AND FIRST PRODUCT PHYSICAL RETRIEAVL (SECTION 5.3), AND THE FINAL PRODUCT PHYSICAL RETRIEVAL (SECTION 5.4)

For robustness testing, a whole day of global data is being simulated to provide 240 full-sized AIRS granules. This is intended to help prepare the Science Team for on-orbit

validation activities where similar volumes of data will be needed, and test the quality assessment process and the algorithm robustness.

The full day simulation has been centered on September 13, 1998. This was selected for no other reason than it coincided with a CAMEX-3 aircraft flight under fair weather conditions and there are contemporaneous NOAA-15 AMSU-A and –B measurements available. The simulation activity begins with a generation of level 2 "truth" data, which actually span the time of 03:00 of 13 September 1998 through 03:00 of 14 September 1998. This data is linearly interpolated in time, bilinearly interpolated in the horizontal, and linearly interpolated in log-pressure from the 3-, 6-, and 9-hr forecasts of the Aviation run of the NCEP weather forecasting model. The UARS upper atmosphere climatology was used for the mid-stratosphere through the mesosphere, and hypothetical models were prescribed for the distribution of trace gases carbon dioxide, carbon monoxide, and methane. Since the Aviation run of the NCEP model does not forecast cloud liquid water content (for this epoch), an approximate formula based on cloud-type and cloud height is used to simulate liquid water content. The topography, land fraction, and viewing geometry are all defined using the PGE toolkit. Since the toolkit-generated topography differs from the NCEP surface geopotential height, the surface pressure was adjusted adiabatically based on the forecast surface air temperature. The ground surface temperature remained unchanged. Results from testing the latest version of the Level 2 PGE are expected in early 2000.

8.5 Data Product Validation

A separate AIRS Validation Plan describes the detailed approach for AIRS data product validation. AIRS product validation activities are intertwined with instrument calibration and retrieval algorithm. The former are described in the AIRS Calibration Plan. Calibrated radiances and retrieved quantities from the AIRS system are the result of a complex flow of data from the suite of AIRS/AMSU/HSB instruments and through the data processing software. There are potential sources of uncertainty at many points in this flow, and all can corrupt the quantities ascribed geophysical significance. Additional uncertainties come from incomplete knowledge of the spectral information used in the

infrared and microwave forward radiance models (See Chapter 4.0). The ultimate objective of validation is to establish the validity of the absolute value of the reported geophysical parameters and equally importantly, their associated error bars.

The first stage in validation occurs before launch through instrument calibration and testing, accompanied by algorithm testing with simulated data. To first order these activities establish the baseline from which on-orbit performance of the AIRS suite of instruments can be validated.

In the early period of on-orbit operations for the second stage of validation, the AIRS team will use geophysical observations from many sources to provide a qualitative understanding of the instruments and processing system performance. Although, these vicarious observations are sometimes referred to as 'truth', they in fact have their own uncertainties that must be taken into consideration. The AIRS team has identified vicarious observations presumed to be reasonably well understood. The most important of these include:

- radiosonde observations of atmospheric temperature
- buoy measurements of sea surface temperature
- ARM-CART site observations
- MODIS (EOS-Aqua) observations
- and CERES (EOS-Aqua) measurements

The latter two will be partially validated from their EOS-Terra observations, so that we will have some understanding of their performance on EOS-Aqua. This places bounds on the bias and variance of any residuals found in the comparisons of vicarious and AIRS observations. When conditions of unexpectedly large uncertainty are encountered, they are taken as a probable indicator of problems of one of several types: poor instrument calibration, spectroscopic uncertainty in the forward model, incorrectly parameterized physics in the cloud clearing, and incorrect convergence within the retrieval algorithm. Identifying and correcting these error sources will be the major activity of the AIRS Science Team in the first year or more of AIRS operations.

The simplest AIRS measurements to be examined first are those obtained of cloud-free ocean scenes. This will eliminate dependence on cloud-clearing and minimize

surface inhomogeneity effects on the observed radiance spectrum. From there, the next set of observations to be studied will include cloudy ocean scenes, then cloud-free land scenes, and finally cloudy land scenes.

Only after most of the instrument and software errors have been corrected will the third stage of validation begin. This stage involves validating the reported error bars associated with the AIRS data products. These numbers are essential for AIRS data users in any research or operational sense. These require a sufficiently large ensemble of colocated, coincident measurements to be statistically significant.

ABBREVIATIONS AND ACRONYMS

AERI	Atmospheric Emitted Radiance Interferometer
AIRS	Atmospheric Infrared Sounder
AMSU	Advanced Microwave Sounding Unit
AMSU-A	Advanced Microwave Sounding Unit-A (a 20 channel microwave radiometer)
AMSU-B	Advanced Microwave Sounding Unit-B (a 5 channel microwave radiometer)
AVHRR	
C	degrees Centigrade
COLR	Clear Sky Outgoing Radiation
DAAC	Distributed Active Archive Center
DB, dB	decibel
EOF	Empirical Orthogonal Functions
EOS	Earth Observing System
ER-2	Earth Research-2 (NASA's civilian version of the Lockheed Skunkworks U-2)
ESDIS	Earth Science Distributed Information System
GHz	Gigahertz (10^9 Hertz, or cycles/second)
GSFC	Goddard Space Flight Center
HITRAN	High Resolution Transmission Molecular Absorption Database
HSB	Humidity Sounder of Brazil
IR	InfraRed
JPL	Jet Propulsion Laboratory
K	degrees Kelvin
km	kilometer (10^3 meters)
kPa	kilopascal (10^3 pascal, equivalent to 10 bar)
L0-L4	Level 0 through level 4 (processing)
MHS	Microwave Humidity Sounder
μm	micrometer, micron (10^{-6} meter)
MODIS	Moderate Resolution Imaging Spectroradiometer

MPM87	Millimeter-wave Propagation Model (Liebe and Layton, 1987)
MPM89	Millimeter-wave Propagation Model (Liebe, 1989)
MPM92	Millimeter-wave Propagation Model (Liebe, et al, 1992)
MPM93	Millimeter-wave Propagation Model (Liebe, et al, 1993)
MSU	Microwave Sounder Unit
MW	MicroWave
NASA	National Aeronautics and Space Administration
NCEP	National Center for Environmental Prediction
NEDT	Noise Equivalent Temperature Difference
NEΔT	Noise Equivalent Temperature Difference
NEMS	Nimbus-E Microwave Sounder
NESDIS	National Environmental Satellite Data and Information Service
NEXRAD	Next Generation Radar
NOAA	National Oceanic and Atmospheric Administration
OLR	Outgoing Longwave Radiation
RH	Relative Humidity
SDPS	Science Data Processing System
SIRS	Satellite Infrared Radiation Spectrometer
SSM/T2	Special Sensor Microwave/Water Vapor Profiler
THz	terahertz (10^{12} Hertz)
TIGR	TOVS Initial Guess Retrieval
TIROS	Television Infrared Observation Satellite
TLSCF	Team Leader Science Computing Facility
TOVS	TIROS Operational Vertical Sounder
VTPR	Vertical Temperature Profile Radiometer

REFERENCES

Ackerman, S. A.,1997: Remote sensing aerosols using satellite infrared observations, *J. Geophys. Res.,* **102**, 17069-17079.

Aumann, H. H., and M. T. Chahine, 1976: An infrared multi-detector spectrometer for remote sensing of temperature profiles in the presence of clouds, *Appl. Opt.*, **15**, 2091-2094.

Aumann, H. H., and R. Pagano, 1994: The Atmospheric Infrared Sounder on EOS, *Opt. Eng.*, **32**, 776-784.

Backus, G., and F. Gilbert, 1970: Uniqueness in the inversion of inaccurate gross earth data. *Phil. Trans. Royal Soc. London,* **A266**, 123-192.

Barnett, T. P., R. W. Preisendorfer, L. M. Goldstein, and K. Hasselmann, 1981: Significance tests for regression model hierarchies, *J. Phys. Oceanogr.*, **11**, 1150-54.

Barnett, T.P. and R. Preisendorfer, 1987: Origins and Levels of Monthly and Seasonal Forecast Skill for United States Surface Air Temperatures determined by Canonical Correlation Analysis, *Monthly Weather Review*, **115**, 1825-1850.

Bauer, A., Godon, M., Carlier, J., and Ma, Q., 1995: Water Vapor Absorption in the Atmospheric Window at 239 GHz, *J. Quant. Spectrosc. Radiat. Transfer*, **53**, 411-423.

Bauer, A., Godon, M., Carlier, J., Ma, Q., and R.H. Tipping, 1993: Absorption by H_20 and H_20-N_2 Mixtures at 153 GHz, *J. Quant. Spectrosc. Radiat. Transfer*, **50**, 463-475.

Bauer, A., Godon, M., Kheddar, M., and Hartmann, J.M., 1989: Temperature and Perturber Dependences of Water Vapor Line-Broadening. Experiments at 183 GHz; Calculations Below 1000 GHz, *J. Quant. Spectrosc. Radiat. Transfer*, **41**, 49-54.

Briancon, A. C., 1986: "Estimation and modeling of multidimensional non-stationary stochastic processes: application to the remote sensing of atmospheric temperature fields," Ph.D. thesis, Mass. Inst. of Tech.

Chahine, M. T., 1968: Determination of the temperature profile in an atmosphere from its outgoing radiance. *J. Optic. Soc. Amer.*, **58**, 1634-1637.

Chahine, M. T., 1970: Inverse problems in radiative transfer: determination of atmospheric parameters, *J. Atmos. Sci* , **27**, 960-967.

Chahine, M. T., 1977: Remote sounding cloudy atmospheres. II. Multiple cloud formations. *J. Atmos. Sci.*, **34**, 744-757.

Chahine, M. T., 1982: Remote sounding of cloud parameters, *J. Atmos. Sci.*, **39**, 159-170.

Chahine, M. T., N.L. Evans, V. Gilbert, and R. Haskins, 1984: Requirements for a passive IR advanced moisture and temperature sounder. *Appl. Opts.*, **23**, 979-989.

Chahine, M. T. and J. Susskind, 1989: Fundamentals of the GLA physical retrieval method. *Report on the Joint ECMWF/EUMETSAT Workshop on the Use of Satellite Data in Operational Weather Prediction:* 1989-1993. Vol. 1, 271-300. T. Hollingsworth, Editor.

Chedin, A., N. A. Scott, C. Wahiche, and P. Moulinier, 1985: The improved initialisation inversion method: A high resolution physical method for temperature retrievals from the TIROS-N series. *J. Clim. Appl. Meteor.*, **24**, 128-143.

Chéruy, F., N.A. Scott, R. Armante, B. Tournier, and A. Chedin, 1995: Contribution to the development of radiative transfer models for high spectral resolution observations in the infrared, *J. Quant. Spectrosc. Radiat. Transfer*, **53**, 597-611

Crone, L.J., L.M. McMillin, and D.S. Crosby, 1996: Constrained Regression in Satellite Meteorology. (Accepted for publication in *J. Appl. Meteor.*)

Cuomo, V., R. Rizzi, and C. Serio, 1993: An objective and optimal estimation approach to cloud-clearing for infrared sounder measurements. *Int. J. of Rem. Sensing*, **14**, 729-743.

Derber and Wu, 1996*: Proceedings of the 11th AMS Conference on Numerical Weather prediction*, Norfolk, VA, August 19-23, pp. 236-237.

Druze, J. L., M. Herman, P. Goloub, D. Tanre, A. Marchand, 1999: Characterization of aerosols over ocean from POLDER/ADEOS-1, *Geophys. Res. Letts.*, **26**, 1421-1424.

Edwards, D.P., 1992: Genln2: A general line-by-line atmospheric transmittance and radiance model. NCAR technical note 367+STR, National Center for Atmospheric Research.

Eyre, J.R. and H.M. Woolf. 1988: Transmittance of atmospheric gases in the microwave region: a fast model. *Appl.Opt.*, **27**, 3244--3249.

Eyre, J. R., 1989a: Inversion of cloudy satellite sounding radiances by non linear optimal estimation. I: Theory and simulation for TOVS. *Q. J. R. Meteorol. Soc.* , **115**, 1001-1026.

Eyre, J. R., 1989b: Inversion of cloudy satellite sounding radiances by nonlinear optimal estimation. II: Application to TOVS data. *Q. J. R. Meteorol. Soc.*, **115**, 1027-1037.

Eyre, J. R., 1990: The information content of data from satellite sounding systems: A simulation study. *Q. J. R. Meteorol. Soc.*, **116**, 401-434.

Fleming, H.F. and L.M McMillin, 1977: Atmospheric transmittance of an absorbing gas 2. *Applied Optics*, **16**, 1366

Fleming, H.F. and M.D. Goldberg, and D.S. Crosby, 1986: Minimum variance simultaneous retrieval of temperature and water vapor from radiance measurements, Proc. Second Conference on Satellite Meteorology, Williamsburg, *Amer. Met. Soc.*, 20-23.

Gamache, R.R., J.-M. Hartmann, and L. Rosenmann, 1994: Collisional broadening of water vapor lines- 1. A survey of experimental results. *J. Quant. Spectrosc. Radiat. Transfer*, **52**, 481-499.

Godon, M., Carlier, J. and Bauer, A.,1992: Laboratory Studies of Water Vapor Absorption in the Atmospheric Window at 213 GHz, *J. Quant. Spectrosc. Radiat. Transfer*, **47**, 275-285.

Grody, N. C., and Gruber, A and Shen, W. C., 1980 Atmospheric Water Content over the Tropical Pacific Derived from the Nimbus-6 Scanning Microwave spectrometer. *J. Appl. Meteo.*, **19**, 986-996.

Grody, N. C., 1988: "Surface Identification Using Satellite Microwave Radiometers," *IEEE Trans. Geosci. and Remote Sensing,* vol. 26, 850-859.

Guillou, C., W. Ellison, L. Eymard, K Lamkaouchi, C. Prigent, G. Delbos, G. Balana, and S. A. Boukabara, 1998: Impact of new permittivity measurements on sea surface emissivity modeling in microwaves. *Radio Science*, **33**, 649-667.Halem, M., M. Ghil, R. Atlas, J. Susskind, W. Quirk, 1978: The GISS sounding temperature impact test. *NASA Tech. Memo. 78063*: 2.9-2.82.

Hanel, R. A., B. J. Conrath, D. E. Jennings, and R. E. Samuelson, 1992: Exploration of the solar system by infrared remote sensing. *Cambridge University Press*, Cambridge, Great Britain.

Hannon,S, L.Larrabee Strow, and W.Wallace McMillan, 1996: Atmospheric infrared fast transmittance models: {A} comparison of two approaches. In *Proceedings of SPIE Conference 2830, Optical Spectroscopic Techniques and Instrumentation for Atmospheric and Space Research II.*

Haskins, R.D., R.M. Goody, and L. Chen, 1996: A statistical method for testing a GCM with spectrally-resolved satellite data, Submitted to J. Geophy. Res.

Higurashi, A. and T. Nakajima, 1999: Development of a two channel aerosol retrieval algorithm on a global scale using NOAA AVHRR, *J. Atmos. Sci.*, **56**, 924-941.

Holben, B.N., T.F. Eck, I. Slutsker, D. Tanre, J.P. Buis, A. Setzer, E. Vermote, J.A. Reagan, Y. J. Kaufman, T. Nakajimi, and F. Lavenu, 1996: Multi-band automatic sun and sky scanning radiometer system for measurement of aerosols, accepted for publication *Rem. Sens. Env.*

Husson, N., B. Bonnet, and N. A. Scott, 1992: Management and study of spectroscopic information: The GEISA program, *J. Quant. Spectrosc. Radiat. Transfer*, **48**, 509.

Janssen, M.A. (ed.), 1993: *Atmospheric Remote Sensing by Microwave Radiometry*, Chap. 1, New York: Wiley.

Kaplan, L.D., 1959: Inferences of atmospheric structures from satellite remote radiation measurements, *J. Opt. Soc.Am.*, **49**, 1004

Kaplan, L. D., M. T. Chahine, J. Susskind, and J. E. Searl, 1977: Spectral band passes for a high precision satellite sounder. *Appl. Opt.*, **16**, 322-325.

Kuo, C. C., D. H. Staelin and P. W. Rosenkranz, 1994: "Statistical Iterative Scheme for Estimating Atmospheric Relative Humidity Profiles," *IEEE Trans. Geosci. and Remote Sensing* , **32**, 254-260.

Lamkaouchi, K., G. Balana and W. Ellison, 1997: "New Permittivity Data for Sea Water (30-100 GHz)", ESA report 11197/94/NL/CN.

Liebe, H.J., Gimmestad, G.G., 1978: Calculation of Clear Air EHF Refractivity, *Radio Science,* **13**(2), 245-251.

Liebe, H.J., Gimmestad, G.G., Hopponen, J.D., 1977: Atmospheric Oxygen Microwave Spectrum-Experiment versus Theory, *IEEE Trans. on Ant. and Prop.*, **AP-25**(3), 327-335.

Liebe, H.J., G.A. Hufford, and M.G. Cotton, 1993: Propagation Modeling of Moist Air and Suspended Water/Ice Particles at Frequencies Below 1000 GHz, in *AGARD Conference Proceedings 542, Atmospheric Propagation Effects through Natural and Man-Made Obscurants for Visible to MM-Wave Radiation*, pp.3.1-3.10.

Liebe, H.J., Hufford, G.A., and Manabe, T., A Model for the Complex Permittivity of Water at Frequencies Below 1 THz, *Int. J. of Infrared and Mill. Waves,* **12**(7), pp. 659-675 (1991).

Liebe, H.J., Rosenkranz, P.W., and Hufford, G.A., 1992: Atmospheric 60-GHz Oxygen Spectrum: New Laboratory Measurement and Line Parameters, *J. Quant. Spectrosc. Radiat. Transfer*, **48**(5/6), 629-643.

Liebe, H.J., 1989: MPM-An Atmospheric Millimeter-Wave Propagation Model, *Int. J. of Infr. and Milli. Waves*, **10**(6).

Liebe, H.J., and Layton, D.H., Millimeter-Wave Properties of the Atmosphere: Laboratory Studies and Propagation Modeling, NTIA Report 87-224, October 1987.

Liebe, H.J., Thompson, M.C. Jr., and Dillon, T.A., 1969: Dispersion Studies of the 22 GHz Water Vapor Line Shape, *J. Quant. Spectrosc. Radiat. Transfer*, **9**, 31-47.

Liebe, H.J. and Dillon, T.A., 1969: Accurate Foreign-Gas-Broadening Parameters of the 22-GHz H20 Line from Refraction Spectroscopy, *J. Chem. Phys.*, **50**(2), 727-732 (1969).

Llewellyn-Jones, D.T., P.J. Minnett, R.W. Sanders, and A.M. Zavody, 1984: Satellite multi-channel infrared measurements of sea-surface temperature of the N.E. Atlantic Ocean using AVHRR/2. *Quart. J. Roy. Meteor. Soc.*, **100**, 613-631.

McMillin, L. M., 1971: A Method of determining surface temperatures from measurements of spectral radiances at two wavelengths. Ph. D. dissertation, Iowa State Univ. Ames, IA, 1971.

McMillin, L.M., and H.E. Fleming, 1976: Atmospheric transmittance of an absorbing gas: a computationally fast and accurate transmittance model for absorbing gases with constant mixing ratios in inhomogeneous atmospheres. *Appl.Opt.*, **15**, 358-363.

McMillin, L.M., and H.E. Fleming, 1977: Atmospheric transmittance of an absorbing gas. 2: A computationally fast and accurate transmittance model for slant paths at different zenith angles. *Appl. Opt.*, **16**, 1366-1370.

McMillin, L.M., H.E. Fleming, and M.L. Hill, 1979: Atmospheric transmittance of an absorbing gas. 3: A computationally fast and accurate transmittance model for absorbing gases with variable mixing ratios. *Appl.Opt.*, **18**, 1600-1606.

McMillin, L.M. , L.J. Crone, M.D. Goldberg, and T.J. Kleespies, 1995: Atmospheric transmittance of an absorbing gas 4. *Appl.Opt.*, 34:6274.

McMillin, L.M., L.J. Crone, and T.J. Kleespies, 1995: Atmospheric transmittance of an absorbing gas 5. *Appl.Opt.*, 34:8396.

McMillin, L. M. and Dean, C. A., 1982: Evaluation of a New Operational Technique for producing clear radiances. *J. Appl. Meteo.*, **21**, 1005-1014.

McMillin, L.M., L.J. Crone, and D.S. Crosby, 1989: Adjusting Satellite Radiances by Regression with an Orthogonal Transformation to a Prior Estimate, *J. Appl. Meteor*, **28**, 969-975.

McMillin, L. M 1991: Evaluationi of a Classification Method for Retrieving Atmospheric Temperatures from Satellite Measurements, *J. Appl. Meteo.*, **30**, 432-446.

Mehta, A. V., and J. Susskind, 1999: Outgoing longwave radiation from the TOVS Pathfinder Path A data set, *J. Geophys. Res.*, **104**, 12193-12212.

Mehta, A. V., and J. Susskind, 1999: Longwave radiation flux calculations in the TOVS Pathfinder Path A data set, *NASA Contrator Report*, CR-1999-208643.

Oman, S.D., 1982: Shrinking Towards Subspaces in Multiple Regression, *Technometrics*, **24**, 307-311.

Phillips, N., J. Susskind, and L. McMillin, 1988: Results of a joint NOAA/NASA sounder simulation study. *J. Atmos. Ocean. Tech.*, **5**, 44-56.

Poynter, R.L. and Pickett, H.M., Submillimeter, Millimeter, and Microwave Spectral Line Catalog, *Applied Optics*, **24**(14), pp. 2235-2240 (1985).

Preisendorfer, R.W., Principal Component Analysis in Meteorology and Oceanography, ed. Curtis D. Mobely, Elsevier, 1988.

Reuter, D., J. Susskind, and A. Pursch, 1988: First guess dependence of a physically based set of temperature-humidity retrievals from HIRS2/MSU data. *J. Atmos. Ocean. Tech.*, **5**, 70-83.

Rodgers, C. D., 1976: Retrieval of atmospheric temperature and composition from remote measurements of thermal radiation. *Rev. Geophys. and Space Phys.*, **14**, 609-624.

Rodgers, C. D., 1990: Characterization and error analysis of profiles retrieved from remote sounding measurements. *J. Geophys. Res.*, **95**, 5582-5595.

Rosenkranz, P.W., 1995: A Rapid Atmospheric Transmittance Algorithm for Microwave Sounding Channels, *IEEE Trans. on Geo. and Remote Sensing*, **33**(5), 1135-1140.

Rosenkranz, P.W., 1993: Absorption of Microwaves by Atmospheric Gases, ch. 2 in *Atmospheric Remote Sensing by Microwave Radiometry*, (M.A. Janssen, ed.) New York: Wiley.

Rosenkranz, P. W., 1998a: Improved rapid transmittance algorithm for microwave sounding channels. *1998 IEEE International Geoscience and Remote Sensing Symposium Proceedings,* 728-30.

Rosenkranz, P. W., 1998b: Water vapor microwave continuum absorption: A comparison of measurements and models. *Radio Science*, **33**, 919-928. (Correction, *Radio Science*, **34**, 1025, 1999).

Rothman, L.S., R.R. Gamache, R.H. Tipping, C.P. Rinsland, M.A.H. Smith, D.C Benner, V.Malathy Devi, J.M. Flaud, C.Camy-Peyret, A.Perrin, A.Goldman, S.T. Massie, L.R. Brown, and R.A. Toth The Hitran Molecular Database: Editions of 1991 and 1992,*J. Quant. Spectrosc. Radiat. Transfer*, **48**(5/6), pp. 469-507 (1992).

Rudman, S.D. R.W. Saunders, C.G. Kilsby, and P.J. Minnett, 1994: Water vapor continuum absorption in mid-latitudes: aircraft measurements and model comparisons. *Quart. J. Roy. Meteor. Soc.*, **120**, 795-807.

Schaerer, G. and T. T. Wilheit, 1979: A passive microwave technique for profiling of atmospheric water vapor. *Radio Science*, **14**, 371-375.

Schluessel, P., H.-Y. Shin, W.J.Emery, and H. Grassl, 1987: Comparison of satellite-derived sea-surface temperature with in-situ measurements. *J. Geophys. Res.*, **92**, 2859-2874.

Scott, N. A., and A. Chedin, 1981: A fast line by line method for atmospheric absorption computations: the Automatized Atmospheric Absorption Atlas, 4A, *J. Appl. Meteor.*, **20**, 801-812.

Smith, W. L., 1968: An improved method for calculating tropospheric temperature and moisture from satellite radiometer measurements. *Mon. Wea. Rev.*, **96**, 387-396.

Smith, W. L., and Woolf, H. M., 1976: The Use of Eigenvectors of Statistical Covariances Matrices for Interpreting Satellite Sounding Radiometer Observations. *J. Atmos. Sci.*, **33** 1127-1140.

Smith, W. L., and Platt, C.R.M., 1978:Comparison of satellite-deduced cloud heights with indications from radiosonde and ground-based laser measurements. *J. Appl. Met.*, **17**, 1796-1802.

Smith, W. L., Woolf, H.M., Hayden, C.M., Wark, D.Q., and McMillin, L.M.,1979: The TIROS-N Operational Vertical Sounder, *Bull. Amer. Meteor.Soc.* **60**, 1177.

Smith, W.L., R. O. Knuteson, H.E. Revercomb, F.A. Best, R. Dedecker, H.B. Howell, M. Woolf, 1995: Cirrus cloud properties derived from high sprectal resolution infrared spectrometry during FIRS II. Part I: The High Resolution Interferometric Sounder (HIS) systems. *J. Atmos. Sci.*, **52**, 4238-4245.

Smith, W. L., H. E. Revercomb, R. O. Knuteson, W. Feltz, H. B. Howell, W. P. Menzel, N. R. Nalli, O. Brown, J. Brown, P. Minnett, W. McKeown,1996: Observations of the infrared radiative properties of the ocean -- implications for the measurement of sea surface temperature via satellite remote sensing. *Bull Amer. Meteor.* Soc, **77**, 41-51.

Staelin, D. H., A. H. Barrett, P. W. Rosenkranz, F. T. Barath, E. J. Johnston, J. W. Waters, A. Wouters, and W. B. Lenior, 1975a: The scanning microwave scpectrometer (SCAMS) experiment, pp. 59-86 in *The Nimnus-6 Users Guide.* Goddard Space Flight Center, Greenbelt.

Staelin, D. H., A. L. Cassel, K. F. Kunzi, R. L. Pettyjohn, R. K. L., Poon, and P. W. Rosenkranz, 1975b: Microwave Atmospheric Temperature Sounding: Effects of Clouds on the Nimbus 5 Satellite Data. *J. Atmos. Sci.*, **32** 1970-1976.

Strong, A. E. and E. P. McLain, 1984: Improved ocean surface temperature from space -- Comparison with drifting buoys. *Bull Amer. Meteor. Soc.*, **85**, 138-142.

Strow, L. L., 1993: The measurement of global carbon monoxide using the Atmospheric InfraRed Sounder (AIRS). In A.Chedin, M.T. Chahine, and N.A. Scott, editors, *High Spectral Resolution Infrared Remote Sensing for Earth's Weather and ClimatE Studies*, pp. 351-362. Berlin: Springer Verlag.

Strow, L. L., D.C. Tobin, and S.E. Hannon, 1994: A compilation of first-order line-mixing coefficients for CO_2 Q-branches. *J. Quant. Spectrosc. Radiat. Transfer*, **52**, 281.

Strow, L. L., D. C. Tobin, W. W. McMillan, S. E. Hannon, W. L. Smith, H. E. Revercomb, and R. Knuteson, 1998: Impact of a New Water Vapor Continuum and Line Shape Model on Observed High Resolution Infrared Radiances, *J. Quant. Spectrosc. Radiat. Transfer*, **59**, 303-317.

Strow, L. L., H. E. Motteler, R. G. Benson, S. E. Hannon, and S. De Souza-Machado, 1998: Fast Computation of Monochromatic Infrared Atmospheric Transmittances using Compressed Look-Up Tables}, *J. Quant. Spectrosc. Radiat. Transfer*, **59**, 481-493.

Sundqvist, H., E. Berge and J.E. Kristjansson, 1989: "Condensation and cloud studies with a mesoscale numerical prediction model," *Mon. Wea. Rev.*, **117**, 1641-1657.

Susskind, J., J. Rosenfield, and D. Reuter, 1983: An accurate radiative transfer model for use in the direct physical inversion of HIRS and MSU temperature sounding data. *J. Geophys. Res.*, **88**, 8550-8568.

Susskind, J., J. Rosenfield, D. Reuter, M. T., Chahine, 1984: Remote sensing of weather and climate parameters from HIRS2/MSU on TIROS-N. *J. Geophys. Res.*, **89**, 4677-4697.

Susskind, J. and D. Reuter, 1985a: Retrieval of sea-surface temperatures from HIRS2/MSU. *J. Geophys. Res.*, **90**, 11602-11608.

Susskind, J., D. Reuter, 1985b: Intercomparison of physical and statistical retrievals from simulated HIRS2 and AMTS data. In: Deepak A., Fleming H. E., Chahine, M. T. (eds) Advances in remote sensing retrieval methods. A Deepak, Hampton VA, 641-661.

Susskind, J., 1993: Water vapor and temperature. *Atlas of Satellite Observations Related to Global Change.* Edited by R. J. Gurney, J. L. Foster, and C. L. Parkinson. Cambridge University Press, Cambridge, England, pp. 89-128.

Susskind, J, J. Joiner and M. T. Chahine, 1993: Determination of temperature and moisture profiles in a cloudy atmosphere using AIRS/AMSU. NATO ASI Series, Vol. 19. High spectral resolution infrared remote sensing for earth's weather and climate studies. Springer Verlag Berlin Heidelberg. pp. 149-161. A. Chedin, M. T. Chahine, and N. A. Scott (Editors).

Susskind, J., J. Joiner, and C. D. Barnet, 1995: Determination of atmospheric and surface parameters from simulated AIRS/AMSU sounding data: Retrieval and Cloud Clearing Methodology. Submitted to *Advances in Space Research.*

Susskind, J., C. D. Barnet, and J. Blaisdell 1996: Determination of atmospheric and surface parameters from simulated AIRS/AMSU sounding data Part II: Cloud Clearing Methodology. Submitted to J. Atmos. Ocean. Tech.

Strong, A.E. and E.P. McClain, 1984: Improved ocean surface temperatures from space -- comparison with drifting buoys, *Bull. Amer. Meteor. Soc.*, **85**, 138-142.

Tobin, D.C., 1996a: *Infrared Spectral Lineshapes of Water Vapor and Carbon Dioxide*, PhD thesis University of Maryland Baltimore County.

Tobin, D. C., L. L. Strow, W. J. Lafferty, and W. B. Olson, 1996b: Experimental investigation of the self- and N_2-broadened continuum within the v_2 band or water vapor, *Applied Optics*, **35**, 4724-4734.

Twomey, S., 1963: On the numerical solution of the Fredholm integral equations of the first kind by inversion of the linear system produced by quadrature. *J. Assoc. Comp. Mach.*, **10**, 79-101.

Uddstrom, M.J. and L.M. McMillin, 1994a: System noise in the NESDIS TOVS forward model. part I: specification. *J. Appl. Meteor.*, **33**, 919-938.

Uddstrom, M.J. and L.M. McMillin, 1994b: System noise in the NESDIS TOVS forward model. part II: consequences. *J. Appl. Meteor.*, **33**, 939-947.

Wan, Zhengming and J. Dozier, 1996: a generalized split-window algorithm for retrieving land surface temperature from space. *IEEE Trans. On Geosci. And Rem. Sens.*, **34**, 892-905.

Wark, D.Q., and H.E. Fleming, 1966: Indirect measurements of atmospheric temperature profiles from satellites: I. Introduction, *Monthly Weather Review*, **94**.

Wark, D.Q., and Hillery, D.T, 1969: Atmospheric temperature: A sucessful test of remote probing, *Science*, **165**, 1256-1258.

Wilheit, T.T., 1990: "An algorithm for retrieving water vapor profiles in clear and cloudy atmospheres from 183 GHz radiometric measurements: Simulation studies," *J. App. Meteor.*, **29**, 508-515.

Wolfe, W. L., 1965: *Handbook of Military Infra-red Technology*, U. S. Goverment Printing Office, Washington, D. C.